Three-dimensional numerical analysis of flow structure and sediment transport process in open channels

Esteban Sánchez Cordero

UNIVERSITAT POLITÈCNICA DE CATALUNYA
BARCELONATECH

THREE-DIMENSIONAL NUMERICAL ANALYSIS OF FLOW STRUCTURE AND SEDIMENT TRANSPORT PROCESS IN OPEN CHANNELS

Esteban Sánchez Cordero

ORCID 0000-0002-8206-386X

A dissertation submitted in partial requirements for the degree of Doctor of Philosophy in Civil Engineering

TECHNICAL UNIVERSITY OF CATALONIA

Supervisors

Manuel Gómez Valentín

Ernest Bladé i Castellet

Barcelona, 2019

SENESCYT

Escola de Camins

flumen

CIMNE
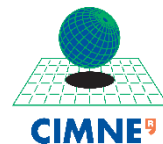
"What we know is a drop, what we don't know is an ocean."

Isaac Newton

To My Family.

Remigio, Teresa, Andrés, and Francisco.

Frida, Tocha and Leia.

Acknowledgments

I would like to thank my advisor Professor Manuel Gómez (Manolo) for his support and motivation throughout these years. I greatly appreciate his valuable suggestions and advice. Also, I would like to thank Professor Ernest Bladé and all FLUMEN´s staff for the good working environment.

My deepest gratitude to Professor Tian-Jian Hsu (Tom) for the possibility of working and learning at the Center for Applied Coastal Research. Similarly my thanks to all my colleagues in this Research Center for their constant support, especially to Yarooh, Yashar, Benjamin, Ali, and Charlie.

Also my sincere appreciation to the Professor Sergei Strijhak from Russian Academy of Sciences, for his advice and help provided in the first part of this research project.

I thank my friends who accompanied the author, offered their help, support and laughter. This author thanks all of them for the unforgettable time shared during these years, especially to Eduardo, Jackson, Alicia, Gonzalo, Marcos, Pablo, Arnau, Andrea, Luis, Susanita, Sasha, Cesca, Cefe, Manuel, Yeudi, Ilias, Abdullah, Noemí, Paúl, Vicente and Chiara.

Last but foremost, I wish to express my wholeheartedly thanks to my family for their invaluable support and love.

CONTENTS

Abstract

This research project focuses on the analysis and prediction of flow structures and sediment transport process in open channels by using three-dimensional numerical models.

The numerical study was performed using the open source computational fluid dynamics (CFD) solver based on the finite volume method (FVM) – OpenFOAM. Turbulence is treated by means of the two main methodologies; i.e. Large Eddy Simulation (LES) and Reynolds-Averaged Navier–Stokes (RANS). The free surface is tracked using the Volume of Fluid method (VOF). In addition, a new multi-dimensional model for sediment transport based on the Eulerian two-phase mathematical formulation is applied.

The results obtained from the different numerical configurations are verified and validated against experimental data sets published in important research journals. The main characteristics of the flow structures are studied by using three set-up cases in steady and unsteady-state (transient) hydraulic flow conditions. On the other hand, the new multi-dimensional model for sediment transport is applied to predict the local scour caused by submerged wall jet test-case.

Non-uniform structured elements are used in the grid configuration of the computational domains. A mesh sensitivity analysis is performed in each test-case study in order to obtain independent grid results. This analysis provides a balance between accuracy and optimal computational time.

The results demonstrate that the three-dimensional numerical configurations satisfactorily reproduce the temporal variation of the different variables under study with correct trends and high correlation with the experimental values.

Regarding the analysis and prediction of the flow structures, the results show the importance of the turbulence approach in the numerical configuration. On the other hand, the results of the new multi-dimensional two-phase model allow to analyze the full dynamics for sediment transport (concentration profile).

Although the numerical results are satisfactory, the application of three-dimensional numerical models in field-scale cases requires a high computational resource.

Resumen

Este trabajo de investigación se enfoca en el análisis y predicción de las estructuras de flujo y el proceso de transporte de sedimentos en canales abiertos mediante el uso de modelos numéricos tridimensionales.

El estudio numérico se realizó utilizando el software de dinámica de fluidos computacional o CFD (por sus siglas en inglés) basado en el método de volúmenes finitos (FVM) - OpenFOAM. La influencia de la turbulencia es analizada con las dos principales metodologías, LES (Large Eddy Simulation) y RANS (Reynolds-Averaged Navier–Stokes); mientras que el método VOF (Volume of Fluid) es usado para la captura de la superficie libre del agua. Además, se aplica un nuevo modelo multidimensional para el transporte de sedimentos basado en la formulación matemática Euleriana de dos fases.

Los resultados obtenidos de las diferentes configuraciones numéricas son verificados y validados con datos experimentales publicados en importantes revistas de investigación. Las características principales de las diferentes estructuras de flujo se estudian en tres casos que incluyen condiciones de flujo estacionario y no estacionario (también conocido como flujo transitorio). Por otro lado, el nuevo modelo multidimensional para el estudio de transporte de sedimentos se aplica para predecir la socavación producida en un caso experimental de chorro de fondo sobre lecho erosionable.

Los dominios computacionales son configurados con elementos estructurados no uniformes. Además, se realiza un análisis de sensibilidad en cada caso de estudio con el objetivo de obtener resultados independientes del tamaño de mallas utilizadas. Este análisis permite encontrar un equilibrio entre la precisión de los resultados y un tiempo de cálculo óptimo.

Los resultados muestran que las configuraciones numéricas son capaces de reproducir satisfactoriamente las diferentes variables en estudio, con tendencias correctas y una alta correlación con los valores experimentales.

Con respecto al análisis y predicción de las estructuras de flujo, los resultados revelan la importancia que tiene el uso del modelo de turbulencia en la configuración numérica. Por otro lado, los resultados obtenidos con el uso de un nuevo modelo multidimensional de dos fases permiten analizar la dinámica completa del transporte de sedimentos (perfil de concentración).

Aunque los resultados numéricos son satisfactorios, la aplicación de modelos tridimensionales en casos a escala de campo exige un considerable recurso computacional en velocidad de cálculo y almacenamiento de datos.

List of Figures

List of Tables

List of symbols

Latin alphabet. Lower case

a_{ij}	deviatoric (anisotropic) part - turbulent kinetic energy
c	sediment mass concentration
c_b	sediment concentration at the nearest cell center above the bed
$c_b{}^*$	equilibrium sediment concentration at a reference level near the bed
d	characteristic grand size of the bed material (i.e. d_{50})
$d_\perp$	normal distance to the wall
e	coefficient of restitution during collision
f_σ	surface tension
g	gravitational acceleration
g_{s0}	radial distribution function
k	turbulent kinetic energy
k_s	effective roughness height
k^{sc}	conductivity of granular temperature
k^f	modified turbulence kinetic energy (Multiphase Eulerian two-phase modeling of sediment transport)
l_o	integral length scale
l^*	turbulent length scale
n	bed porosity
$\mathbf{n}$	normal unit
p	pressure, filtered or Reynolds-averaged
$\bar{p}$	Reynolds-averaged pressure
$\hat{p}$	filtered pressure
p^s	particle pressure
p^{sc}	particle pressure collisional component
p^{sf}	particle pressure frictional component
q	contribution from the source of the quantity ϕ
q_{bi}	bed load transport rates in different directions (fluxes)
q_j	flux of granular temperature
q_o	bed load sediment transport rate per unit width for a flat bed

r_{ij}^{ft}	grain-scale components (Multiphase Eulerian two-phase modeling of sediment transport)
s	specific density of the sediment
t	time
t_l	characteristic timescale of energetic eddies
t_p	particle response time
$u_{i,j}$	fluid velocity components
$\bar{u}_{i,j}$	Reynolds-averaged velocities
$\hat{u}_{i,j}$	filtered velocities
$u_i^{a,w,s}$	velocity for air (a), water (w) and sediment (s)
u^*	turbulent velocity scale
u_*	shear velocity
u^+	dimensionless velocity
u_η	Kolmogorov velocity scales
$\mathbf{u}$	filtered or Reynolds-averaged velocity vector
$\mathbf{u_r}$	compression velocity
w_s	sediment fall velocity
$x_{i,j}$	Cartesian coordinates
y^+	normalized distance to the wall
z_b	reference level near the bed

Latin alphabet. Upper case

B	empirical coefficient (Multiphase Eulerian two-phase modeling of sediment transport)
C	constant that reflects the slope of the sediment flux
C_{max}	maximum Courant number
C_o	courant number
C_s	constant Smagorinsky coefficient
C_α	controls the intensity of the compression
$C_{\varepsilon1}$	constant Standard $k - \varepsilon$ model
$C_{\varepsilon2}$	constant Standard $k - \varepsilon$ model
$C_{\varepsilon13}$	constant Renormalization Group (RNG) k-ε turbulence model
$C_{\varepsilon23}$	constant Renormalization Group (RNG) k-ε turbulence model

$C_{\omega12}$	constant $k - \omega$ model
$C_{\omega22}$	constant $k - \omega$ model
C_μ	constant Standard $k - \varepsilon$ model
$C_{\mu\text{RNG}}$	constant Renormalization Group (RNG) k-ε turbulence model
$C_{1\varepsilon}, C_{2\varepsilon}, C_{3\varepsilon}, C_{4\varepsilon},$ C_μ	constants Multiphase Eulerian two-phase modeling of sediment transport
D	flow field domain (LES model)/ deposition rate (Single-phase sediment transport model)
D_*	dimensionless particle diameter
E	entrainment /erosion rate
G	function filter
H	water depth from bed
J_{int}	energy production / dissipation - interaction with the carrier fluid
L	characteristic length of the involve geometries
$\mathcal{L}_{ij}$	Germano identity
M_i^{fs}, M_i^{sf}	interphase momentum (Multiphase Eulerian two-phase modeling of sediment transport)
N	number of identical experiments at a certain time - Reynolds averaging analysis
P_k	turbulent production
R	relative submerged density
Re	Reynolds number
R^2	Coefficient of determination
R_{ij}^{ft}	Reynolds stress (Multiphase Eulerian two-phase modeling of sediment transport)
R	Reynolds stress (RANS) or subgrid-scale Reynolds stress (LES)
S	surface in a control volume
$\hat{S}_{ij}$	strain rate of the large scale or resolved field strain rate tensor
S_{ij}^f	fluid-phase strain rate tensor (Multiphase Eulerian two-phase modeling of sediment transport)
S_{ij}	strain-rate tensor
S_t	Stokes number
$S_{ij}{}^s$	sediment-phase strain rate tensor

S	strain rate – tensor notation
T	Time interval over which averaging is performed - Reynolds averaging analysis
U	characteristic velocity of the flow
U	magnitude absolute velocity
V	volume in a control volume
V_f	volumes occupied by the interstitial fluid
V_P	volumes occupied by the particles

Greek alphabet. Lower case

α	volume fraction (VOF method)/ Turbulence drag parameter (Multiphase Eulerian two-phase modeling of sediment transport)
β	constant Renormalization Group (RNG) k-ε turbulence model/ bed slope angle (Single-phase sediment transport model)
γ_s	energy dissipation rate
δ_{ij}	Kronecker delta
δ_v	viscous length scale
ε	turbulent kinetic energy dissipation rate
η	Kolmogorov length scales/ bed elevation (Single-phase sediment transport model)
θ	dimensionless bed shear stress (Shield number) / granular temperature (Multiphase Eulerian two-phase modeling of sediment transport)
θ_c	critical Shields number for initiation of motion
θ_{co}	critical Shield number for initiation of motion at the horizontal bed
θ_f	constant friction angle (repose angle)
κ	Von Karman´s constant
κ_α	curvature of the interface
λ	bulk viscosity
μ	viscosity
μ_s	static friction coefficient
μ_{sgs}	subgrid eddy viscosity
μ_t	eddy viscosity
μ^{sc}	particle shear viscosity
μ^{sf}	frictional viscosity

ρ	fluid density
ρ_w	density of water
ρf	volume force term
σ	surface tension coefficient
σ_c	turbulent Schmidt number
σ_k	constant Standard $k - \varepsilon$ model
σ_{k1}	constant $k - \omega$ model
σ_{k2}	constant Renormalization Group (RNG) k-ε turbulence model
σ_ε	constant Standard $k - \varepsilon$ model
$\sigma_{\varepsilon 2}$	constant Renormalization Group (RNG) k-ε turbulence model
$\sigma_{\omega 1}$	constant $k - \omega$ model
ν_t	diffusivity
ϕ	scalar or vector quantity
$\phi^{a,w,s}$	volumetric concentration for air (a), water (w) and sediment (s)
ϕ^f	fluid phase
$\phi(x,t)$	flow variables - Reynolds averaging analysis
$\bar{\phi}(x,t)$	mean value component - Reynolds averaging analysis
$\phi'(x,t)$	fluctuating component - Reynolds averaging analysis
$\overline{\bar{\phi}(x,t)}$	time average over a time-averaged quantity
$\overline{\phi'(x,t)}$	time average over a fluctuating quantity
ϕ_f^s	random-loose-packing concentration for spheres
ϕ_{max}^s	random-close-packing concentration for spheres
φ	angle between the fluid velocity vector at the particle position and the steepest bed slope direction
η_0	constant Renormalization Group (RNG) k-ε turbulence model
τ_b	boundary shear stress/bed shear stress (Single-phase sediment transport model)
τ_{ij}	Reynolds stresses
τ_η	Kolmogorov time scales
$\tau_{ij}{}^{sc}$	particle stress collisional component
$\tau_{ij}{}^{sf}$	particle stress frictional component
$\tau_{ij}{}^{sgs}$	subgrid-scale Reynolds stress

τ_{ij}^{f}	fluid stress (Multiphase Eulerian two-phase modeling of sediment transport)
τ_{ij}^{s}	particle shear stress
υ	dynamic viscosity
υ^{ft}	turbulent eddy viscosity
ψ	dimensionless shear stress parameter

Greek alphabet. Upper case

Γ	diffusion coefficient
Δ	filter cutoff width –LES
Δl	characteristic length of grid size
$\widetilde{\Delta}$	additional test filter
$\mathrm{T}_{ij}{}^{sgs}$	test filtering
Φ	variables- LES model
$\widehat{\Phi}$	filtered (resolved) variable- LES
$\Phi"$	residual (subgrid-scale, SGS) variable-LES

1 INTRODUCTION

1.1 Background and motivation

The prediction of flow and sediment transport in open-channels and rivers presents a significant challenge for river engineering. Flows in natural and artificial channel systems commonly encounter the interaction between a variety of planimetries (i.e. curved and braided channels) and/or structures (i.e. bridge piers, weirs, dams, barrages, intakes, etc.) which usually produce a three-dimensional effect, free-surface variation and bed change that significantly affect the flow structure and the sediment transport process.

Early numerical models based on a set of algebraic and differential equations in one- and two- dimensional approaches have been developed. These numerical models are applied where the vertical velocities and accelerations are negligible, resulting in a hydrostatic pressure distribution.

Recently, the development in computer capabilities has provided the use of three-dimensional numerical models which are based on the application of the Navier-Stokes equations. This numerical approach allows a better representation of the complex process involved, providing a new insight and understanding concerning in river engineering analysis.

Computational Fluid Dynamics (CFD), its fundamental basis being the Navier–Stokes equations, allows the solving of river engineering problems using numerical methods. CFD codes are tools that permit to evaluate different combinations of boundary conditions, geometric changes and also reduce scale-up problems presented in the experimental models.

This implies the analysis of the advantages and disadvantages obtained whenever three-dimensional numerical models are applied in river engineering issues. There is a significant value in identifying the flow structure and sediment transport process in which this numeric approach becomes more important.

1.2 Objectives

1.2.1 Main objective

The main goal of this study is TO USE THREE-DIMENSIONAL NUMERICAL MODELS TO ANALYZE AND PREDICT THE FLOW STRUCTURE AND SEDIMENT

TRANSPORT PROCESS IN OPEN-CHANNELS. Also, it is expected that the conclusions reached would provide an insight into the applications for which the hydrostatic pressure distribution assumption is no longer valid.

1.2.2 Specific Objectives

In order to reach the aforementioned main goals, the following specific targets are pursued:

- Review of the mathematical governing equations that represent the variables involved in both the flow structure and the sediment transport process.
- Understand the importance of the turbulence model and free-surface variation in order to identify the most important flow dynamics processes.
- Select some representative experimental set-up cases for which the three-dimensional effect is important.
- Perform mesh sensitive analysis to obtain results no matter the grid configuration size.
- Verify the accuracy and reliability of the three-dimensional numerical configuration models against experimental results.
- Issue general conclusions regarding the relevance of using a new multi-dimensional numerical approach in the analysis of the sediment transport process.
- Show the key processes and the main results concerning the river channel dynamics.

1.3 Methodology

The three-dimensional study in this research project is developed on the open-source computational fluid dynamics (CFD) code named OpenFOAM. The source code accessibility facilitates the addition/customization of features required in river engineering problems.

The following items describe in detail the steps carried out in this investigation to achieve each of the above specific objectives.

- **Review of governing equations.** The derivation of the governing equations provides the basic knowledge of the fundamentals involved in the three-dimensional numerical simulation. As well, it allows to understand the importance of the use of the turbulence models, the method to track/capture the free surface and the significance of the boundary conditions.
- **Validating the numerical results with experimental data**. Different numerical configurations in steady and unsteady-state (transient) hydraulic flow conditions are analyzed in order to identify the main characteristics of the fluid dynamics processes.
- **Numerical models of sediment transport.** A new multi-dimensional numerical model to analyze the sediment transport process is applied to predict the local scour

caused by a submerged wall jet. To the author's knowledge, this test-case numerical analysis using the kinetic theory has not been reported in the literature.

1.4   Outline of the thesis

Subsequently, the thesis is organized as follows:

The next section, Chapter 2, provides the theoretical background needed for the comprehensive use of a three-dimensional numerical model. The third chapter contains the three-dimensional numerical simulation of three cases in steady and unsteady-state flow conditions to identify the flow dynamics processes involved. Chapter 4 describes the mathematical formulation considered to simulate the sediment transport process. An application to a scouring process is presented. Finally, Chapter 5 presents a summary of the overall conclusions of this research project.

2 GOVERNING EQUATIONS

2.1 Introduction

This chapter provides an overview of the basic mathematical equations required to describe the three-dimensional free-surface flow simulations in river engineering applications. The Navier-Stokes equations for an incompressible viscous flow that represent the physics conservation law properties and the models used to simplify the resolution of turbulent flows based on LES and RANS approaches are described.

The numerical model based on the Finite Volume Method (FVM), the free-surface model founded on the Volume of Fluid method (VOF) and the most common boundary conditions are discussed.

2.2 The Navier-Stokes equations

The governing equations for the fluid flow in hydraulic engineering applications are the incompressible Navier-Stokes equations for Newtonian fluids. These equations consist of the law of conservation of mass (2.1) and the law of conservation of momentum (2.2), which are presented in Eulerian form. The mass conservation equation is also called the continuity equation, which states that since the matter is neither created nor destroyed, it can only be transformed by physical, chemical or biological processes; whereas, the momentum conservation or equation of motion is a vector quantity defined as a product of mass and velocity.

$$\frac{\partial u_i}{\partial x_i} = 0 \tag{2.1}$$

$$\frac{\partial u_i}{\partial t} + u_j \frac{\partial u_i}{\partial x_j} = -\frac{1}{\rho}\frac{\partial p}{\partial x_i} + v\frac{\partial^2 u_i}{\partial x_j \partial x_j} \tag{2.2}$$

where $i, j = 1,2,3$ is the tensor notation (Cartesian coordinates), u_i are the fluid velocity components, p is the pressure, ρ is the fluid density and v is the dynamic viscosity, defined as the viscosity μ divided by ρ. The pressure presents a particular situation, in which it does not appear under a time dependence form, and it is only determined up to a constant. This requires special treatment for numerical schemes in order to solve continuity [1,2].

The transition from laminar to turbulence flow is ruled by Reynolds number defined as,

$$Re = \frac{\rho U L}{\mu} \qquad (2.3)$$

here, U is the characteristic velocity of the flow and L is a characteristic length of the involve geometries.

Laminar flows, at low Reynolds numbers, are stable due to viscous term are dominant and hence the momentum equation becomes more linear. On the other hand, turbulent flows, at high Reynolds numbers, are unsteady, chaotic, random, and involve three-dimensional fluctuations where, inertial term dominates, causing non-linearity in the momentum equation.

2.3 Turbulent scales

The modern theory of turbulence is based on the energy cascade concept first introduced by Richardson [3] and quantified by Kolmogorov [4]. In this theory, turbulence is composed of different scales of flow motion referred as eddies. Through the cascade process, Figure 2.1, the kinetic energy is transferred from largest scales (production mechanism resulting from the flow shear) to smaller and smaller scales by inviscid process (inertia effect) until, at the smallest scales, the friction forces (viscous stresses) become large and the kinetic energy is dissipated as heat. The kinetic energy rate transferred from an eddy to a smaller eddy is the same for each eddy size [5], resulting in equal to the turbulent kinetic energy dissipation rate, ε.

Through dimensional analysis, the smallest scales of turbulent motion, where dissipation occurs, can be defined based on a set of two parameters, ε $[L^2/T^3]$ and υ $[L^2/T]$, i.e. Kolmogorov length (η), time (τ_η) and velocity (u_η) scales.

$$\eta = \left(\frac{\upsilon^3}{\varepsilon}\right)^{1/4} \qquad \tau_\eta = \left(\frac{\upsilon}{\varepsilon}\right)^{1/2} \qquad u_\eta = (\varepsilon\upsilon)^{1/4} \qquad (2.4)$$

The Reynolds number of the Kolmogorov scales is one, i.e. $\eta u_\eta/\upsilon = 1$, which is small enough for the dissipation of the kinetic energy to be effective (see Pope [6]). Additionally, the largest scales of turbulent motion (l_o - integral length scale) are determined by the characteristic size of the flow.
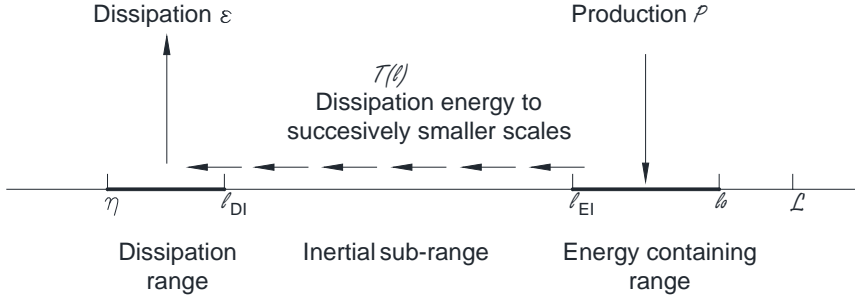
Figure 2.1. Energy cascade at high Reynolds number – schematic diagram
"Adapted from Pope [6]"

Navier Stokes equations describe both laminar and turbulent flow, but the spatial resolution required to solve the whole range of the turbulent scales for practical hydraulic engineering problems makes Direct Numerical Simulation (DNS) approach out of reach based on the current computer capacities (the total computational effort for DNS simulations is proportional to Re^3 for homogeneous turbulence [1]).

In order to reduce computational cost, statistical analysis can be used to avoid the solution of all the scales of flow motion. There are basically two main methodologies. The first one, called Large Eddy Simulation (LES), which directly solves the largest scales of flow motion while modeling only the small scales. On the other hand, the second approach, called the Reynolds-Averaged Navier–Stokes (RANS), parameterizes all turbulent fluctuations presenting the calculation of the turbulent averaged flow.

2.4 Reynolds-Averaged Navier–Stokes (RANS)

2.4.1 Reynolds Averaging

The Reynolds averaging concept introduced by Reynolds [7], is used to derive the equations of motion for time-averaged turbulent quantities. The main idea behind of Reynolds averaging is to decompose any of the flow variables involved, $\phi(x, t)$, which is a function of time and space, into a mean value component, $\bar{\phi}(x, t)$, and a fluctuating component, $\phi'(x, t)$, which is of a stochastic nature.

$$\phi(x, t) = \bar{\phi}(x, t) + \phi'(x, t) \qquad (2.5)$$

The mean value, $\bar{\phi}(x, t)$, can be computed by using any of the following perceptions: time averaging (average of a quantity over a time interval), space averaging (average of a quantity over a space interval) or ensemble averaging (average of numerous identical quantities at a certain time) [8].

The time averaging approach is appropriate when considering a steady turbulent flow (flow does not vary on the average in time)

$$\bar{\phi}(x) = \lim_{T \to \infty} \frac{1}{T} \int_t^{t+T} \phi(x, t) \, dt \qquad (2.6)$$

here, T is the time interval over which averaging is performed and for engineering applications, it is assumed that, it is much greater compared to the time scale of the turbulent fluctuations.

If unsteady flow occurs, with time scales of the same order of the turbulent fluctuations, the ensemble averaging must be used. Ensemble average should be understood as an average of N identical experiments at a certain time, which is both time and space-dependent.

$$\bar{\phi}(x, t) = \lim_{T \to \infty} \frac{1}{N} \sum_{i=1}^{N} \phi(x, t) \qquad (2.7)$$

2.4.2 Averaging Rules

Some of the averaging rules are needed in deriving RANS equations, which include,

- The time average over a time-averaged quantity gives the same time average

$$\overline{\bar{\phi}(x, t)} = \bar{\phi}(x, t) \qquad (2.8)$$

- The time average over a fluctuating quantity is zero.

$$\overline{\phi'(x, t)} = 0 \qquad (2.9)$$

In the ensemble average as the averaging operation, i.e.

$$\overline{\frac{\partial \phi_i}{\partial x_i}} = \frac{\partial \bar{\phi}_i}{\partial x_i} \qquad (2.10) \qquad \qquad \overline{\frac{\partial \phi_i}{\partial t}} = \frac{\partial \bar{\phi}_i}{\partial t} \qquad (2.11)$$

2.4.3 Incompressible RANS equations

The RANS equations are derived from applying the rules (2.8)-(2.11) in the Navier-Stokes equations (2.1) and (2.2)

$$\frac{\partial \bar{u}_i}{\partial x_i} = 0 \qquad (2.12)$$

$$\frac{\partial \rho \bar{u}_i}{\partial t} + \frac{\partial \rho \bar{u}_i \bar{u}_j}{\partial x_j} = -\frac{\partial \bar{p}}{\partial x_i} + \frac{\partial}{\partial x_i}\left[\mu\left(\frac{\partial \bar{u}_i}{\partial x_j} + \frac{\partial \bar{u}_j}{\partial x_i}\right)\right] + \frac{\partial \tau_{ij}}{\partial x_j} \qquad (2.13)$$

where $\bar{u}_i$ and $\bar{u}_j$ are Reynolds-averaged velocities and $\bar{p}$ is the Reynolds-averaged pressure.

The difference between RANS equations and Navier-Stokes equations is that, an additional term, τ_{ij} , called Reynolds stresses, is introduced.

$$\tau_{ij} = -\rho \overline{u'_i u'_j} = -\rho \left(\overline{u_i u_j} - \bar{u}_i \bar{u}_j\right) \qquad (2.14)$$

Reynolds stress is a symmetric second-order tensor, where the diagonal components are the normal stresses and the off-diagonal components are shear stresses.

$$\tau_{ij} = -\rho \begin{bmatrix} \overline{u_\iota'^2} & \overline{u_\iota'u_j'} & \overline{u_\iota'u_k'} \\ \overline{u_j'u_\iota'} & \overline{u_j'^2} & \overline{u_j'u_k'} \\ \overline{u_k'u_\iota'} & \overline{u_k'u_j'} & \overline{u_k'^2} \end{bmatrix}$$

Note that new unknown terms are introduced; consequently, the system is not closed and an additional model denominated turbulence model is required.

The turbulent kinetic energy is the half of the trace of the Reynolds stress

$$k = \frac{1}{2}\rho\overline{u'_\iota u'_j} = \frac{1}{2}\rho\left(\overline{u_\iota'^2} + \overline{u_j'^2} + \overline{u_k'^2}\right) \tag{2.15}$$

Thus, the isotropic stress is defined as $\frac{2}{3}k\delta_{ij}$ and deviatoric (anisotropic) part is

$$a_{ij} = \rho\overline{u'_\iota u'_j} - \frac{2}{3}k\delta_{ij} \tag{2.16}$$

By substituting Equation (2.16) into Equation (2.13), the isotropic term is usually combined with the Reynolds-averaged pressure term, $\bar{p} \leftarrow \bar{p} + \frac{2}{3}k\delta_{ij}$, and a turbulent closure model is necessary specifically for the deviatoric part (with a negative sign), $-a_{ij}$ [‡].

2.4.4   The turbulent-viscosity hypothesis

The turbulent-viscosity hypothesis was introduced by Boussinesq. Reynolds stresses are linked to the velocity gradients via the positive scalar coefficient denominated eddy viscosity, μ_t; following a relation similar to Newtonian fluids.

$$\tau_{ij} = \rho\overline{u'_\iota u'_j} = \mu_t\left(\frac{\partial \bar{u}_i}{\partial x_j} + \frac{\partial \bar{u}_j}{\partial x_i}\right) - \frac{2}{3}k\delta_{ij} \tag{2.17}$$

from where

$$-a_{ij} = -\rho\overline{u'_\iota u'_j} + \frac{2}{3}k\delta_{ij} = \mu_t\left(\frac{\partial \bar{u}_i}{\partial x_j} + \frac{\partial \bar{u}_j}{\partial x_i}\right) \tag{2.18}$$

2.4.5   Turbulence Models

There are numerous turbulence models based on the Boussinesq hypothesis in the literature. In these models, the eddy viscosity, μ_t, can be expressed as a turbulent velocity scale, u^*, multiplied with a turbulent length scale, l^*.

$$\mu_t \propto u^*l^* \tag{2.19}$$

[‡] Lecture notes - Professor Tian-Jian Hsu (University of Delaware - Center for Applied Coastal Research)

The turbulence models range from simple algebraic models to highly sophisticated models and can be grouped into four main categories: Algebraic (Zero-Equations), One-Equations, Two- Equations and Second-Order Closure models [8]. Despite the variety of models developed, none is applicable to all flow conditions.

2.4.6 Two-equation turbulence models

In this study, two-equation turbulence models are used because are the most popular models to simulate a large number of engineering flows [9]. These models require the solution of two transport equation, for both the turbulent kinetic energy and the turbulence length scale. Thus, two-equation models are considered complete because no additional information about turbulence is required. The turbulent kinetic energy is generally chosen as one of the transport equations due to its extensive use and easy interpretation.

The transport equation of turbulent kinetic energy (TKE), k, describes how mean flow feeds kinetic energy into turbulence. k energy is derived analytically from the Navier-Stokes equations using the Reynolds average kinetic energy of a turbulent flow concept. Further, with some mathematical manipulation, the k equation is obtained. The full derivation of the equation is given in Celik [9]. Three different turbulence closures are employed in this study.

Standard $k - \varepsilon$ model

In the $k - \varepsilon$ model of Launder and Spalding [10], the eddy viscosity is modeled as

$$\mu_t = \rho C_\mu \frac{k^2}{\varepsilon} \tag{2.20}$$

The k equation is computed by

$$\frac{\partial(\rho k)}{\partial t} + \frac{\partial(\rho \bar{u}_i k)}{\partial x_j} = \frac{\partial}{\partial x_j}\left[\left(\mu + \frac{\mu_t}{\sigma_k}\right)\frac{\partial k}{\partial x_j}\right] + P_k - \rho\varepsilon \tag{2.21}$$

here P_k is the turbulent production due to the gradient of the mean flow velocity

$$P_k = -\rho\overline{u'_i u'_j}\frac{\partial \bar{u}_i}{\partial x_j} \tag{2.22}$$

σ_k is an empirical coefficient controlling the magnitude of the diffusion of k.

The turbulent dissipation rate, ε , is modeled based on the energy transfer rate in the energy cascade concept and it is determined by the large-scale motion [6]. The ε transport equation is derived in a similar way to k.

$$\frac{\partial(\rho\varepsilon)}{\partial t} + \frac{\partial(\rho \bar{u}_i \varepsilon)}{\partial x_j} = \frac{\partial}{\partial x_j}\left[\left(\mu + \frac{\mu_t}{\sigma_\varepsilon}\right)\frac{\partial \varepsilon}{\partial x_j}\right] + C_{\varepsilon 1}\frac{\varepsilon}{k}P_k - C_{\varepsilon 2}\rho\frac{\varepsilon^2}{k} \tag{2.23}$$

The second and third terms on the right-hand side of Equation (2.23) are referred to the production and the destruction of ε, respectively.

The model constants are obtained from simple flow experiments.

$C_\mu = 0.09$, $\sigma_k = 1$, $\sigma_\varepsilon = 1.3$, $C_{\varepsilon 1} = 1.44$ and $C_{\varepsilon 2} = 1.92$.

$k - \omega$ model

The k-ω model of Wilcox [11] differs from $k - \varepsilon$ model, in the fact that ε is not modeled. A transport equation is implemented for the specific turbulent dissipation rate, ω.

The eddy viscosity is

$$\mu_t = \rho \frac{k}{\omega} \qquad (2.24) \qquad \text{with} \qquad \omega = \frac{\varepsilon}{C_\mu k} \qquad (2.25)$$

The k and ω transport equations are depicted in the Equations (2.26) and (2.27)

$$\frac{\partial(\rho k)}{\partial t} + \frac{\partial(\rho \overline{u}_i k)}{\partial x_j} = \frac{\partial}{\partial x_j}\left[\left(\mu + \frac{\mu_t}{\sigma_{k1}}\right)\frac{\partial k}{\partial x_j}\right] + P_k - C_\mu \rho k \omega \qquad (2.26)$$

$$\frac{\partial(\rho \omega)}{\partial t} + \frac{\partial(\rho \overline{u}_i \omega)}{\partial x_j} = \frac{\partial}{\partial x_j}\left[\left(\mu + \frac{\mu_t}{\sigma_{\omega 1}}\right)\frac{\partial \omega}{\partial x_j}\right] + C_{\omega 12}\frac{\omega}{k}P_k - C_{\omega 22}\rho \omega^2 \qquad (2.27)$$

with the model constants $\sigma_{k1} = 2$, $\sigma_{\omega 1} = 2$ while the coefficients C_μ, $C_{\omega 12}$ and $C_{\omega 22}$ employ standard values 0.09, 0.55 and 0.075, respectively.

Renormalization Group (RNG) k-ε turbulence model

In the $k - \varepsilon$ (RNG) model introduced by Yakhot and Orszag [12], the eddy viscosity is computed as

$$\mu_t = \rho C_{\mu \text{RNG}}\frac{k^2}{\varepsilon} \qquad (2.28)$$

The turbulent kinetic energy and dissipation rate, respectively are

$$\frac{\partial(\rho k)}{\partial t} + \frac{\partial(\rho \overline{u}_i k)}{\partial x_j} = \frac{\partial}{\partial x_j}\left[\left(\mu + \frac{\mu_t}{\sigma_k}\right)\frac{\partial k}{\partial x_j}\right] + P_k - \rho \varepsilon \qquad (2.29)$$

$$\frac{\partial(\rho \varepsilon)}{\partial t} + \frac{\partial(\rho \overline{u}_i \varepsilon)}{\partial x_j} = \frac{\partial}{\partial x_j}\left[\left(\mu + \frac{\mu_t}{\sigma_\varepsilon}\right)\frac{\partial \varepsilon}{\partial x_j}\right] + (C_{\varepsilon 13} - R)\frac{\varepsilon}{k}P_k - C_{\varepsilon 23}\rho \frac{\varepsilon^2}{k} \qquad (2.30)$$

The main difference with the Standard $k - \varepsilon$ model formulation lies in the extra term, R , in the second term, on the right hand side in the Equation (2.30).

$$R = \frac{\eta(1 - \eta/\eta_0)}{1 + \beta\eta^3} \qquad (2.31)$$

with

$$\eta = \frac{Sk}{\varepsilon} \qquad\qquad S = \sqrt{2\bar{S}_{ij}\bar{S}_{ij}} \qquad\qquad \bar{S}_{ij} = \frac{1}{2}\left(\frac{\partial \bar{u}_i}{\partial x_j} + \frac{\partial \bar{u}_j}{\partial x_i}\right) \qquad (2.32)$$

S_{ij} represents the strain-rate tensor. The model constants are derived from RNG analytic theory,

$\sigma_{k2} = 0.7194$, $\sigma_{\varepsilon2} = 0.7194$, $C_{\varepsilon13} = 1.42$, $C_{\varepsilon23} = 1.68$, $C_{\mu RNG} = 0.0845$, $\eta_0 = 4.38$ and $\beta = 0.012$.

2.5   Large Eddy Simulation (LES)

In Large eddy simulation (LES), the large, energy-containing scale structures, anisotropic turbulence, are directly resolved whereas the effects of the small-scale structures, more isotropic, are modeled.

The scale-separation is achieved by applying a filter operation to the Navier-Stokes equations to decompose the variables, Φ, into filtered (resolved) and residual (modeled using a subgrid-scale, SGS) components; denotes as $\hat{}$ and ", respectively.

$$\Phi = \widehat{\Phi} + \Phi" \qquad (2.33)$$

Mathematically, the filter operation is expressed as a convolution of the relevant flow field in the domain, D, with a selected filter kernel.

$$\widehat{\Phi}(x,t) = \iiint\limits_{D} \Phi(x,t)G(x-\lambda,\Delta)d^3\lambda \qquad (2.34)$$

The function filter G retains the Φ values of a size larger than the filter cutoff width, Δ. Filters Kernels include, top-hat or box filter (a simple local average), Gaussian filter and Spectral cut-off filter (both are preferred in the research literature), [13].

The finite volume discretization provides an implicit filtering technique operation, which is usually used together with a top-hat filter.

$$\widehat{\Phi}(x,t) = \frac{1}{\Delta^3} \iiint\limits_{\Delta} \Phi(x,t)d^3\lambda \qquad (2.35)$$

where the box filter G is a Heaviside function expressed as

$$G(x-\lambda,\Delta) = \begin{cases} 1/\Delta^3 & |x-\lambda| \le \Delta/2 \\ 0 & otherwise \end{cases} \qquad (2.36)$$

here, the filtering provides a value which is an average over a rectangular volume Δ^3. The filter width is related to local grid size $\Delta = \left(\Delta_{x_i}\Delta_{x_j}\Delta_{x_k}\right)^{1/3}$, which makes $\hat{\Phi}$ equal to the average value Φ in the computational cell [14].

The mass and momentum filtered equations LES from the incompressible Navier-Stokes equations, i.e.

$$\frac{\partial \hat{u}_i}{\partial x_i} = 0 \tag{2.37}$$

$$\frac{\partial \rho \hat{u}_i}{\partial t} + \frac{\partial \rho \hat{u}_i \hat{u}_j}{\partial x_j} = -\frac{\partial \hat{p}}{\partial x_i} + \frac{\partial}{\partial x_i}\left[\mu\left(\frac{\partial \hat{u}_i}{\partial x_j} + \frac{\partial \hat{u}_j}{\partial x_i}\right)\right] + \frac{\partial \tau_{ij}{}^{sgs}}{\partial x_j} \tag{2.38}$$

where $\hat{u}_i$ and $\hat{u}_j$ are the filtered velocities while $\hat{p}$ is the filtered pressure. $\tau_{ij}{}^{sgs}$ describes the unresolved scales and is called the subgrid-scale Reynolds stress.

$$\tau_{ij}{}^{sgs} = -\rho\left(\widehat{u_i u_j} - \hat{u}_i \hat{u}_j\right) \tag{2.39}$$

The residual stress tensor is presented in Equation (2.40) for the dynamic Smagorinsky model.

$$\tau_{ij}{}^{sgs} = -\rho\left(\widehat{u_i{}^{"} u_j{}^{"}} + \widehat{u_i{}^{"} u_j{}^{"}} + \widehat{u_i{}^{"} u_j{}^{"}} + \widehat{\hat{u}_i \hat{u}_j} - \hat{u}_i \hat{u}_j\right) \tag{2.40}$$

2.5.1   Static Smagorinsky model

The earliest model is the one proposed by Smagorinsky [15]. It is an eddy viscosity model which assumes that the principal effects of the residual stress tensor are increased transport and dissipation [16].

$$\tau_{ij}{}^{sgs} - \frac{1}{3}\tau_{ij}{}^{sgs}\delta_{ij} = \mu_{sgs}\left(\frac{\partial \hat{u}_i}{\partial x_j} + \frac{\partial \hat{u}_j}{\partial x_i}\right) = 2\mu_{sgs}\hat{S}_{ij} \tag{2.41}$$

where, μ_{sgs} is the subgrid eddy viscosity and $\hat{S}_{ij}$ is the strain rate of the large scale or resolved field strain rate tensor, defined by Equation (2.42).

$$\hat{S}_{ij} = \frac{1}{2}\left(\frac{\partial \hat{u}_i}{\partial x_j} + \frac{\partial \hat{u}_j}{\partial x_i}\right) \tag{2.42}$$

The eddy viscosity is obtained through a dimensional analysis – as in RANS.

$$\mu_{sgs} = C_s^2 \rho \Delta^2 |\hat{S}| \tag{2.43}$$

here $|\hat{S}| = \left(\hat{S}_{ij}\hat{S}_{ij}\right)^{1/2}$ and Δ is the filter with. C_s is a constant Smagorinsky coefficient which varies depending on flow characteristics from 0.065 to 0.25, [17].

2.5.2   Dynamic Smagorinsky model

Germano et al. [18] proposed a dynamical model later improved by Lilly [19], in which the parameter C_s is calculated dynamically.

The dynamic Smagorinsky model uses the resolved flow field information and introduces an additional test filter, $\widetilde{\Delta}$, which is typically $\widetilde{\Delta} = 2\Delta$, to obtain subgrid information assuming that the residual stress of these two filtering processes are similar. Hence, the Smagorinsky coefficient is determined to minimize the difference [20].

The residual stress tensor and the test filtering are expressed in Equations (2.44) and (2.45)

$$\tau_{ij}^{\,sgs} = -\rho \left(\widehat{u_i u_j} - \hat{u}_i \hat{u}_j \right) \tag{2.44}$$

$$\mathrm{T}_{ij}^{\,sgs} = -\rho \left(\widehat{\widetilde{u_i u_j}} - \hat{\hat{u}}_i \, \hat{\hat{u}}_j \right) \tag{2.45}$$

The Germano identity is defined as

$$\mathcal{L}_{ij} = \mathrm{T}_{ij}^{\,sgs} - \widehat{\tau_{ij}^{\,sgs}} = -\rho \left(\hat{u}_i \hat{u}_j - \widehat{u_i u_j} \right) \tag{2.46}$$

By applying the Smagorinsky model, the Smagorinsky coefficient is determined as

$$C_s^2 = \frac{\mathcal{L}_{ij} M_{ij}}{M_{ij} M_{ij}} \tag{2.47}$$

where $M_{ij} = 2\widehat{\Delta^2} \left| \hat{S} \right| \hat{S}_{ij} - 2\Delta^2 \widehat{\left| \hat{S} \right| \hat{S}_{ij}}$

Note that RANS and LES equations are similar in their mathematical representation. It is important to mention that, the magnitude of modeled Reynolds stresses are much larger in RANS than in LES [5].

2.6   Flow Near the wall

In viscous flows, the flow velocity at a wall or solid boundary, is zero, no-slip boundary condition, $u_i(x_i, t) = 0$; which implies that all the Reynolds Stresses are zero. Consequently, Pope [6] states that due to the total shear stress is the sum of viscous stress and the Reynolds stress, the wall shear stress is entirely due to viscous contribution, while in the free shear flows the viscous stresses are negligible.

Clearly, in the near wall region, the boundary shear stress, τ_b , and the viscosity are important parameters. The shear velocity, u_*, is define according to Henderson [21].

$$u_* = \sqrt{\tau_b / \rho} \tag{2.48}$$

The shear velocity, provides a direct measure of flow intensity and its ability to entrain and transport sediment particles [22].

The viscous length scale, δ_v, is use to quantify the extent of importance of the viscous effect.

$$\delta_v = \frac{v}{u_*} \qquad (2.49)$$

The normalized distance to the wall, y^+, is measured in viscous length or wall units, where $d_\perp$ is the normal distance to the wall, Equation (2.50). Indeed, y^+ is considered as a local Reynolds number and its magnitude determines the relative importance of viscous and turbulence effect [6].

$$y^+ = \frac{d_\perp}{\delta_v} = \frac{u_* d_\perp}{v} \qquad (2.50)$$

The near-wall region is divided into different regions or sub-layers according to y^+, [23]. In the viscous sub-layer, $y^+ \leq 5$, the turbulence is negligible and it is characterized by a linear correlation. In the buffer sub-layer, $5 < y^+ < 30$, both turbulence and viscous effect are of importance; whilst, in the logarithmic or inertial sub-layer, $y^+ \geq 30$, the viscous effect are small and a complete development of turbulence occurs, Figure 2.2.
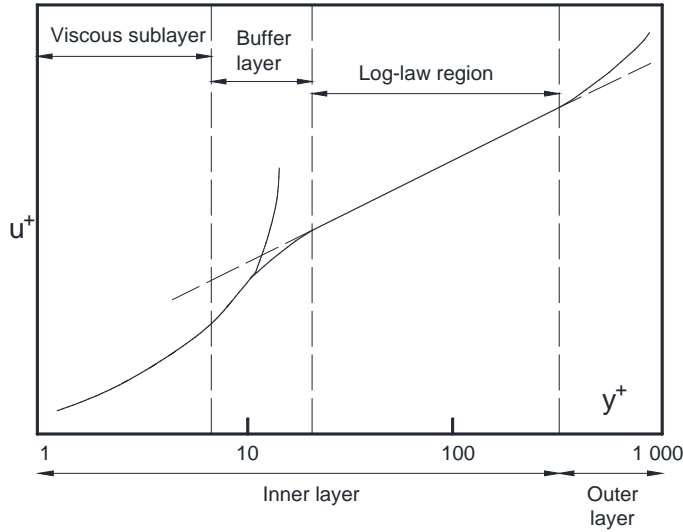
Figure 2.2. Velocity distribution near the wall "Adapted from Davidson [24]"

The near-wall variation of the flow variables is characterized by large gradients. Therefore, in order to resolve the near-wall region, a large number of cells are required. In engineering problems, this becomes almost impossible, due to the computational resource required, and a function is utilized as a bridge between the wall and the mesh point closest to the wall. In practice, the first mesh point is placed in the inertial sub-layer. This latter approach is denoted as a wall-function method.

The standard law of the wall first introduced by von Karman [25], is used to describe the flow velocity profiles for hydraulically smooth solid walls. This is achieved by defining the dimensionless velocity, u^+, as $u^+ = u/u_*$, and y^+.

$$u^+ = y^+ \qquad\qquad\qquad y^+ \leq 5$$

$$u^+ = 5.0 \ln y^+ - 3.05 \qquad\qquad 5 < y^+ < 30 \qquad\qquad (2.51)$$

$$u^+ = \frac{1}{\kappa}\ln y^+ + 5.5 \qquad\qquad y^+ \geq 30$$

The last relationship is known as the log-law, where $\kappa = 0.41$ is Von Karman´s constant.

In the case of hydraulically rough solid walls, most boundaries in river flow, according to García [22], no viscous sub-layer exist, and a modified form of the law of the wall is applied.

$$u^+ = \frac{1}{\kappa}\ln\left(\frac{d_\perp}{k_s}\right) + 8.5 = \frac{1}{\kappa}\ln\left(30\frac{d_\perp}{k_s}\right) \qquad\qquad (2.52)$$

where k_s represents the effective roughness height.

2.7 Numerical Model

In this work, the mathematical formulation is solved numerically using the open-source computational fluid dynamics (CFD) code, OpenFOAM (Open Field Operation and Manipulation). It is based on the finite volume method (FVM) and supports many numerical schemes, both for time and space integration. The code also provides pre- and post-processing utilities, dynamic mesh handling and parallel computation with domain decomposition.

OpenFOAM uses a C++ object-oriented programming language to implement scalar-vector-tensor operations. The accessibility to the source code provides a fundamental platform to customize new solvers and utilities. The former are used to solve the partial differential equation, while the latter are designed to perform tasks that involve data manipulation. In addition, the solvers are written in tensorial partial differential equation form, providing natural language representation in the software. An example for the conservation of momentum equation and its representation provided by Jasak [26] is shown hereafter.

$$\frac{(\partial\rho\mathbf{u})}{\partial t} + \nabla\cdot(\phi\mathbf{u}) = -\nabla p + \nabla\cdot(\mu\nabla\mathbf{u}) \qquad\qquad (2.53)$$

the path to its encoded version in OpenFOAM

```
// Momentum equation
fvVectorMatrix UEqn
    (
        fvm::ddt(rho, U)
      + fvm::div(phi, U)
      - fvm::laplacian (mu, U)
    );
    Solve (UEqn == -fvc::grad (p));
```

where, fvc denotes Explicit discretization, differential operator and fvm denotes Implicit discretization, differential operator.

OpenFOAM does not provide enough details in the Programmer's guide, resulting in a lack of documentation to address the different questions and difficulties presented in the research development. Consequently, the program's learning process demands a considerable amount of time to write new applications and/or add functionality. In addition, the program does not have an integrated graphical user interface, which makes the code uses the Unix command line to execute a specific case.

In the configuration of each case under study, no previous definitions of boundary conditions and/or numerical schemes are provided. This forces the program's user to know the mathematical formulation involved in each of the numerical options that need to be defined in each case study.

Detailed information of the algorithm implementation can be found in Weller et al. [27], Jasak [28] and Rusche [29].

2.7.1   File structure

The file structure for a simulation case in OpenFOAM is composed of three major folders, i.e. 0, constant and system. A scheme of the file structure in OpenFOAM is shown in Figure 2.3
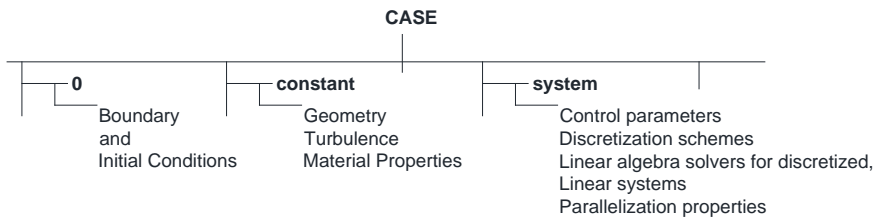
Figure 2.3. General file structure in a simulation case - OpenFOAM

2.7.2 The Finite Volume Method (FVM)

The Finite Volume Method (FVM) first introduced by MacDonald [30] and MacCormack and Paullay [31], is a numerical discretization technique to transform partial differential equations into algebraic equations.

The solution domain is subdivided into a non-overlapping finite set of volumes or elements, also called control volumes, and evaluates the conservation equations in integral form on each element. The integral form of the conservation law for the quantity ϕ, scalar or vector, is expressed in the Equation (2.54).

$$\underbrace{\frac{\partial}{\partial t}\int_V \rho\phi dV}_{\substack{\text{transient term} \\ \text{time}}} + \underbrace{\oint_S \rho\phi\mathbf{u}\cdot\mathbf{n}\,dS}_{\substack{\text{convection term} \\ \text{divergence}}} = \underbrace{\oint_S \Gamma(\nabla\phi)\cdot\mathbf{n}dS}_{\substack{\text{diffusion term} \\ \text{Laplacian}}} + \underbrace{\int_V qdV}_{\text{source term}} \qquad (\ 2.54\ )$$

where V and S are the volume and surface in a control volume, respectively. $\mathbf{n}$ is the normal unit, Γ is the diffusion coefficient and q are the contribution from the source of the quantity ϕ. The transient term is the accumulation of ϕ in the considered control volume, the convection term represents the amount of ϕ that is transported by the flow and the diffusion term is defined as the contribution due to molecular agitation, where the transport of ϕ is as a result of its gradients [1]. Note that the Navier-Stokes equations obey the form of this equation.

In OpenFOAM, the variable values are assigned at the centroid of each control volume, cell-centered variable arrangement method, and the Gauss theorem is applied to transform the volume integrals into the surface integrals. Consequently, the integral conservation law is satisfied for each control volume and for the entire domain (by summing over all control volumes).

In order to obtain an algebraic equation for each control volume, the volume integrals and surface integrals are approximated using quadrature formulae. Therefore, spatial interpolation schemes are used to approximate the variation of the variable values at the control volume surface in terms of the centroid value.

Note that in OpenFOAM the numerical schemes are defined separately. This provides facilities for evaluating different numerical schemes. In this research project, the numerical schemes are applied according to the requirements of each test-case under study (Refer to each case of analysis).

2.7.3   Fluid Flow Model

The filtered or Reynolds-averaged equations for an incompressible flow are presented using a tensor notation. The mass and moment are exposed in the Equations (2.55) and (2.56), respectively.

$$\nabla \cdot \mathbf{u} = 0 \qquad\qquad (2.55)$$

$$\frac{\partial \rho \mathbf{u}}{\partial t} + \nabla \cdot (\rho \mathbf{u}\, \mathbf{u}) = -\nabla p + \nabla \cdot (2\mu \mathbf{S}) + \nabla \cdot (\mathbf{R}) + \rho f \qquad (2.56)$$

where $\mathbf{u}$ and p are filtered or Reynolds-averaged velocity vector and pressure, respectively. ρ is the density and μ is the viscosity in the domain. $\mathbf{S}$ is the strain rate tensor defined by $\mathbf{S} = 1/2\ (\nabla \mathbf{u} + \nabla \mathbf{u}^T)$. The external volume force or body force, ρf, is introduced (gravity and surface tension). $\mathbf{R}$ represents the Reynolds stress (RANS) or subgrid-scale Reynolds stress (LES), which is solve with the different turbulence model or sub-grid approaches.

2.7.4   Free Surface model

The Volume of Fluid (VOF) method proposed by Hirt and Nichols [32], based on a Eulerian approach, is used to capture the water-air interface. An indicator to represent the volume fraction, α , is implemented to determine the water phase contained at each mesh element. To calculate α a new transport equation is introduced.

$$\frac{\partial \alpha}{\partial t} + u_i \frac{\partial \alpha}{\partial x_i} = 0 \qquad \text{in tensor form} \qquad \frac{\partial \alpha}{\partial t} + \nabla \cdot (\mathbf{u}\alpha) = 0 \qquad (2.57)$$

The volume fractions in each mesh element sum up the unity. Therefore, the results of α are between 0 and 1. If $\alpha = 0$ the mesh element is full with air; in contrast, if $\alpha = 1$ the mesh element is full with water. On the other hand, if $0 < \alpha < 1$ the element contains the interface between the two fluids, Figure 2.4. As a result, the two fluids are considered as one effective fluid on the domain and the volume fraction of the each phase is used as the weighting factor to get the mixture properties. The fluid velocity $\mathbf{u}$, density ρ and the viscosity μ of the two phased flow are assumed with a linear variation according to Equations (2.58)-(2.60).

$$\mathbf{u} = \alpha \mathbf{u}_1 + (1 - \alpha)\mathbf{u}_2 \qquad\qquad (2.58)$$

$$\rho = \alpha \rho_1 + (1 - \alpha)\rho_2 \qquad\qquad (2.59)$$

$$\mu = \alpha \mu_1 + (1 - \alpha)\mu_2 \qquad\qquad (2.60)$$

where subscripts 1 and 2 denotes water and air phases, respectively.

In this method, no neat interface between water and air is explicitly defined, due to the numerical diffusion of the volume fraction variable. The numerical solution procedure

developed by Rusche [29] is used to preserve the sharp interface. An additional artificial compression term is introduced in the left-hand side of Equation (2.57).

$$\frac{\partial \alpha}{\partial t} + \nabla \cdot (\mathbf{u}\alpha) + \nabla \cdot (\mathbf{u_r}\alpha(1 - \alpha)) = 0 \tag{2.61}$$

This term works only in the thin interface region and is based on the magnitude of velocity in the transition region. $\mathbf{u_r}$ is the compression velocity which acts perpendicular to the interface and it is calculated according to Weller [33].

$$\mathbf{u_r} = min[C_\alpha |\mathbf{u}|, max|\mathbf{u}|] \frac{\nabla \alpha}{|\nabla \alpha|} \tag{2.62}$$

where C_α controls the intensity of the compression. Thereby, C_α yields no-compression, high compression and conservative compression if C_α is 0, 1, and > 1; respectively. Some numerical studies presented accurate precision in the interface position, on moderate to accurate resolution meshes [34].
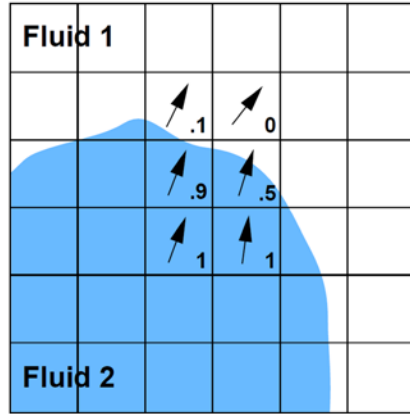
Figure 2.4. Water-air interface with a volume fraction indicator "Adapted from Rusche [29]"

In the VOF method, the volume force term is composed of gravitational and surface tension effects terms.

$$\rho f = \rho g + f_\sigma \tag{2.63}$$

The surface tension is evaluated per unit volume according to

$$f_\sigma = \sigma \kappa_\alpha \nabla \alpha \tag{2.64}$$

where σ is the surface tension coefficient, 0.074 kg $\cdot$ s^{-2} , and κ_α is the curvature of the interface.

$$\kappa_\alpha = -\nabla \cdot \left(\frac{\nabla \alpha}{|\nabla \alpha|} \right) \tag{2.65}$$

2.7.5   Numerical Simulation Procedure for flow field

In the numerical solution of the incompressible Navier-Stokes equations, the non-linearity of the momentum equation and the pressure-velocity coupling require special attention [26]. The convention term in the momentum equation is linearized using a simple strategy in which the fluid velocity in the previous time-step is used. The pressure-velocity coupling procedure is achieved by using the standard PIMPLE approach, which is a merged between PISO (Pressure implicit with split operator) and SIMPLE (semi-implicit method for pressure linked equations) algorithms.

In the PIMPLE algorithm, an equation-corrector and outer-correction loops are allowed for stability. The former parameter, nCorrectors, sets the number of times that in every time step, the algorithm solves the pressure equation and the momentum corrector. The second parameter, nOuterCorrectors, enables the total number of times in which the total system is solved. If no nOuterCorrectors are used, the algorithm is equivalent to the PISO method [35].

The algorithm is described briefly,

- The momentum equation is solved to calculate the velocity field using the initial condition or previous time-step pressure field values, where the solution does not satisfy the continuity condition.

- The velocity field calculated in the previous step is used to solve the pressure equation, which provides a new pressure field. The mass conservation is incorporated into the pressure Poisson equation.

- The new velocity field is calculated using the new pressure field. This interactive algorithm continues until the pressure-velocity system reaches a pre-defined tolerance.

The turbulence closures equations for RANS and sub-grid model for LES are solved by a segregated approach, which means that solves one at a time [36,37]. Regarding the free surface, the modified scheme based on CICSAM is used.

2.7.6   Time Integrator

PIMPLE solver includes an automatic time-step adjustment, Δt, to satisfy the Courant-Fiedrichs-Lewy (CFL) condition.

$$C_o = \frac{\mathbf{U} \Delta t}{\Delta l} \leq C_{max} \qquad\qquad (2.66)$$

where C_o is the Courant number, $\mathbf{U}$ is the magnitude absolute velocity and Δl is the characteristic length of grid size. C_{max} maintains the balance between numerical stability and optimal computational time [38].

2.7.7 Boundary and Initial Conditions

A numerical model is complete when boundary and initial conditions are defined. Boundary Conditions (BC) are specified on all boundary faces of the computational domain. Note that defining BC have a significant impact on the numerical results obtained in a simulation. Mathematically, the BC can be defined using two main approaches.

- Dirichlet condition, where the value of the variable, ϕ, is fixed, $\phi = const$. This condition is implemented by specifying the proper value at the boundary node.

- Neuman condition, where the normal gradient of the variable, ϕ, is prescribed, $\partial_n \phi = const$. This condition specifies the values in which the derivative of a solution is applied at the boundary node.

On the other hand, the initial conditions determine the state of flow variables at time t=0.

The specification of the different boundary conditions in this study are based on engineering interpretation for each test-case study. In OpenFOAM, this is achieved thanks to the use of the swak4FOAM library as well as the customization of some utilities present in the program. Thereby, the author was able to specify the different mathematical expressions required.

2.8   References

[1]   C. Hirsch, Numerical Computation of Internal and External Flows, 2007.

[2]   H.P. Langtangen, K.-A. Mardal, R. Winther, Numerical methods for incompressible viscous flow, Adv. Water Resour. 25 (2002) 1125–1146.

[3]   L.F. Richardson, Weather Prediction by Numerical Process, Cambridge Univ. Press. Repr. by Dover Publ. 1965. (1922) 236.

[4]   A.N. Kolmogorov, Equations of turbulent motion of an incompressible fluid., IZV Akad. Nauk. USSR, Ser. Phys. (Translated into English by D.B. Spalding, as Imp. Coll. Mech. Eng. Dep. Rep. ON/6, 1968, London, U.K.). 6 (1941) 56–58.

[5]   L. Davidson, Fluid mechanics, turbulent flow and turbulence modeling, 2018.

[6]   S.B. Pope, Turbulent Flows, 2000.

[7]   O. Reynolds, On the Dynamical Theory of Incompressible Viscous Fluids and the Determination of the Criterion, Philos. Trans. R. Soc. A Math. Phys. Eng. Sci. 186 (1895) 123.

[8]   F. Moukalled, L. Mangani, M. Darwish, The Finite Volume Method in Computational Fluid Dynamics, 2016.

[9]   I.B. Celik, Introductory Turbulence Modeling, 1999.

[10]   B.E. Launder, D.B. Spalding, The numerical computation of turbulent flows, Comput. Methods Appl. Mech. Eng. 3 (1974) 269–289.

[11]   D.C. Wilcox, Turbulence Modeling for CFD, DCW Industries, La Canada, California (USA), 2006.

[12]   V. Yakhot, S.A. Orszag, Renormalization group analysis of turbulence. I. Basic theory, J. Sci. Comput. 1 (1986) 3–51.

[13]   H.K. Versteeg, W. Malaskekera, An Introduction to Computational Fluid Dynamics, 2nd ed., 2007.

[14]   T. Mukha, M. Liefvendahl, Large-Eddy Simulation of Turbulent Channel Flow, Sweden, 2015.

[15]   J. Smagorinsky, General circulation experiments with the primitive equations. I. The basic experiment, Mon. Weather Rev. 91 (1963) 99–164.

[16]   J.H. Ferziger, M. Peric, Computational Methods for Fluid Dynamics, 3rd ed., 2002.

[17]   M. Saidi, R. Maddahian, B. Farhanieh, H. Afshin, Modeling of flow field and separation efficiency of a deoiling hydrocyclone using large eddy simulation, Int. J. Miner. Process. 112–113 (2012) 84–93.

[18]   M. Germano, U. Piomelli, P. Moin, W.H. Cabot, A dynamic subgrid-scale eddy viscosity model, Phys. Fluids A Fluid Dyn. 3 (1991) 1760–1765.

[19]   D.K. Lilly, A proposed modification of the Germano subgrid-scale closure method, Phys. Fluids A Fluid Dyn. 4 (1992) 633–635.

[20]   Z. Cheng, T.-J. Hsu, J. Chauchat, An Eulerian two-phase model for steady sheet flow using large-eddy simulation methodology, Adv. Water Resour. 111 (2018) 205–223.

[21]   F.M. Henderson, Open Channel Flow, (Macmillan: New York, USA), 1966.

[22]   H.M. García, Sedimentation and erosion hydraulics, in: Hydraul. Des. Handb., McGraw-Hill, New York, 1999.

[23]   H. Tennekes, J.L. Lumley, A first course in turbulence, The MIT Press, Cambridge, Massachusetts, 1972.

[24]   P. Davidson, Turbulence: An Introduction for Scientist and Engineers, 2nd ed., 2015.

[25]   T. von Kármán, Mechanische Ähnlichkeit und Turbulenz, Nachr. Ges. Wiss. Goettingen, Math.-Phys. Kl., 1930.

[26]   H. Jasak, OpenFOAM: Open source CFD in research and industry, Int. J. Nav. Archit. Ocean Eng. 1 (2009) 89–94.

[27]   H.G. Weller, G. Tabor, H. Jasak, C. Fureby, A tensorial approach to computational continuum mechanics using object-oriented techniques, Comput. Phys. 12 (1998) 620.

[28]   H. Jasak, Error analysis and estimation for the finite volume method with applications to fluid flows., PhD thesis, Imperial College London, 1996.

[29]   H. Rusche, Computational Fluid Dynamics of Dispersed Two-Phase Flows at High Phase Fractions, Direct. (2002).

[30]   P.W. MacDonald, The Computation of Transonic Flow Through Two- Dimensional Gas Turbine Cascades, Am. Soc. Mech. Eng. (1971).

[31]   R.W. MacCormack, A.J. Paullay, Computational Efficiency Achieved by Time Splitting of Finite Difference Operators, AIAA Pap. (1972) 72–154.

[32]   C.. W. Hirt, B.. D. Nichols, Volume of Fluid (VOF) Method for the Dynamics of Free Boundaries, J. Comput. Phys. 39(1) (1981) 201–225.

[33]   H.G. Weller, A New Approach to VOF-based Interface Capturing Methods for Incompressible and Compressible Flow, Tech. Rep. (2008).

[34]   E. Roohi, A.P. Zahiri, M. Passandideh-Fard, Numerical simulation of cavitation around a two-dimensional hydrofoil using VOF method and LES turbulence model, Appl. Math. Model. 37 (2013) 6469–6488.

[35]   E. Robertson, V. Choudhury, S. Bhushan, D.K. Walters, Validation of OpenFOAM numerical methods and turbulence models for incompressible bluff body flows, Comput. Fluids. 123 (2015) 122–145.

[36]   X. Liu, M.H. García, Three-Dimensional Numerical Model with Free Water Surface and Mesh Deformation for Local Sediment Scour, J. Waterw. Port, Coastal, Ocean Eng. 134 (2008) 203–217.

[37]   A.M.A. Sattar, H. Jasak, V. Skuric, Three dimensional modeling of free surface flow and sediment transport with bed deformation using automatic mesh motion, Environ. Model. Softw. 97 (2017) 303–317.

[38]   Y. Kim, Z. Cheng, T.-J. Hsu, J. Chauchat, A Numerical Study of Sheet Flow Under Monochromatic Nonbreaking Waves Using a Free Surface Resolving Eulerian Two-Phase Flow Model, J. Geophys. Res. Ocean. 123 (2018) 4693–4719.

3 ANALYSIS OF FREE SURFACE FLOWS IN OPEN CHANNELS

3.1 Introduction

The prediction of free-surface flows is of significant importance in the field of river engineering practice. The free-surface represents the water-air interface, i.e. it is the boundary between the water body and the air, Figure 3.1. Several numerical models have been developed in order to evaluate the hydraulic variables involved in the motion of water in different hydrodynamic configurations in open channels and rivers. Realistically numerical model prediction is not a simple task due to the flow interaction with the geometrical characteristics of the channel and near in-stream structures, which usually can produce secondary currents and vertical accelerations. Therefore, 3D numerical models provide a reliable estimate of flow hydraulic variables.

In this chapter, three-dimensional numerical simulations of free-surface flow based on the solution of the complete set of Large Eddy Simulations (LES) and Reynolds-Averaged Navier-Stokes (RANS) equations are performed. The free water surface is tracked using the Volume of Fluid (VOF) method.

In order to verify and validate comprehensively the 3D numerical configurations, three set-up cases are studied in steady and unsteady-state (transient) hydraulic flow conditions. The results obtained from the different numerical configurations are assessed against published experimental data. In the former two set-up cases, the experimental set-up dimensions, smaller in scale, have hydraulic variables measurements at a finer resolution. On the other hand, the latter set-up case, the experimental set-up dimensions, are on a real scale, since it was built to study the application of the models on field-scale Irrigation Channels.
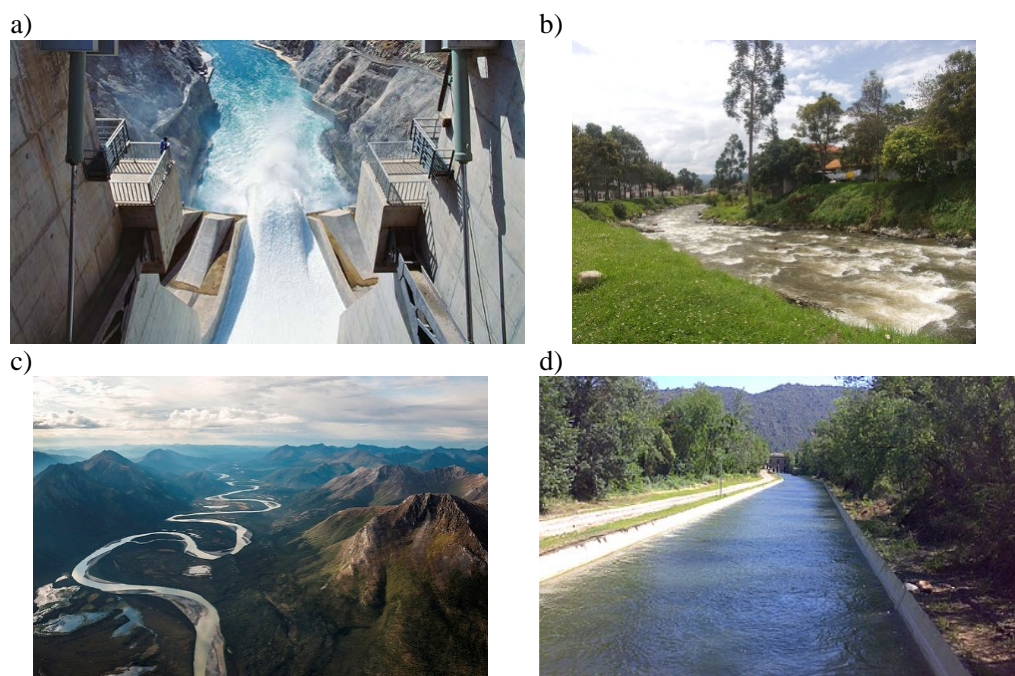
Figure 3.1. Free surface flows, a) Dam water release (www.poyry.at), b) River Bend,
c) Meandering stream (www.nps.gov) and d) Irrigation Channel (www.nivus.com)

3.2 Free surface flow modeling –An overview

In the early development of three-dimensional numerical models, the free-surface simulation in open channel flow ignored the free water surface variations and replaced it with a rigid lid approximation [1,2]. On the rigid lid, the normal velocity is zero, and the pressure is no longer atmospheric [3]. However, this assumption is valid only if the curvature of the interface is smooth, i.e. free-surface presents gentle variations along channel [4].

There are other two main approaches to simulate the free-surface, i.e. surface tracking method and volume tracking method. In the first approach, surface tracking method, the interface is explicitly defined following its movement. The surface is tracked or captured based on; either a Lagrangian approach, where a set of market particles is used [5,6] or a Eulerian approach, where a height function is defined [7,8]. Nevertheless, this approach presents a significant drawback in capturing complex surface topologies (large deformations) as additional operations are required, which adds extra complexity [9,10].

In the second approach, volume tracking method, no net interface is explicitly defined. The fluids are marked either massless particles or by an indicator function [9]. The Volume of Fluid (VOF) method, based on a Eulerian approach, uses a continuous function, the volume of fraction (indicator), to define the localization of the free surface [11,12].

A number of studies based on LES and RANS approaches have demonstrated the applicability of the VOF method within a river engineering context. In river engineering flow

applications, a detailed prediction of the turbulence features in the free-surface boundary is not the main interest and coarse meshes can be applied [13,14].

Most 3D numerical models discretize and solve the LES or RANS equations, using a finite difference, finite element, or finite volume method suitable for structured or unstructured grids.

Ramamurthy et al. [15] and Gholami et al. [16] simulated the flow pattern in an open channel bend flow while a steady hydraulic jump simulation was performed by Bayon et al. [17]; the numerical models used were based on a RANS approach. These authors found an adequate representation of the flow hydraulic characteristics assessed against experimental data.

In recent years, some studies based on LES approach have been reported [18–20]. Kim et al.[18] performed a numerical study of a swash flow driven by a dam-break; the results demonstrate the main characteristics of turbulence in the swash zone. Larocque et al. [14] presented a numerical simulation of dam-break flow using the LES and RANS approaches.

3.3 Three-dimensional numerical analysis of dam-break wave with the presence of an obstacle.[‡]

3.3.1 Introduction

Dam-break waves result from the sudden failure of a dam, river embankments or dikes. Another type of accident is the overtopping of these water control structures. Consequently, a dam-break wave will invade areas that are normally dry, not prepared to support such an event and that faces a series of obstacles (building, bridges, industrial structures, etc.). The presence of obstacles can induce sudden changes in the dam-break wave propagation. Therefore, a reliable simulation is essential for assessing the flood flows pattern and analysis for possible structural failure.

Dam-break is simulated by the sudden removal of a gate in a dry bottom channel. Analytical solutions are available only for idealized situations. Dressler [21] and Whitham [22] presented studies for a horizontal channel, while the researchers [23–25] solved for a sloping channel. More recently, Chanson [26] developed an analytical solution for horizontal and slopping channels using the method of characteristics. However, dam-break waves are commonly computed using 1D and 2D Saint-Venant shallow-water equations (SWE). Mathematically, these equations stating depth-averaged mass and momentum conservation meaning hydrostatic assumption. As a result, several numerical models have been reported by different investigators [27–32]. Quantitative verifications were stated using numerical models against experimental data [33–38]; whilst, diverse authors have investigated the applicability of SWE in the presence of obstacles [39–41].

Despite the usefulness in predicting the main aspects of the dam-break flow pattern by using SWE models, the initial dam-break stages at the immediate vicinity of the dam are mainly influenced by vertical acceleration due to gravity [42]. Likewise, the impact of a flood wave against an obstacle is a local 3D phenomenon and presents strong curvatures of the free surface [43]. Therefore, both cases have a non-hydrostatic pressure distribution.

Due to advances in computational power and the associated reduction in computational time, modern analysis of flow wave pattern can be performed by using 3D numerical models based on Navier-Stokes equations. Direct Numerical Simulation (DNS) is unfeasible as the associated grid resolution causes a substantial amount of computing resource. In consequence, the simulation is restricted to turbulence modeling approaches based on Large Eddy Simulation (LES) and Reynolds-averaged Navier-Stokes (RANS).

 Shigematsu et al. [44] presented a three-dimensional numerical analysis of the water depth in front of the dam during the initial stages. They found a good agreement against experimental data. Abdolmaleki et al. [45] assessed the accuracy of the free-surface elevation

---

[‡] Preliminary numerical results of this test-case study have been published

and pressure peak due to wave impact on the vertical wall. Both studies were based on RANS equations with k-ε turbulence model. Ozmen-Cagatay and Kocaman [46,47] presented an experimental and numerical investigation of dam-break flow without and with a bottom obstacle using models based on RANS and the SWE equations. These authors found that in the first case both models predict the dam-break flow with a reasonable accuracy although the agreement using the RANS model is better. On the other hand, in the second case, the RANS model reproduces the flow under investigation with reasonable accuracy while SWE model indicates some discrepancies due to the presence of the obstacle. Three-dimensional numerical simulations of dam-break flow using the RANS and LES approaches were performed by Larocque et al. [14]. These authors found that both modeling configuration satisfactorily reproduces the measured bottom pressure although the LES captures better the free-surface and velocity variation with time.

The present study aims to assess the performance of LES and RANS turbulence approaches by using a 3D numerical model in a rapidly varying free-surface flow induced by a dam-break problem. In addition, the influence of the non-use of a turbulence model (LAMINAR) in the 3D approach is analyzed. The numerical results are compared against existing experimental data performed by Kleefsman et al. [48]. Therefore, the numerical configurations are used to analyze the ability to capture the temporal variation of flow depth and pressure variables within different locations of the problem domain.

Preliminary three-dimensional numerical results of this test-case study were published in manuscripts performed by Sánchez-Cordero et al. [49,50].

3.3.2   Experimental set-up model

The experimental studies were conducted at the Marine Research Institute Netherlands by Kleefsman et al. [48]. In this dam-break test case, no special in- or outflow boundary conditions are needed. The test set-up was performed in a rectangular horizontal bottom tank of 3.22 x 1 x 1 m (long, wide, high, respectively) with an open roof. At the beginning of the test, the right part of the tank, which is considered as an upstream reservoir, is closed by a door with an initial water depth $H_{4o}=0.55$ m. Then, the gate is opened almost instantaneously and the flood wave reaches the dry downstream flood plain.

A box with a rectangular section and vertical walls, that represents an isolated obstacle, was placed in the flood plain. This obstacle is 0.161 m long, 0.493 m wide and 0.161 m high. During the experiment, water heights and pressures measurements were obtained. As shown in Figure 3.2, four probes were used for the water height, one in the reservoir and the other three in the flood plain; whilst, eight pressure sensors were placed in the box, four on the front and four on the top.
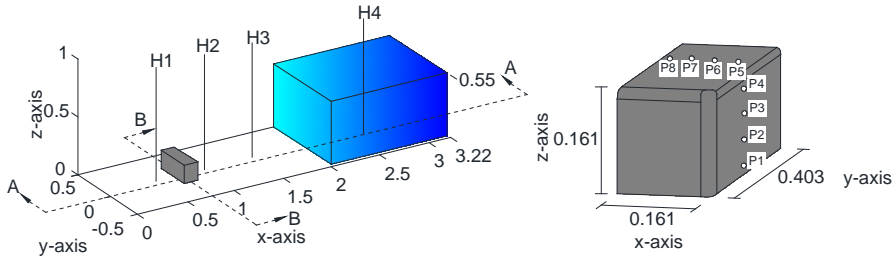
Figure 3.2. Schematic view of the experimental set-up "Adapted from Kleefsman et al.[48]"

3.3.3 Numerical model

In this numerical study, both LES and RANS approaches are used. In the former approach, the Static Smagorinsky model is used while in the latter one the $k - \varepsilon$ RNG model is applied. In addition, no-turbulence model is used which is denominated LAMINAR model. The free surface is tracking by the VOF method.

The static Smagorinsky model implemented in OpenFOAM does not define explicitly the constant C_s. Instead, C_k and C_e constants are used by the Equation (3.1).

$$C_s = \left(\frac{C_k}{C_e}\right)^{\frac{1}{4}}$$

(3.1)

The default values are $C_k = 0.094$ and $C_e = 1.048$ which provide $C_s = 0.168$. The accessibility to the source code allows to modify the C_s value which is highly problem-dependent.

3.3.4 Boundary and Initial conditions

In this numerical test-case, no special inlet/outlet flow boundary conditions are needed, which provides numerical stability in the analysis. A schematic sketch of the boundary conditions is shown in the Figure 3.3-a and Figure 3.3-b (refers Figure 3.2). Therefore, two types of BC are imposed. In the left-wall, right-wall, bottom, and obstacle, a wall-function boundary condition for smooth solid walls is imposed; while at the top of the test-case atmospheric BC is applied.

A water-depth initial condition is imposed, H =0.55 m, Lx= 1.228 m and Ly= 1 m. It represents the initial water volume in the experiment.
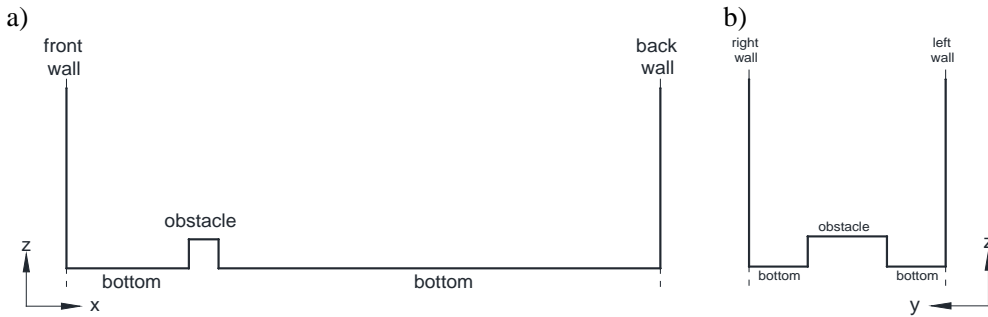
Figure 3.3. Schematic view of the Boundary conditions, a) profile view A-A b) profile view B-B (refers Figure 3.2)

3.3.5   Grid domain configuration

The computational domain was divided into non-overlapping structured hexahedral grid elements with a grid refinement near the bed, walls, and obstacle due to large gradients of flow variables expected in these parts. Therefore, the grid configuration presents non-uniform elements. Starting from the finer grid size, the grid sizes in each direction were progressively increased to obtain the coarse grid size (max.value) with a maximum aspect ratio of 4.

Different lines parallel to the axes are created in order to establish the maximum grid value while the minimum grid value (2.5 mm) is imposed near the walls, bed, and obstacle. Figure 3.4-a shows the A-A cross section (refers to Figure 3.2). In the spanwise direction (y), three lines are established while one in the vertical direction (z). In the same way, Figure 3.4-b shows the B-B cross section where three lines are established in the streamwise direction (x) whereas one in the vertical direction (z).

To obtain grid independent results, a series of grids with different max.value (20, 15 and 10 mm) were tested. Therefore, the final grid configuration was the one such that the resulting deviations were less than 2.5% between the final and the penultimate grids at time t=1s, [51]. This was an empirical criterion used by the author due to the computational time required in the simulation process. The same grid configuration domain is used for all 3D numerical configurations analyzed

a)
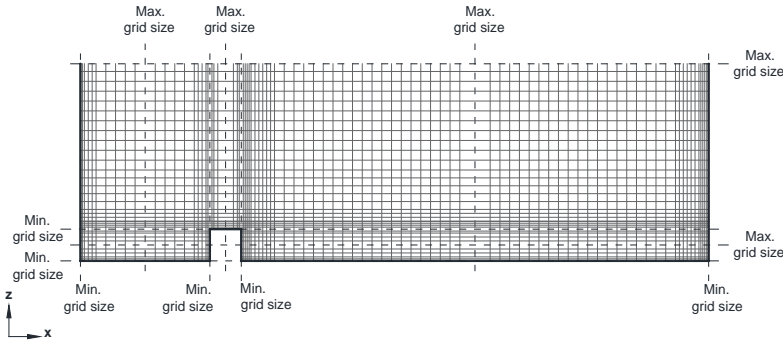
b)
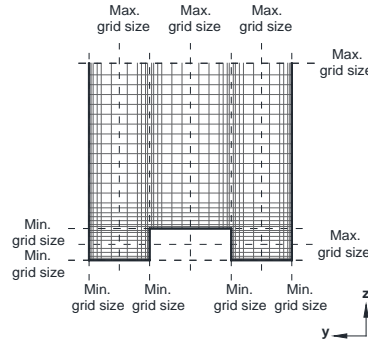
c)
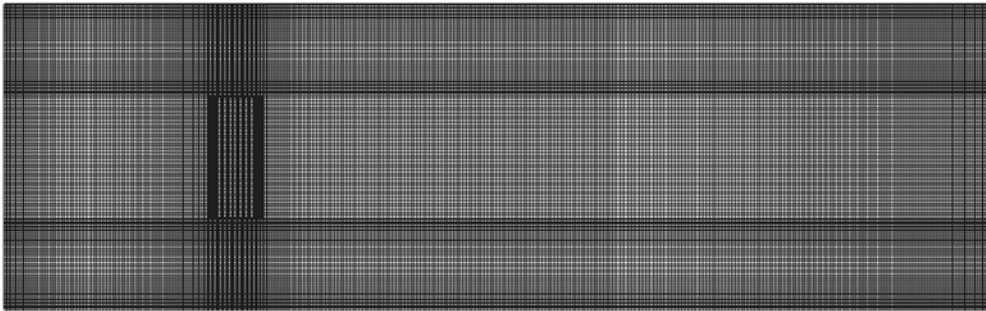
Figure 3.4. Grid domain configuration, a) profile view A-A b) profile view B-B c) Grid domain detail - plan view

3.3.6   Numerical Simulation Schemes

The PIMPLE algorithm is used to solve the pressure-velocity coupling in Navier-Stokes equations. Three loops were applied for the pressure correction. Time derivative terms are discretized using a first-order accurate bounded implicit Euler scheme. The gradient terms are treated using a second-order central difference scheme and a linear interpolation scheme. The convection terms in the Navier-Stokes equations; i.e. mass and momentum, are discretized using a second-order unbounded linear upwind scheme. A second-order Total Variation Diminish (TVD)-scheme with van Leer limiter is used for the volume fraction variable, α. Maximum Courant number of 0.5 is applied, this value maintains numerical

stability. The computational time for this analysis simulation is about 420 hours on an Intel core i7 6700k with 32 GB of RAM computer.

3.3.7   Results and discussion

In order to evaluate the capabilities of the 3D numerical models to reproduce the dam-break flow pattern, the numerical results are assessed against published experimental data described in the section denominated *Experimental set-up model*. Water depth and pressure measurements are used. The experimental data are in a time step resolution of 0.001s, whereas, due to the considerable memory space required, the numerical results were obtained in a time step of 0.01 s. The Coefficient of determination, R^2, is used to quantify the agreement of simulated against experimental data at different locations inside the domain.

Water depth

The water-depth variation with time at different locations in the experimental set-up are shown in Figure 3.6. Note that the 3D models satisfactorily capture the temporal variation at all points of analysis. The variation of the flood wave toe position in the experimental set-up is shown in Figure 3.5.
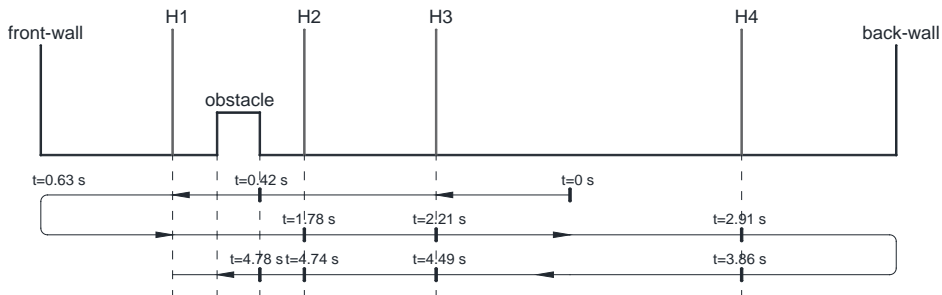
Figure 3.5. Flood wave toe position- a variation on time (profile view A-A)

The flood wave reaches again the probe H2 at t=1.78s, once it first hits the front-wall (t=0.63s). Simulations obtained with the LES model shows a good agreement with the experimental data at this time-period, precisely capturing the peak value; while RANS model displays a time-lag in peak value and LAMINAR model significantly overpredicts the observed water height peak value. The water wave touches the probe H3 at t=2.21 s, LES model shows somewhat closer match than RANS and LAMINAR models, although the three models overpredict the peak value. The probe H4 is reached at t=2.91s, the three models show deficiencies in capture the peak value.

After that, the water flows turn over again to probe H4 (t=3.86) once it hits the back-wall. The moment of the peak value is almost exactly the same in simulations and experiment although the models underpredict the measured data. The second wave meets the probe H3 and H2 at t= 4.49 s and t= 4.74 s, respectively. All three models show a time-lag and

overpredict the peak observed water depth value with the LAMINAR model results deviating farther from the experimental data. A similar analysis can be performed for the rest of the time, although the overall behavior remains the same.

In the probe H1, Figure 3.6-a, which is located between the box and the front-wall, LES model shows close matches with the data even at peak values during the first 1.78 s. Instead, both RANS and LAMINAR models show several spikes in the same period of time with the laminar model results deviating farther from the experimental data.

a)

b)

c)

d)
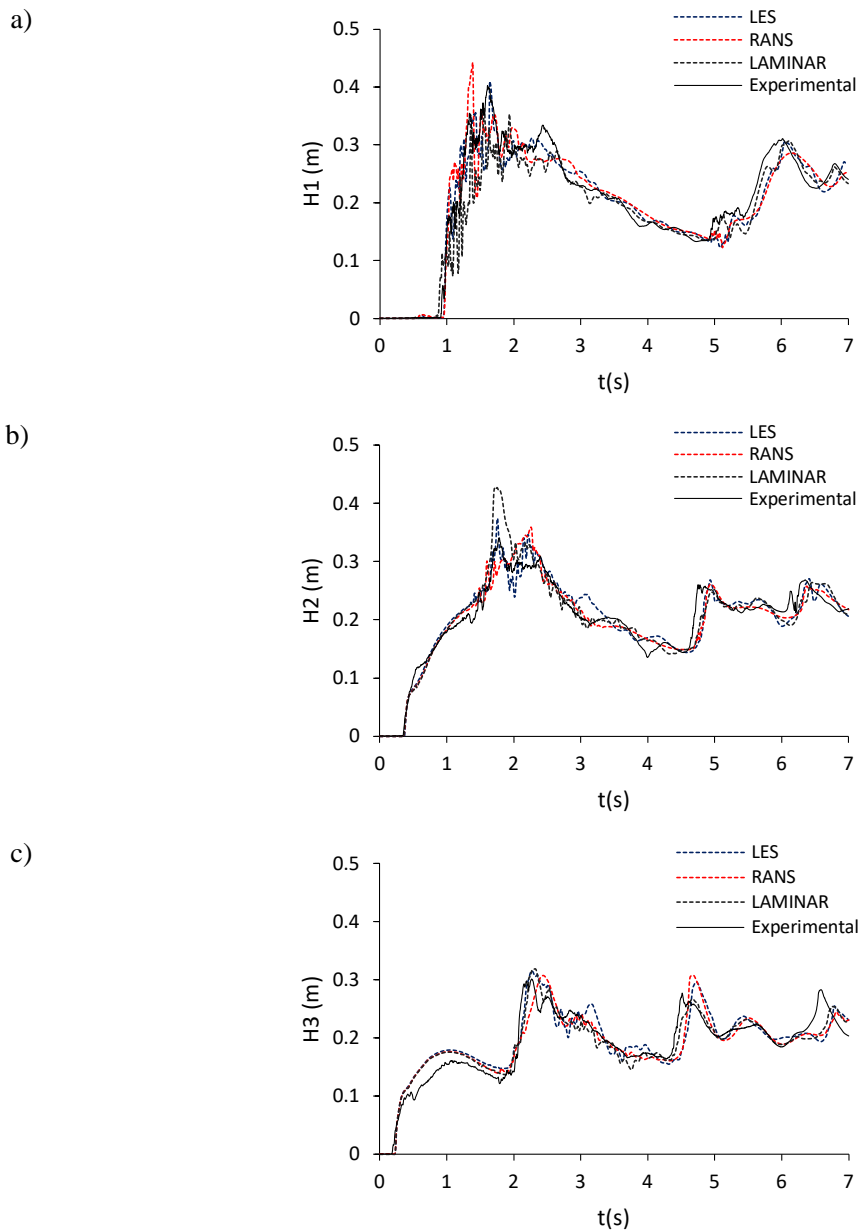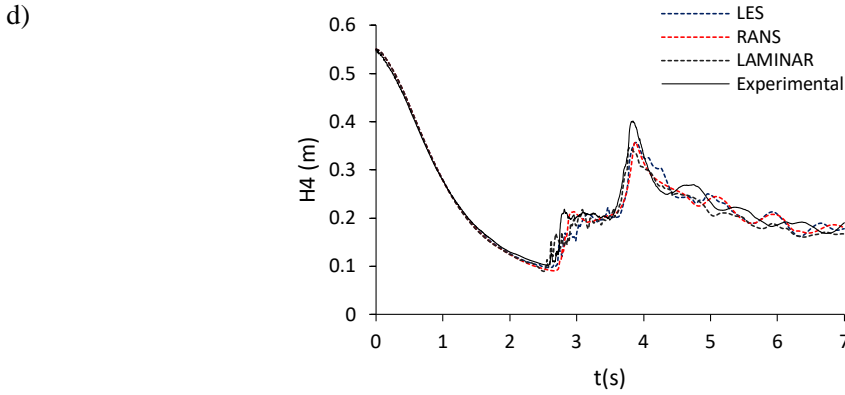
Figure 3.6. Measured and simulated water depths – time variation, a) H1, b) H2, c) H3 and d) H4.

In order to obtain a quantitative measure of the models' performance, scatter plots of simulated against experimental data at different locations and the coefficient of determination, R^2, are presented in Figure 3.7. In addition, a summary of the R^2 values is presented in the Table 3.1.

The results show that the three modeling approaches provide a high coefficient of determination values. Note that in all cases, the LAMINAR model shows lower performance values. Furthermore, the LES model displays lower values of R^2 compared to the RANS model at the positions H2 and H4, but without a significant difference. Similarly, the numerical performance at positions H1 and H2, where the RANS model is better.

The best performance shows the probe H4 (Figure 3.7-d) located inside the tank. Here, the water depth has a slow decline over time during a period following the dam failure (about 2.5s). On the other hand, the lowest agreement is in the probe H3 (Figure 3.7-c). Described so far is consistent as stated in the qualitative description.

a)

b)

c)

d)
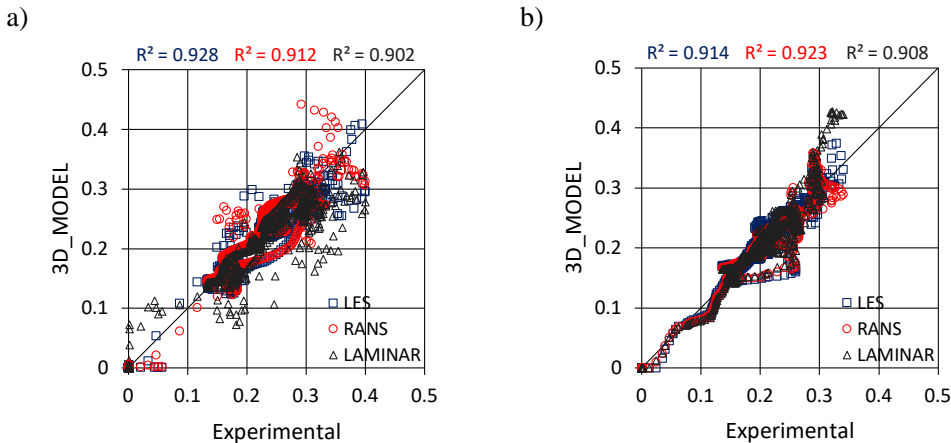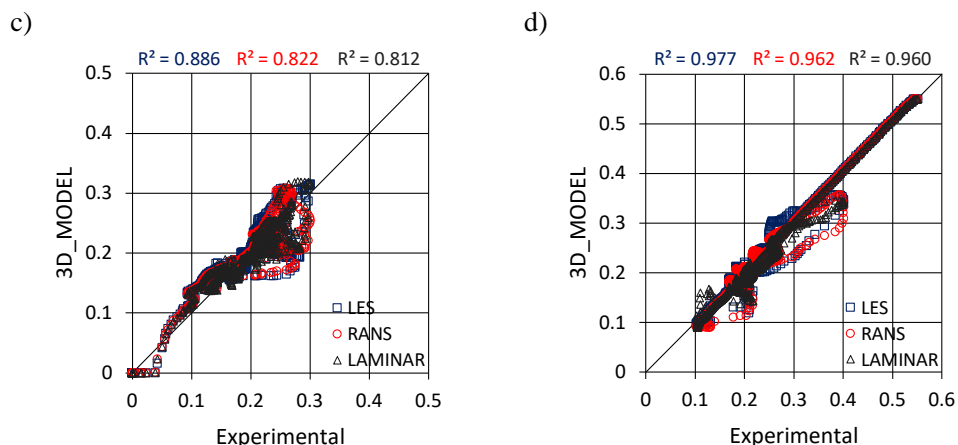
Figure 3.7. Comparison of experimental and simulated water depth values– scatter plots, a) H1, b) H2, c) H3 and d) H4.

Table 3.1. R^2 value- water depth

	R^2			
	H1	H2	H3	H4
LES	0.928	0.914	0.886	0.977
RANS	0.912	0.923	0.822	0.962
LAMINAR	0.902	0.908	0.812	0.960

Figure 3.8 shows the snapshots of a dam-break simulation with the three configuration numerical models at time t=0.56 s. The three models differ in both flood wave toe position and water depth.The LAMINAR model presents a major advance than the other two models in the flood plain, Figure 3.8 –c. In addition, the LAMINAR model shows a greater diffusion of the water sheet after the collision with the obstacle.

a)
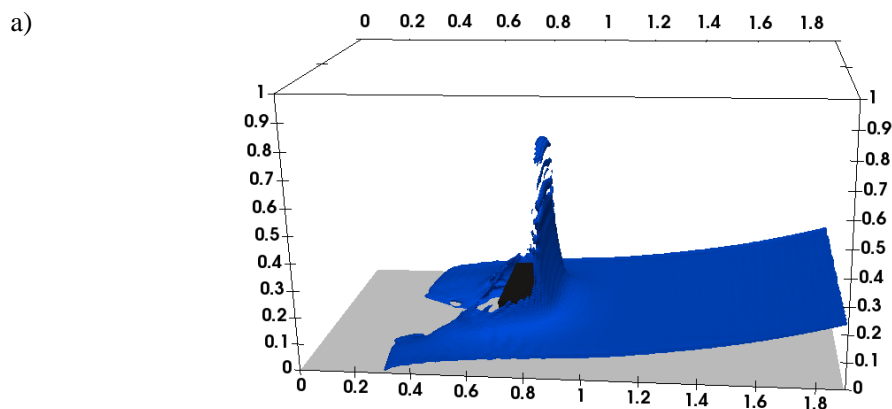
b)
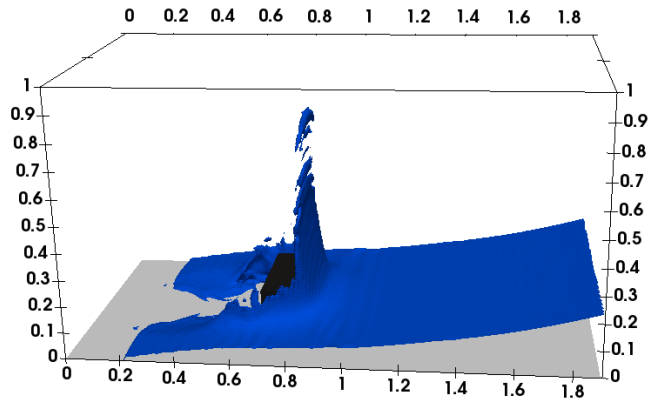
c)
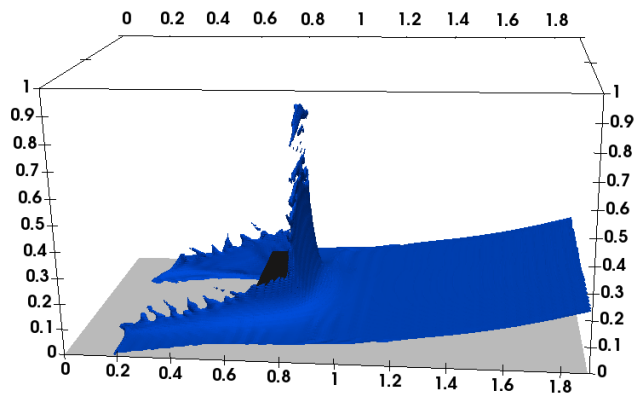
d)

Figure 3.8. Snapshots of a dam-break simulation t=0.56 s. a) LES, b) RANS, c) LAMINAR and d) Experimental photo (taken from Kleefsman et al. [48])

A plan view of the dam-break simulation at time t=0.56 s is shown in Figure 3.9. It can be observed that LAMINAR model shows greater discrepancies against LES and RANS models.
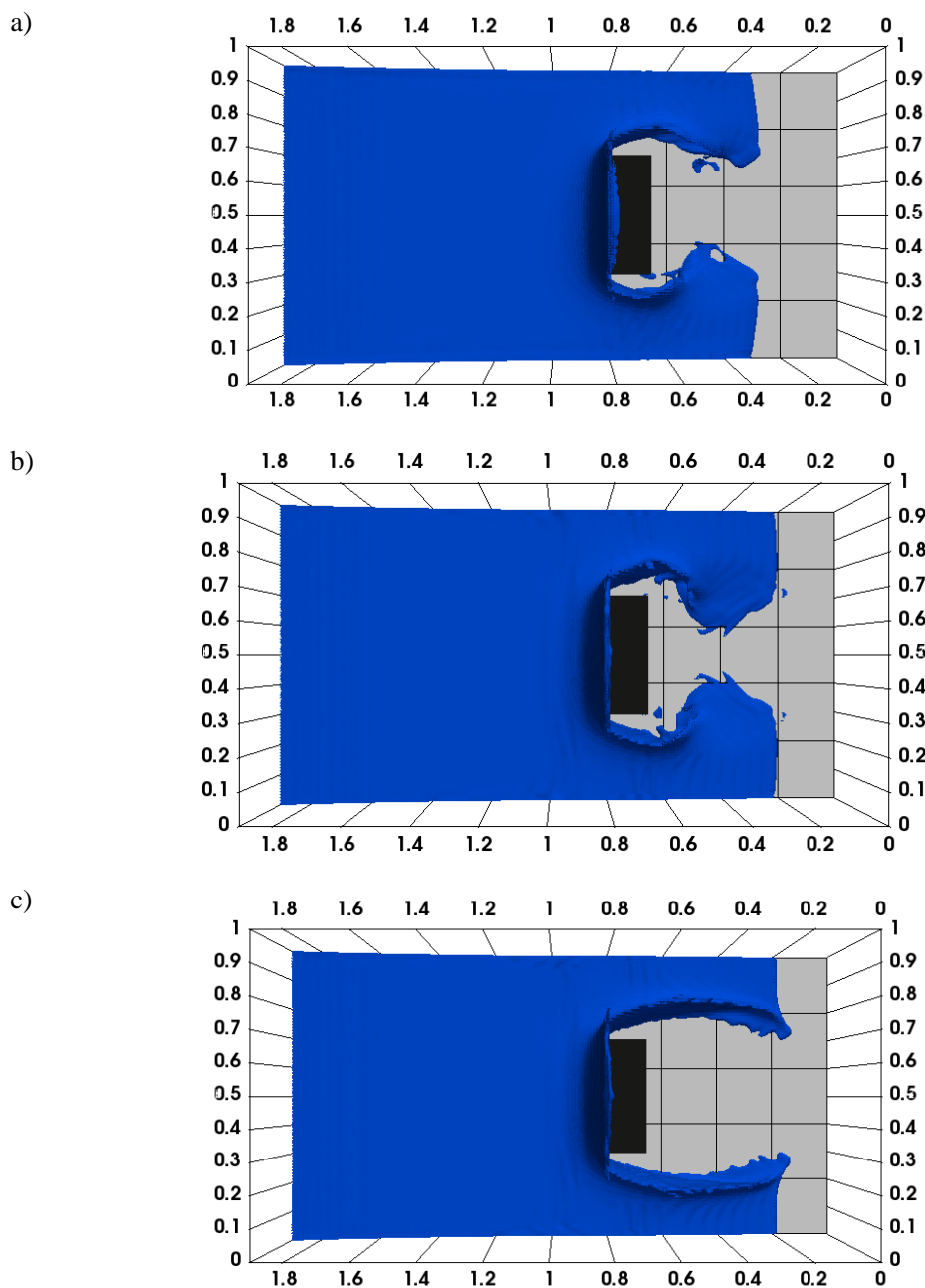
Figure 3.9. A plan view - dam-break simulation t=0.56 s. a) LES, b) RANS, c) LAMINAR

Pressure

A similar analysis to the previous section is presented for this variable. Figure 3.10 shows the time variation of pressure at different points in the box experimental set-up. In order to optimize space in this section, only the pressure analysis at points P1, P3, P5, and P7 are presented. Note that a better agreement between experimental and simulation data is

observed at points at the front of the box (P1 and P3) than the points on top of the box (P5 and P7).

The flood wave hits the box at t=0.42s, showing an almost instantaneous rise of pressure from zero to the peak value. The three models overpredict the magnitude of the pressure value at point P1 (the lowest on the box, Figure 3.10-a), while they underpredict at point P3 (Figure 3.10-b).

The second wave reaches the obstacle at t= 4.78s, a time-lag and difference in peak pressure magnitude are presented at points P1 and P3 by the three models. At points P5 and P7, the results obtained with the LAMINAR model shows a wiggle with several spikes during the first 3s in the simulation, which is not present in the other two models.

a)

b)

c)

d)
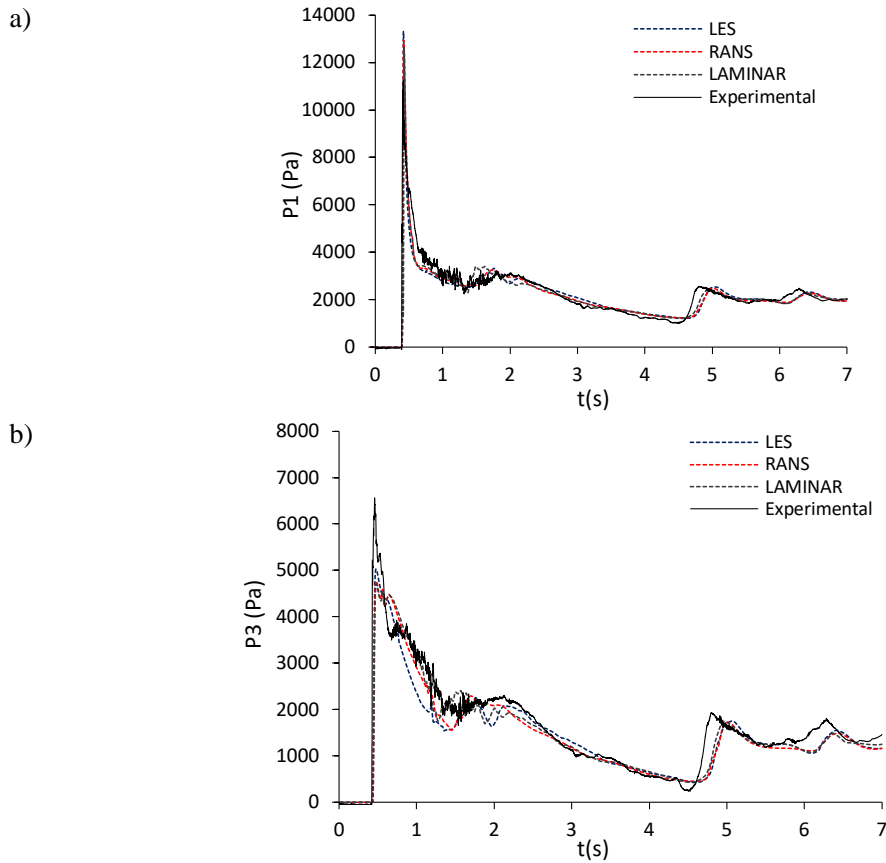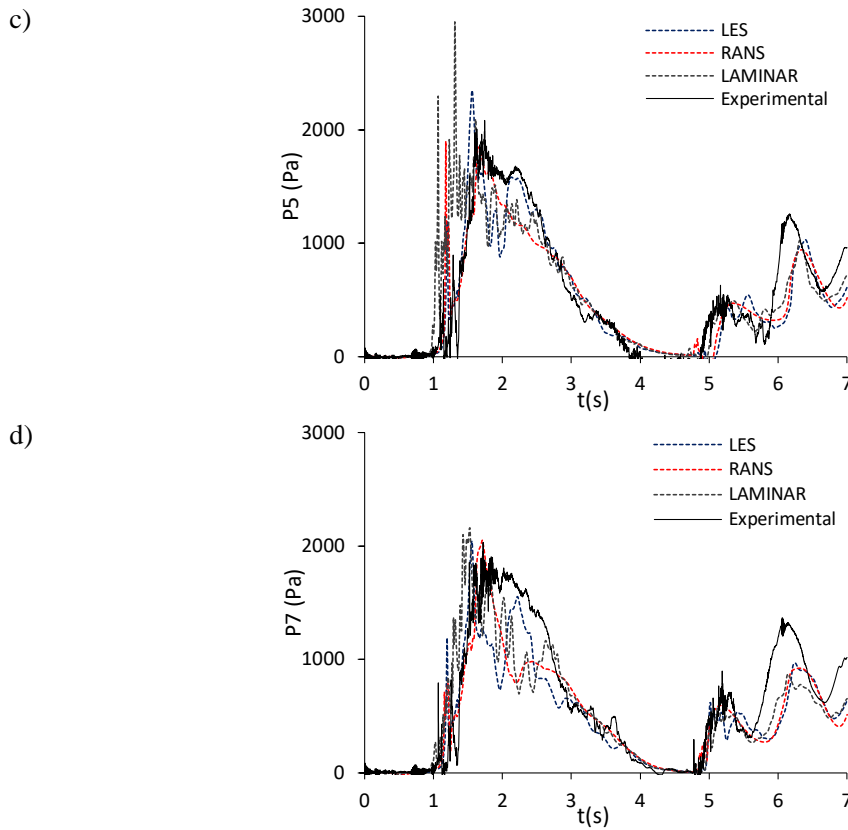
Figure 3.10. Measured and simulated pressure – time variation, a) P1, b) P3, c) P5 and d) P7.

The model performances are quantified using scatter plots of comparison between experimental data and simulation results obtained with LES, RANS and LAMINAR models. In addition the coefficient of determination, R^2, is presented. The LAMINAR model shows lower values of R^2 at the four positions in the analysis, Table 3.2.

Described qualitatively is confirmed using the statistical analysis. Simulations values obtained at positions P1 and P3 (Figure 3.11-a and Figure 3.118-b), located at the front of the box, show a better match with the experimental data than the numerical values obtained at points P5 and P7 (Figure 3.11-c and Figure 3.11-d), located the top of the box, Table 3.2.

Table 3.2. R^2 value -pressure

	P1	P3	P5	P7
		R^2		
LES	0.756	0.829	0.754	0.733
RANS	0.781	0.843	0.781	0.725
LAMINAR	0.750	0.789	0.633	0.652
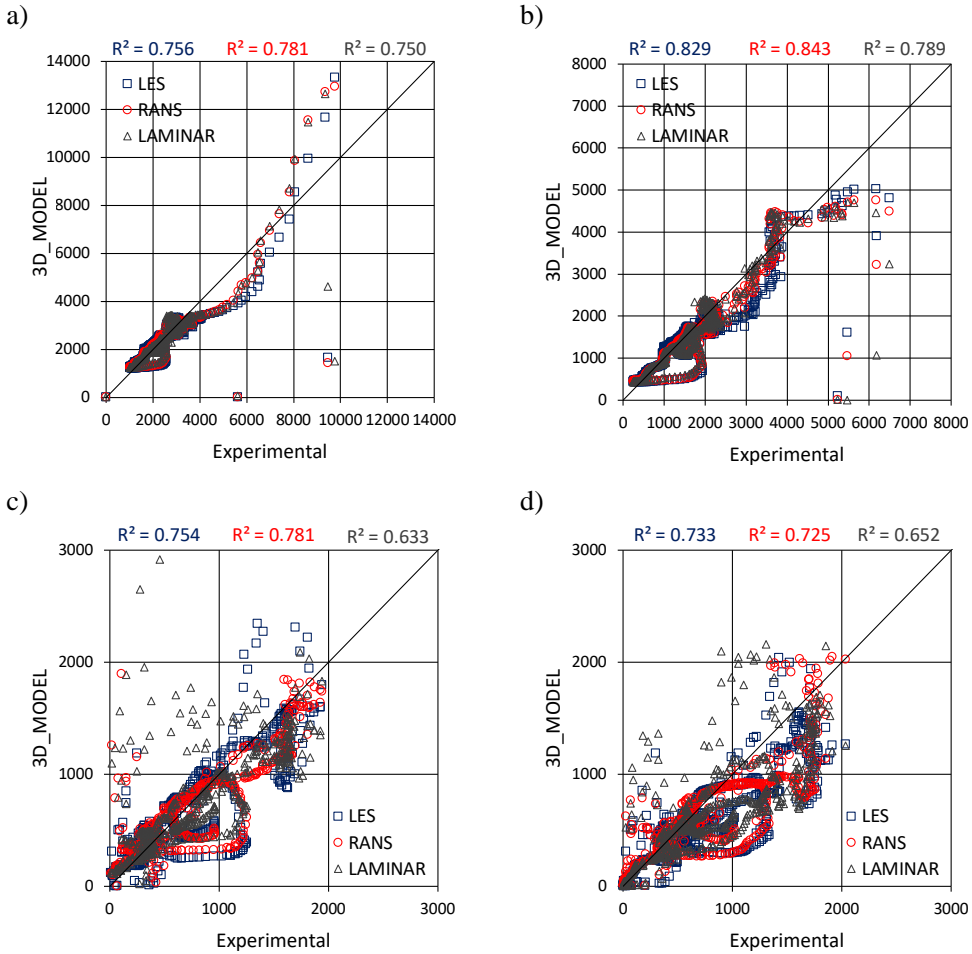
Figure 3.11. Comparison of experimental and simulated pressure values– scatter plots, a) P1, b) P3, c) P5 and d) P7.

3.3.8   Conclusions

In this test-case study, the capabilities of the 3D numerical configuration models to reproduce the dam-break flow pattern, unsteady-state (transient) hydraulic flow condition, are analyzed. The 3D numerical model configurations are based on LES and RANS approaches, and also using a no-turbulence (LAMINAR) configuration. A mesh sensitive analysis is performed in order to ensure the independence of mesh size results. The most relevant observations are listed below

- The 3D numerical configurations show good performance when the results are compared against laboratory experimental data in two hydraulic variables; i.e. water depth and pressure.

- The use of specific 3D numerical approaches; LES, RANS, and no-turbulence (LAMINAR), affects both qualitative and quantitative comparisons.

- The non-use of a turbulence model (LAMINAR) presents lower R^2 performance. Therefore, the results demonstrate that turbulence approach is important in the analysis.

- The R^2 values, show better performances in a water-depth variable than in pressure variable. Note that the water-depth variable presents reliability in laboratory measurement values.

- There is no clear trend to support which turbulence model approach (LES or RANS) produces better adjustments.

In conclusion, the three-dimensional numerical configurations are able to reproduce the dynamics involved in the unsteady-state (transient) hydraulic flow studied. The adjustment of the hydraulic variables; i.e. water-depth and pressure, against experimental values is quite accurate. This allows carrying out a deeper analysis of the hydraulic phenomenon under study.

3.4 Three-dimensional comparative numerical analysis in an open-channel bend.

3.4.1 Introduction

Sharp open channel bend flow is characterized by the presence of a circulatory flow pattern generated in planes perpendicular to the main direction of the motion called secondary flow. Secondary flows are formed due to the disequilibrium in transverse pressure gradient and the driving centrifugal force [52]. The interaction between the main flow and the secondary flow forms a spiral motion, termed helical flow, in the bend, see Figure 3.12. This flow induces important changes in the velocity distribution components, streamlines at different water levels, transport of momentum, and could produce flow separation from boundaries downstream of the bend [53]. Consequently, a detailed and accurate description of the flow structure in an open channel bend is not a simple task and it is of great interest in river engineering.

Although numerical models based on 2D depth-averaged equations are useful to analyze the flow pattern due to their straightforward implementation and application, the flow structures in an open channel bend are highly three-dimensional (3D). Therefore, due to advances in computational power, several studies have been carried out by different investigators [16,51,53–59] to evaluate the flow field in open channel bends by using three-dimensional numerical models based on RANS equations. Likewise, different authors [60–64] performed three-dimensional numerical simulations using the LES approach.

van Balen et al.[65] and Ramamurthy et al. [15] presented a three-dimensional numerical comparative investigation of an open-channel bend flow using different turbulence models based on RANS and LES approaches. These authors identified the importance of the turbulence model, establishing that only those models that can solve all the Reynolds Stress components are appropriates for an adequate representation of the flow structures in an open channel bend.

The objective of the present study is to obtain a comparative assessment of the predictions of the open-channel bend flow characteristic in a stationary regime, using different turbulence models based on LES and RANS approaches. In order to validate the numerical models, the results are compared with laboratory measurements of velocity and water surface elevation obtained by Gholami et al. [16]. Therefore, the numerical models are used to analyze the flow structure along the bend by studying variations of streamlines, components of velocity, and secondary flows.
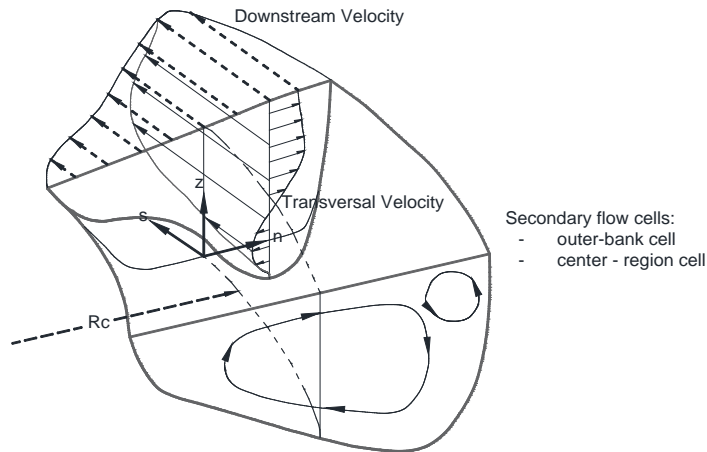
Figure 3.12. Definition variables in an open channel bend – schematic diagram "Adapted from (Blanckaert and De Vried [66])"

3.4.2 Experimental set-up model

The experiment used in this study was carried out in the hydraulic laboratory at the Ferdowsi University of Iran by Gholami et al. [16]. The test set-up, Figure 3.13; consisted of 3.60 m upstream straight channel, a 90° sharp open channel bend, followed by 1.80 m downstream straight channel. The channel was of rectangular cross-section 0.403 x 0.403 m (width x height) made of Plexiglas. Measurements of discharge were done by a calibrated triangle-shaped weir. On the other hand, water depth was measured by a micrometer while the one-dimensional velocity meter PROPLER was used to measure the axial velocity. The accuracy of the micrometer was $\pm$ 0.1mm whilst the velocity meter was $\pm$ 2 cm/s. The experiment was conducted for discharge and downstream water depth fixed values of 25.3 l/s and 15 cm, respectively. Thereby, the flow was subcritical (Froude number= 0.34) and fully turbulent (Reynolds number=44 705).
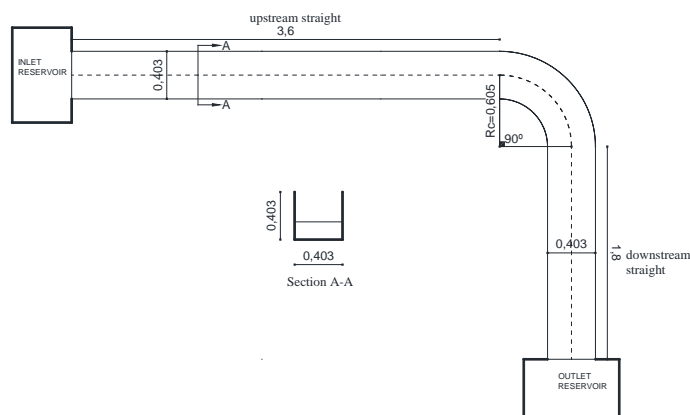
Figure 3.13. A sketch of experimental set-up

The axial velocities were measured in 4 different levels of water depth located at 3, 6, 9 and 12 cm from the bed; and at 13 points along the channel width located at 3 cm apart from the Inner Wall. The measurements were done at a section before the bend (40 cm), two sections after the bend (40 and 80 cm) and three sections in the bend (22.5º, 45º, and 67.5º), Figure 3.14.
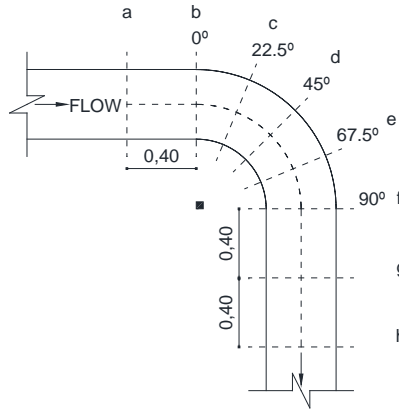
Figure 3.14. Cross-sections positions

3.4.3 Numerical model

In this test-case study, both numerical approaches are used; i.e., LES and RANS. Therefore, the subgrid-scale Reynolds stress (LES) and Reynolds Stress (RANS) are solved by using, Static and Dynamic Smarinsky (LES) and $k - \varepsilon$ (RNG) (RANS). The later model was used as a RANS model as it provides an improved performance for swirling flows around curved geometries [15,67,68]. The volume of fluid (VOF) method is used to simulate the air-water interface.

3.4.4 Boundary and Initial conditions

The experimental set-up was conducted in a steady-state hydraulic condition. In Figure 3.15, the boundary conditions used in the numerical model are summarized. In the inlet BC, a ramping function, which varies in time, is imposed for the velocity profile. The velocity presents a linear variation during $t = 10s$, until the experimental discharge, Q_o , is reached. This strategy provides numerical stability in the simulation process. In the inner-wall, outer-wall, and bottom, a wall-function boundary condition for a smooth solid wall is established. At the top boundary, an atmospheric BC is imposed, which allows the flow to go down and into the channel. As regard the outlet, the subcritical water-depth value, h_{sub}, and a hydrostatic profile is imposed as proposed by [69]. Table 3.3, presents a summary of the boundary conditions, where fV represents fixed value and zG denotes zero Gradient.

Table 3.3. Boundary conditions implemented in the test-case numerical simulation

Boundary	α	$\mathbf{u}$	p	k	ε
inlet	ZG	fV, $\mathbf{u} = f(Q)$	zG	fV*, $k = 1\text{x}10^{-12}$	zG
Inner-wall	ZG	fV, $\mathbf{u} = 0$	zG	zG	zG
Outer-wall	ZG	fV, $\mathbf{u} = 0$	zG	zG	zG
bottom	ZG	fV, $\mathbf{u} = 0$	zG	zG	zG
atmosphere	ZG	fV, $\mathbf{u} = 0$	fV, $p_{\text{total}} = 0$	zG	zG
outlet	$\alpha = 1$ if $z \le h_{\text{sub}}$ $\alpha = 0$ if $z > h_{\text{sub}}$	zG	fV, $p_{\text{total}} = f(h)$	zG	zG

In regard to initial conditions, water depth and velocity values are imposed in the computational domain; i.e. 0.15 m and 0.40 m/s, respectively. The latter value is based on the average velocity (discharge/ section area) which provides a better numerical convergence.
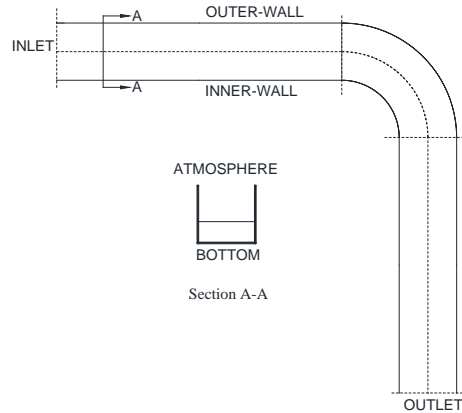
Figure 3.15. Description of the boundary conditions- A schematic view

3.4.5   Grid domain configuration

In this test-case study, the experimental set-up domain size is reduced in order to optimize the computational time required. Therefore, in the numerical domain, the upstream straight reach is 2m while the channel depth is 0.30 m. The former measure was adopted because it is adequate for the complete development of the variables under study, while the latter one is the large enough in order to avoid the top BC influence.

The computational domain was divided into non-overlapping structured hexahedral grid elements. A grid refinement near the bed, walls, and the water surface is needed because large gradients of flow variables are expected. Consequently, the grid configuration presents

non-uniform elements. Starting from the finer grid size, the grid sizes in each direction were progressively increased to obtain the coarse grid size ($max.value$). The grid sizes increase with a maximum aspect ratio of 4.

Figure 3.16 shows the grid alignment with the flow direction. The grid size in the streamwise direction varies according to the proximity of the straight reaches to the bend, with the smallest value close to it $[5 - 10]$ mm.

a)
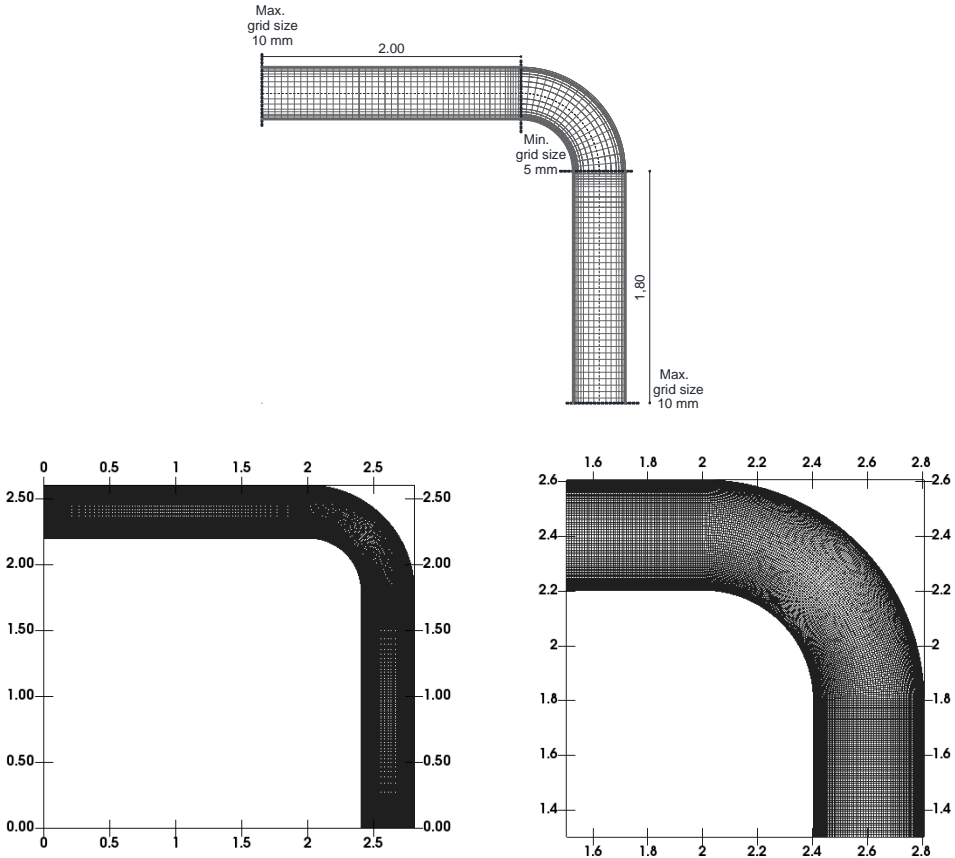
Figure 3.16. a) Grid domain configuration detail - plan view b) Grid domain configuration - plan view c) Bend configuration - detail

Figure 3.17 illustrates the grid size in the spanwise direction from inner-wall and outer-wall to channel axis $[2.5 - max.value]$ mm. On the other hand, the grid is refined vertically close to the bed and near the water interface $[2.5 - max.value]$mm.
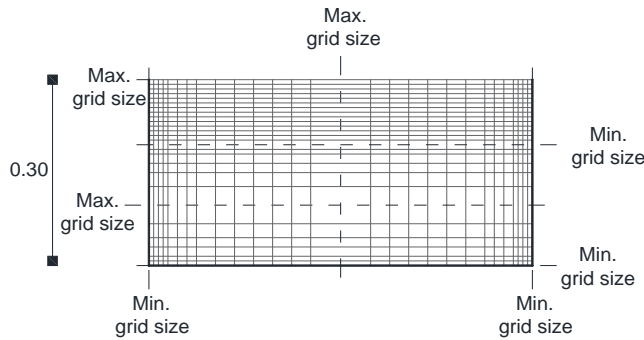
Figure 3.17. Grid domain configuration - cross section

In order to ensure grid independence on the results, three different grid configurations based on a maximum grid size value (20, 15 and 10) mm were tested.

Therefore, the values of velocity, pressure, and water-depth into the domain were analyzed at $t = 15\ s$, once the flow reaches the outlet BC. However, this was an empirical criteria assumed by the author due to the computational time required. The deviations of the variables between the final and penultimate grid were less than 2.5% [70].

Consequently, the grid resolution used in the analysis of the results, for the three numerical models, has a maximum grid size value of 10 mm.

3.4.6   Numerical Simulation Schemes

In this study, the PIMPLE algorithm is used to solve the velocity-pressure coupling. A second-order implicit backward discretization scheme is applied for the temporal term. The use of implicit approach provides numerical stability but it implies longer computational simulation time [71]. The gradient terms are treated with a second-order central differencing scheme and a linear interpolation scheme. The convection terms in governing equations; i.e. momentum and mass, are discretized using the second-order central difference scheme based on a Sweby limiter. The flow fraction convective term, α, is discretized with a second-order Total Variation Diminish (TVD)-scheme with van Leer limiter. The time step is automatically updated with a Maximum Courant number 0.5. The computational time for this analysis simulation is about 390 hours on an Intel core i7 6700k with 32 GB of RAM computer.

3.4.7   Convergence criteria

The simulation was assumed to have reached a steady-state hydraulic characteristic, using empirical criteria, when the residuals of the variables; i.e. velocity, pressure, and water-depth, were less than $1\mathrm{x}10^{-3}$ and the difference between the inlet and outlet discharge values was less than 2.5 %.

3.4.8   Model Verification

Water Depth

Transversal water profiles comparison between numerical simulation data against experimental measurement values using three model configurations approaches in the different sections are presented in Figure 3.18. The model configurations, i.e. $k - \varepsilon$ RNG, LES Static Smagorinsky and LES Dynamic Smagorinsky, show an adequate agreement with the experimental data measurements.

While the flow remains in the straight channel parts, upstream and downstream, Figure 3.18, the water surface is linear and the match between the numerical models results and the experimental data is quite accurate. This occurs at the beginning and ending sections of the channel (section a and section h).

Major discrepancies happen in section b to section f, which are in the bend part of the experiment. Here, the centrifugal force generates a transverse slope at the water surface where the water level increases near the outer wall and decreases at the inner wall. The experimental data provided by Galomhi, show that the transversal slope is non-linear and it has greater gradients near the inner wall than near the outer wall.

It can be seen that the 3D model based on RANS approach presents the transversal slope gradient values with a slight variation for all the sections. On the other hand, both models based on LES approach, show greater transversal slope gradient values near Inner-wall.

The section f shows the greatest differences in shape and values between the experimental measurements and simulated data. Thus, the maximum under-estimated values differ in 2.2 mm, 4.9 mm and 5.8 mm for $k - \varepsilon$ RNG, LES Static Smagorinsky and LES Dynamic Smagorinsky models, respectively. In addition, in all the sections analyzed, the Smagorinsky dynamic model underestimates the measured values.

a)
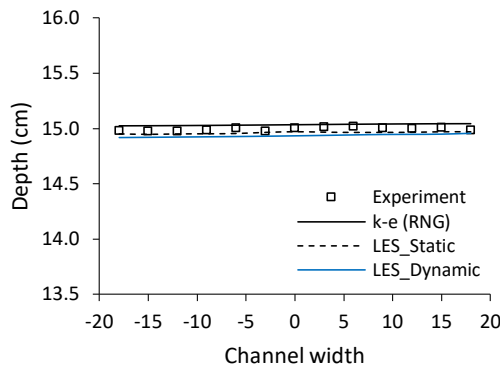
b)
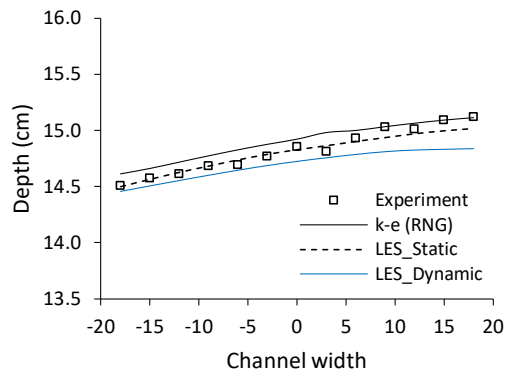
c)
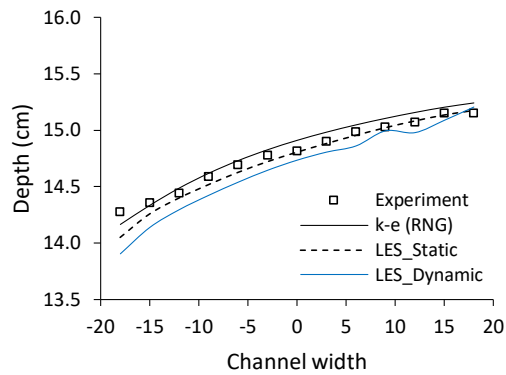
d)
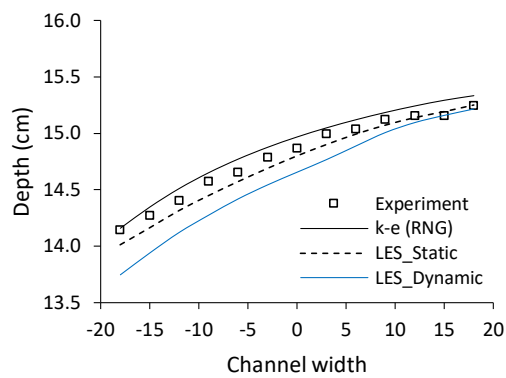
e)
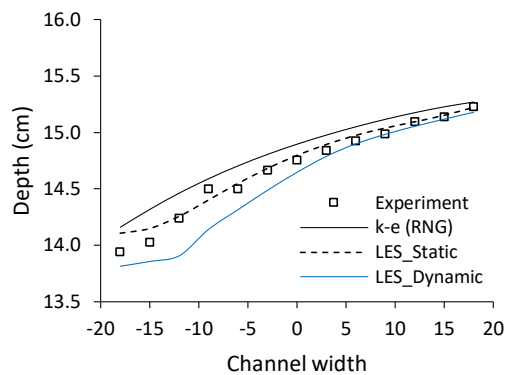
f)
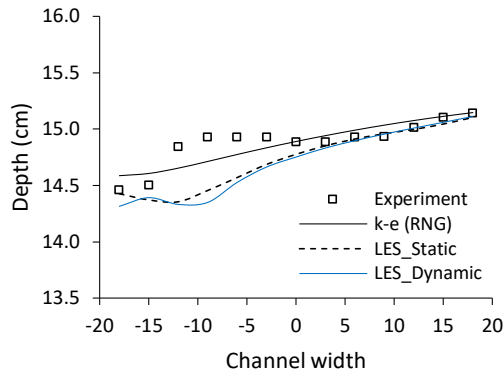
g)
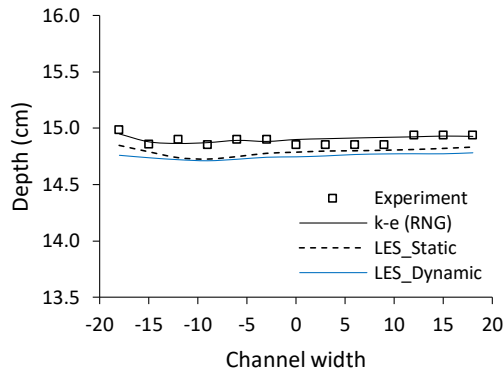
Figure 3.18. Measured and simulated water surface

Figure 3.19 shows the snapshots of a water surface in the channel bend. The three models differ in shape. In addition, LES dynamic model shows greater variation.

a)

b)
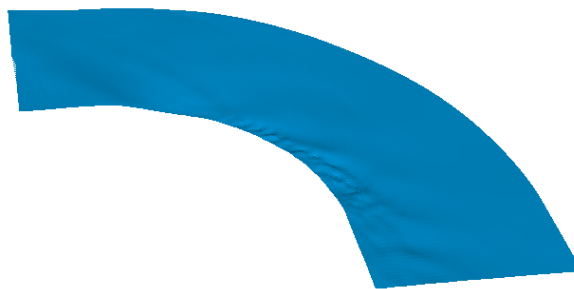
c)
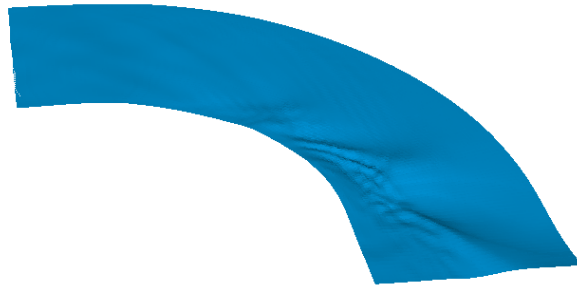
Figure 3.19. Water surface – snapshots a) RANS, b) LES static, and c) LES dynamic

Measured and simulated water surface

Table 3.4 shows the Root Mean Square Error (RMSE) and Mean Absolute Error values in order to measure the performance of the of the three models against laboratory data. Note that the k-e (RNG) model shows a better performance in RMSE and MAE average value; however, in the bend channel sections, LES_static model presents a better performance.

Table 3.4. Water-depth statistic values

Cross section	water-depth					
	RMSE (cm)			MAE (cm)		
	k-ε (RNG)	LES_static	LES_dynamic	k-ε (RNG)	LES_static	LES_dynamic
a	0.096	0.108	0.403	0.097	0.109	0.403
b	0.225	0.042	0.279	0.231	0.054	0.291
c	0.218	0.049	0.221	0.225	0.075	0.241
d	0.188	0.071	0.295	0.19	0.08	0.317
e	0.302	0.055	0.272	0.309	0.073	0.293
f	0.126	0.303	0.556	0.138	0.349	0.588
g	0.03	0.395	0.638	0.038	0.397	0.639
h	0.086	0.523	0.729	0.089	0.523	0.729
average	0.159	0.193	0.424	0.165	0.208	0.438

Longitudinal velocity profiles

In order to obtain more qualitative results of the flow field, the longitudinal velocity profiles are analyzed in some cross sections. Figure 3.20 shows the comparison profiles at the beginning of the bend channel, section b; at the middle of the bend, section d; and at the end of the bend channel, section f. The velocity profiles from the numerical results and the experiment shown in general a reasonable agreement.

The presence of the secondary flow in the bend is responsible for local variations of velocity components [53]. At the beginning of the bend, the influence of the secondary flow is not significant and the maximum velocity occurs near the water surface and near the inner

wall. In the mid sections of the bend, the influence of the secondary flow is evidenced, where the maximum longitudinal velocity moves towards the outer wall and near the channel bed. At the end of the bend, major changes in the longitudinal velocity are exposed, which causes that the maximum velocity occurs near the outer wall. These flow characteristics have been reported by [16,53]. Note that LES static Smagorinsky results present better match than dynamic Smagorinsky data.

a)
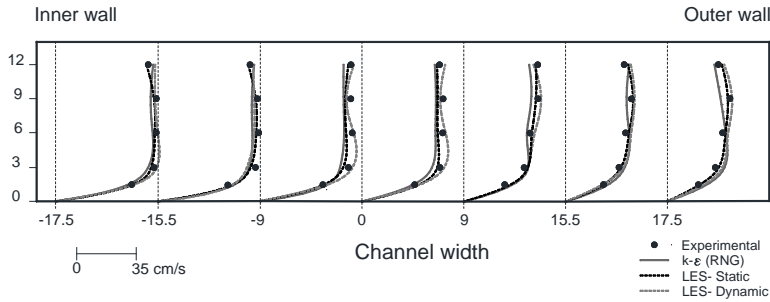
b)
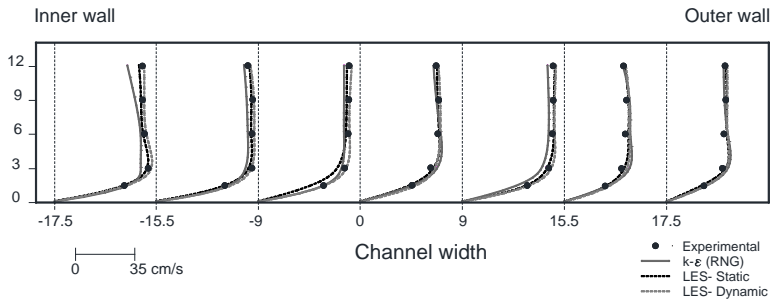
c)
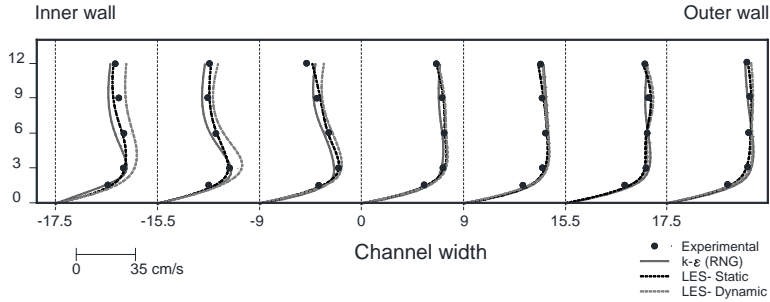
Figure 3.20. Measured and simulated profiles- longitudinal velocity component a) section b, b) section d and c) section f.

Streamlines

The secondary flow in the bend is the result of the local imbalance between the centrifugal force and the water surface gradient. According to Blanckaert and De Vried [66], turbulence is important in the generation of the outer-bank cell (minor secondary flow).

The numerical results presented herein show the presence of the double-cell pattern; i.e. main secondary flow and minor secondary flow. In order to optimize space in this item, only two cross sections are presented. Figure 3.21 shows the cross section c and section f.

The main secondary flow moves downstream of the bend. The center of the main secondary flow moves along the bed moving from the outer wall toward the inner wall. In contrast, a minor secondary flow with opposite direction is formed near the outer wall and near the water surface. Therefore, the three numerical configurations show the described characteristics. These characteristics were exposed in the studies performed by [16,53].

However, according to the numerical model used, the size of the secondary flows is different. Major discrepancies in the form of secondary flows occur at the end of bend where the LES models presents a steeper gradient near outer wall.
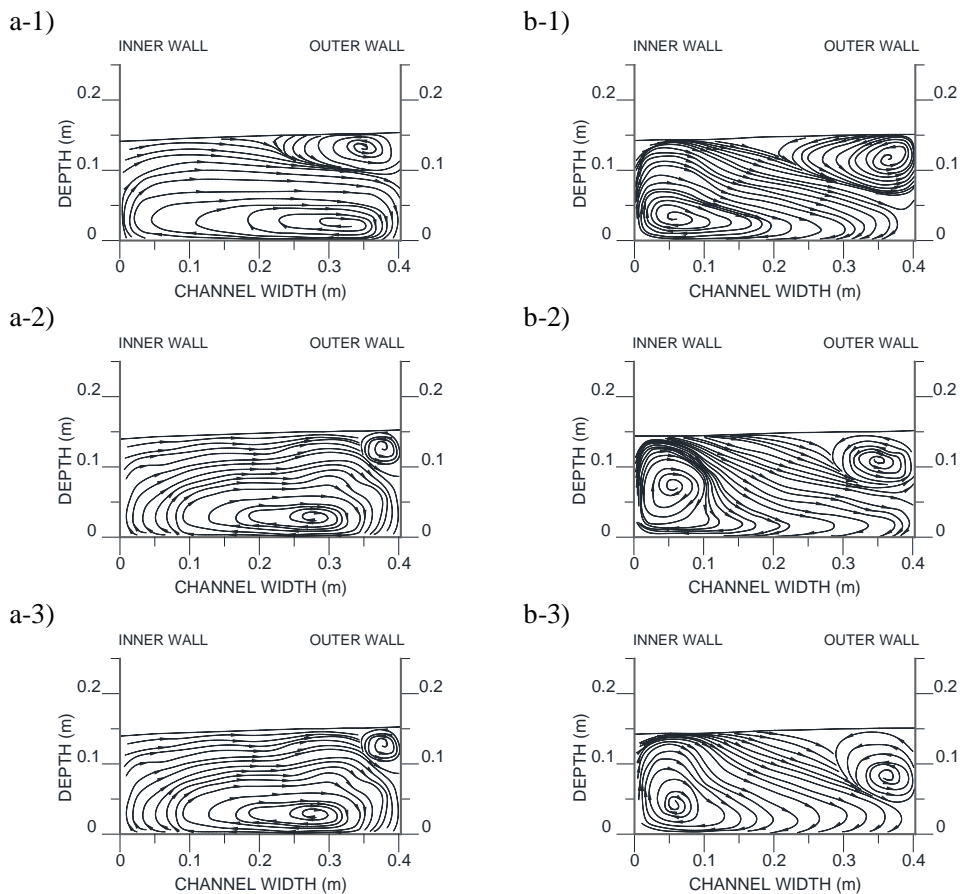
Figure 3.21. Streamlines at the established sections, a) section c b) section f.
$k - \varepsilon \, (RNG)$[1], LES_static[2] and LES_dynamic[3].

3.4.9 Conclusions

In this test-case study, a comparative assessment of the flow characteristic using three numerical configurations based on LES and RANS approaches is performed. In the former approach Static and Dynamic Smarinsky models are used while in the last approach k-ε (RNG) is implemented. A mesh sensitive analysis was conducted in order to determinate an adequate grid size. The numerical results are assessed against experimental observations; i.e. water-depth and longitudinal velocity component. The main conclusions of this study are listed below

- Three numerical model results present an acceptable level of agreement in the variables analyzed; i.e. water level and longitudinal velocity component.

- Water depth values are better predicted in sections at the beginning and the end of the bend, where the influence of the secondary flow is lower.

- Local variations of velocity components are presented in the channel due to the secondary flow influence. The pattern of these variations coincides with previous studies.

- The major discrepancies of the simulated values occur in the mid sections of the channel bend, where the influence of the secondary flow is significant.

- The three-numerical models reproduce the two secondary flows along the bend channel; i.e. main and minor. The center of the main secondary flow moves along the bed moving from the outer wall toward the inner wall. In contrast, a minor secondary flow with opposite direction is formed near the outer wall and near the water surface.

In conclusion, a three-dimensional numerical model can predict the various trends of the water-depth and velocity profiles based on both the geometry of the channel and the magnitude of the discharge. Therefore, the numerical models can assist in the design and evaluation of hydraulic channels.

3.5 Three-dimensional numerical analysis of free-surface flow in a sharp open-channel bend influenced by a weir and a sluice gate[‡]

3.5.1 Introduction

Flow in open channel bends is characterized by secondary flows, flow separation, energy losses, and water surface variations. Secondary flows result from the imbalance between centrifugal force and pressure gradient leading to the water particles near the surface are driven outwards [72]. The interaction between the main flow and secondary flow forms the so-called helical flow in the bend, which has important consequences in the velocity distributions, transport of momentum, and streamlines at different water levels [53]. Therefore, the study of flow patterns in a channel bend is not a simple task and has a great interest within the hydraulic design practice. Due to advances in computational power and the associated reduction in computational time, three-dimensional (3D) models based on Navier-Stokes equations have become a feasible tool to analyze the flow pattern of various geometries and boundary conditions.

Early open-channel bend studies [52,73,74] provided considerable attention to secondary flow characteristics without emphasis on the flow separation. de Vriend [75] presented a theory of secondary flows profiles for non-asymmetric steady flow in shallow and curved channels with a fixed bed. Kalkwijk and de Vriend [76] presented a mathematical 2D model to describe the flow in rivers taking into account bottom friction, flow curvature, and transverse convection of momentum by the secondary flow. de Vriend [77] analyzed the velocity redistribution in curved rectangular channels. This author presented a shallow water mathematical model for steady incompressible laminar flow. Shimizu et al. [78] developed a 3D numerical model whose results were compared with experimental data and 2D numerical results obtained from the model proposed by Shimizu and Itakura [79]. They concluded that the flow field is predicted more accurately by the 3D model than the 2D model. Therefore, the applicability of 3D models is presented when the understanding of the flow field is required. Several studies have been carried out by different investigators [54,57,80,81] to evaluate the flow field in open-channel bends by using three-dimensional numerical models. More recently, Naji Abhari et al. [53] studied flow pattern in a channel bend, experimentally and numerically by applying a three-dimensional numerical model, SSIIM. The results showed that the flow pattern in a channel bend is influenced widely by the secondary flow and the centrifugal force. Han et al. [51] using two commercial three-dimensional numerical codes, PHOENICS and FLUENT, computed the flow in sharp open-channel bends with vanes validating against laboratory measurements. They found that vanes are effective to reduce the secondary flow intensity and flow separation along the inner wall. Ramamurthy et al. [15] simulated flow pattern in a sharp bend by using two commercial

---

[‡] The data in this test-case study, have been prepared as a manuscript for a possible publication

three-dimensional numerical codes (PHOENICS and FLUENT) along with different turbulent models, and by comparing the numerical and experimental results. These authors identified that an adequate representation of secondary flow in the channel downstream of the bend requires both the appropriate treatment of the channel free surface and a proper turbulence model. Gholami et al. [16] presented an experimental and a three-dimensional numerical study of the flow patterns in a sharped open channel bend. The numerical modeling was carried out using the commercial code FLUENT. In that study, they analyzed the patterns of secondary flow, longitudinal velocity contours, and shear stress. The authors found that along a sharped channel bend, the maximum flow velocity always occurs near the inner wall and in such bends, the effect of the secondary flows is not limited to the sections within the bend.

The objective of this test-case study is to analyze the flow fluid characteristics obtained from the 3D numerical results in a real scale sharp open-channel bend influenced by a weir and a sluice. To the author's knowledge, 3D numerical modeling of this channel geometric configuration has not been reported in the literature. The sensitivity of the numerical code to three RANS turbulence models; $k - \varepsilon$, $k - \omega$, and $k - \varepsilon$ (RNG), and mesh element size is assessed. The numerical model was assessed according to water depth experimental data performed by Gómez and Martínez-Gomariz [82]. In addition, a roughness parameter has been calibrated to set a reliable model. Therefore, the numerical model was used to analyze the flow pattern along the sharp bend by studying variations of streamlines, components of velocity, and secondary flows.

3.5.2 Experimental set-up model

Experiments were carried out at the hydraulic laboratory of the Technical University of Catalonia. The PAC-UPC channel "Canal de Pruebas de Algoritmos de Control (Test Canal Algorithms Control) - Universitat Politècnica de Catalunya (Technical University of Catalonia)" is specially designed to develop basic and applied research in the irrigation channel control area. The channel has a snake shape in its 220 m long construction with a rectangular cross-section of 0.44 m wide and 1 m deep. The channel has zero slope in order to achieve the largest possible time delay. The bed and side walls of the channel are made of concrete while the vertical sluice gates and rectangular weirs are made of methacrylate and PVC respectively. The bend where W1 weir and G3 sluice gate are located was chosen for this study because the discharge value is known with appropriate accuracy (Figure 3.22-a). Discharge measurements were carried out through a calibrated V-notch weir and water depths were measured in 10 locations. Two water level sensors (Figure 3.23), which have an accuracy of 0.1mm, were used for measurements at locations 3 and 10 whilst the rest of the depths were measured by a limnimeter with 1 mm of accuracy (Figure 3.22-b).

Gómez and Martínez-Gomariz [82] obtained the data from experiments in steady flow condition. Table 3.5, shows the data of discharge (Q), sluice gate opening (a), and weir height

(w) stabilized according to Figure 3.22-c. The flow was subcritical (Froude number≈0.1) and fully turbulent (Reynolds number≈ 1.95×10^5). The discharge through the weir W1 was measured (0.017 m^3/s) [83].

Table 3.5. Hydraulic and geometric characteristics – experimental set-up

Flow Rate Q	w	a	water depth (m)									
m^3/s	m	m	1	2	3	4	5	6	7	8	9	10
0.094	0.643	0.170	0.740	0.737	0.727	0.729	0.735	0.740	0.742	0.730	0.735	0.600
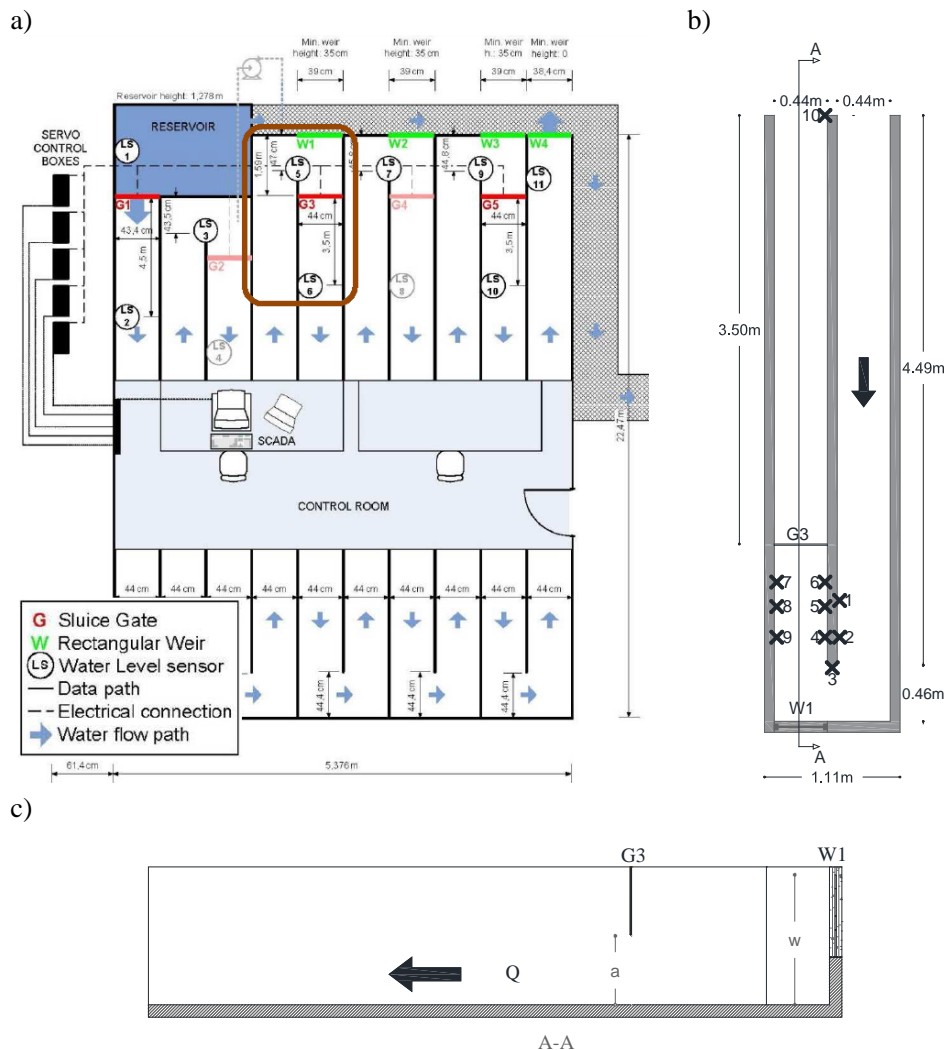
Figure 3.22. a) Schematic layout of UPC laboratory channel "adapted from Gómez and Martínez-Gomariz [82]", b) Schematic view of the channel bend - points for measurements, c) Detail of Section A-A

a)   b)
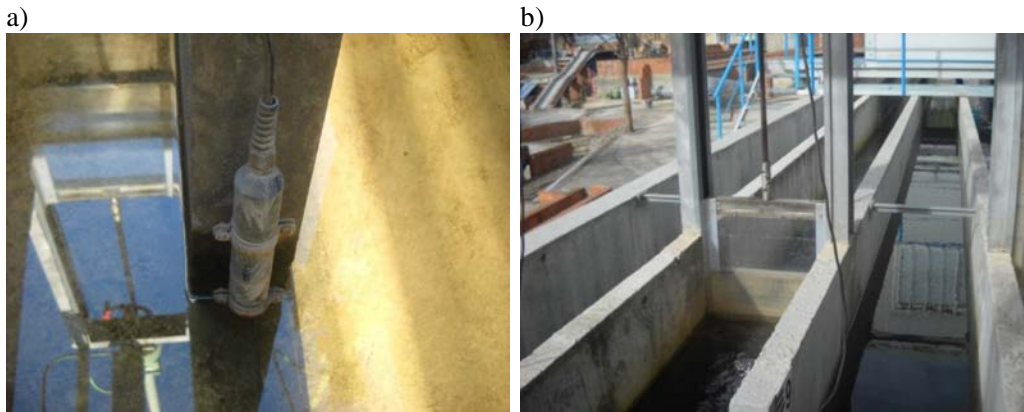
Figure 3.23. UPC laboratory channel photos: a) Level sensor, b) sluice gate (taken by Gómez and Martínez- Gomariz [82])

3.5.3   Numerical model

The governing equations for the fluid flow in this test-case, are the incompressible Reynolds-averaged Navier Stokes (RANS) equations. Turbulence is treated using three models; i.e. $k - \varepsilon$, $k - \omega$, and $k - \varepsilon \, (RNG)$. The free-surface is tracked by mean the Volume of Fluid (VOF) method.

3.5.4   Boundary and Initial conditions

The boundary conditions of the computational domain are one inlet, two types of outlets (which depend on flow conditions), atmosphere, walls, and bottom (Figure 3.24).
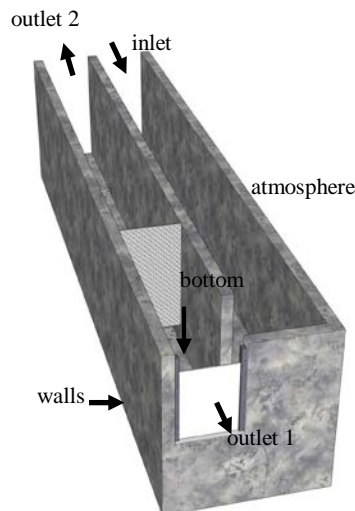
Figure 3.24. Schematic view of boundary conditions

Inlet

In the analyzed test-case, the steady-state flow condition is reached for a given discharge rate, Q_o. In order to provide a numerical stability, a ramping function is imposed to the velocity boundary condition. The time-variation velocity is gradually incremented until the maximum velocity value matches to the one calculated with Q_o.

Therefore, a velocity profile based on flow rate is specified, Dirichlet boundary condition. Pressure is defined by a Neumann boundary condition with a zero normal gradient, $\partial p / \partial \mathbf{u}$, to be consistent with the velocity condition [69]. Turbulence quantities are set as a constant values calculated according to the flow conditions.

Outlets

Two types of outlet boundary conditions are placed in this research. In the first condition, outlet 1 (weir), zero gradient conditions $\partial / \partial n = 0$, Neuman conditions, are applied for all quantities.

At the second condition (outlet 2), the hydrostatic pressure changes with the free surface. Therefore, in order to specify the pressure BC, the dynamic component $\rho \mathrm{u}^2 / 2$ is specified as a zero normal gradient, and the hydrostatic pressure is subtracted from the total pressure. Velocity and turbulence values are defined by a Neumann boundary condition with a zero normal gradient. Details of this outlet free surface condition can be found in [4,69].

Atmosphere

At the top boundary of the channel, an atmospheric boundary condition is imposed to allow the flow to enter and leave the domain. The total pressure is set to zero, Dirichlet condition. The other variables are calculated according to the flow direction by means a zero gradient, Neumann condition.

Walls and bottom

At the surface of the walls and bottom of the channel, a wall-function boundary condition for the rough wall is established. No-slip condition, $u = 0$, Dirichlet condition, is set for the velocity with zero pressure gradient, Neuman condition.

A water-depth initial condition is imposed into the channel, H =0.60 m.

3.5.5   Grid domain configuration

A grid independent solution implies that the results do not change significantly when increasing the number of grid cells. The grid-independent results are obtained through a sensitivity analysis. The domain is discretized by using non-uniform structured Cartesian hexahedral elements. The large gradients of flow expected; near walls and bottom, impose mesh densification in their vicinity, minimum grid value (2.5 mm).

Different lines parallel to the axes are created in order to establish the maximum grid value, (max.value); i.e. 40, 20, 10 mm. Starting from the finer grid size, the grid sizes in each direction were progressively increased to obtain the coarse grid size (max.value) with a maximum aspect ratio of 2. The grid-configuration is shown in Figure 3.25.

a)

b)

c)
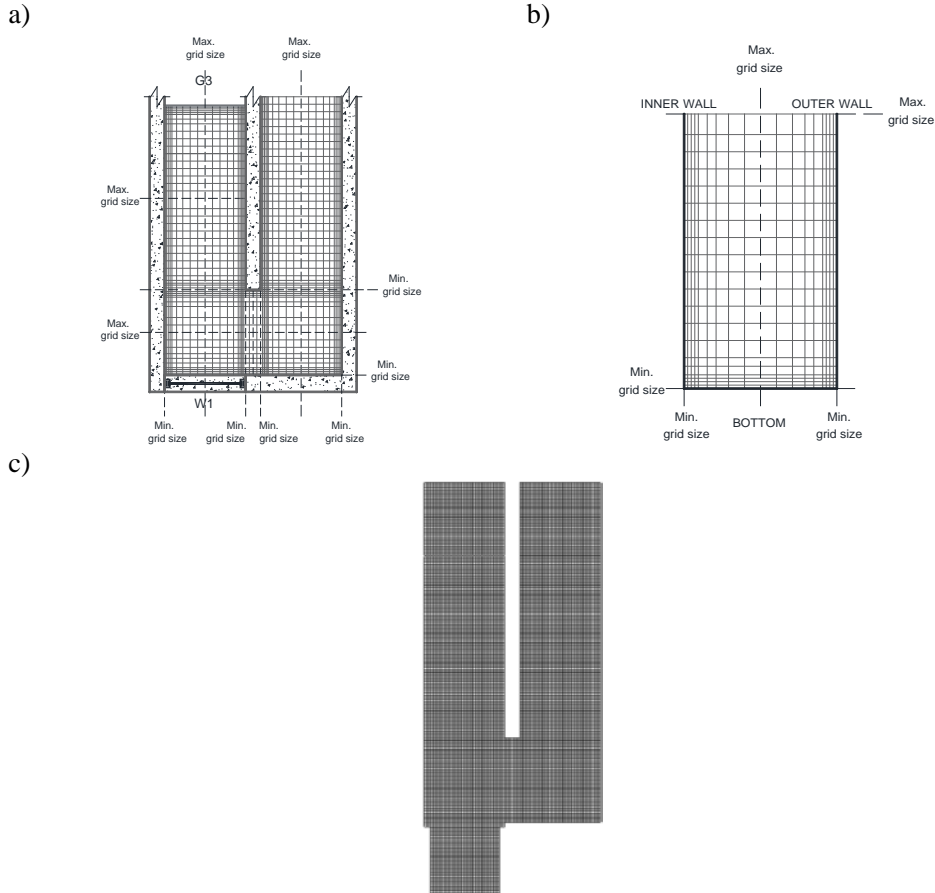
Figure 3.25. Grid domain configuration, a) plan view - detail b) cross-section profile and c) Grid configuration - plan view

The results of three turbulence models; i.e. $k - \varepsilon$, $k - \omega$, and $k - \varepsilon \ (RNG)$, in relation to water depth at the locations 3 and 10 (Figure 3.22-b) are compared against experimental data using the Relative Error criteria. These locations were chosen for the analysis because water level sensors (LS5 and LS6) where placed there. Based on the graphic representation, Figure 3.26 show a decreasing trend in Relative Error values of the turbulence models in relation to the decrease in max.value mesh sizes grid spacing. The analysis shows that the most accurate results are the $k - \varepsilon \ (RNG)$ model. This turbulence model provides an improved performance for flows with separation zones and around curved geometries [67]. Moreover, it is important to mention that, the numerical results underestimate the results in

relation to water-depth measurements. The subsequent analysis will be conducted with a maximum mesh size grid spacing of 1cm.

a)   b)
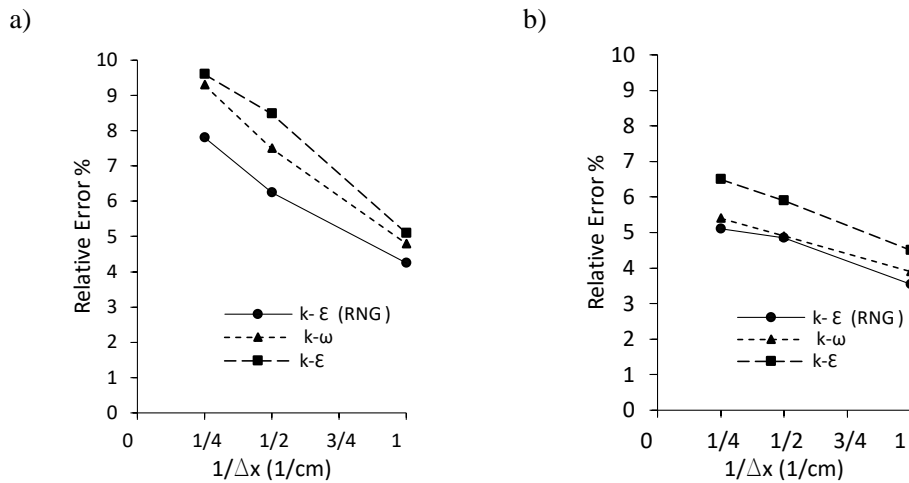
Figure 3.26. Mesh sensitivity analysis- Relative Error estimation - water depth, a) point 3 and b) point 10

Once the turbulence model and max mesh size grid spacing have been chosen, the effective roughness height (k_s) for the concrete surface is calibrated. Note that a wall-function boundary condition for the rough wall was established. Three k_s ; i.e., 0.002, 0.003, and 0.004, are analysed based on experimental values. The numerical results show better performance with $k_s = 0.003$ when the numerical values are compared against the experimental ones using the Relative Error criteria, Figure 3.27. It can be observed that the variation of the values of the roughness parameter does not have a significant discrepancy in relation to the experimental values.

a)   b)
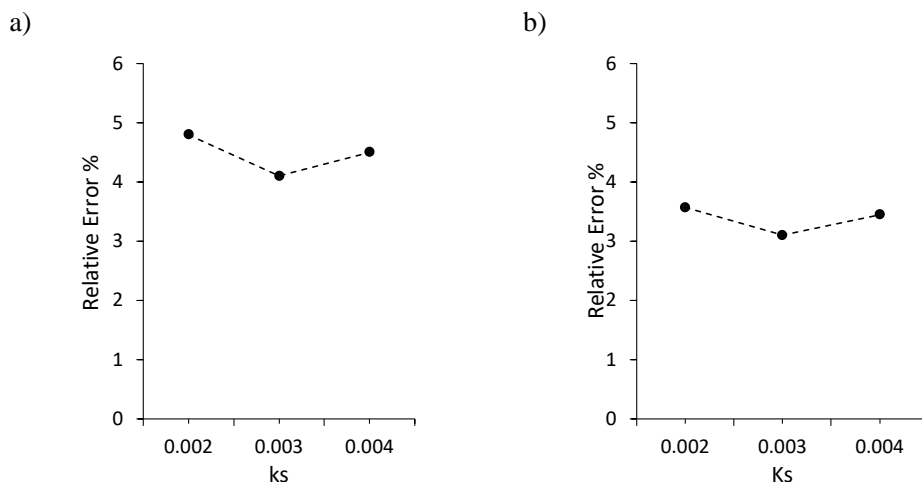
Figure 3.27. Effective roughness height analysis, a) Point 3, b) Point 10

To assess the accuracy of the numerical configuration, Relative Error criteria is used again to compare water-depth results against experimental data at the 10 locations within the domain. The distribution of the locations is shown in Figure 3.22-b and their values are in Table 3.5. Figure 3.28 shows that the maximum Relative Error produced is 4.01%.
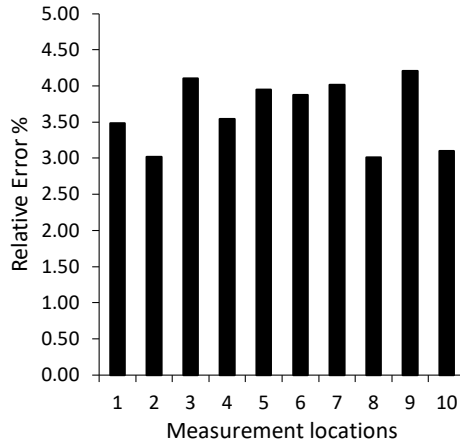
Figure 3.28. Water depth values - comparison

3.5.6 Numerical Simulation Schemes

The PIMPLE algorithm is used to solve the pressure-velocity coupling Navier-Stokes equations. A first-order Euler scheme is applied for the time derivative terms. The gradient terms are discretized with a second order central differential scheme and a linear interpolation scheme. The convection terms; i.e. mass and momentum equations are discretized using the second order upwind schemes, while in the volume of fraction term, α, a TVD-scheme with a van Leer limiter is used. The time step is updated to satisfice a Maximum Courant number condition of 0.5. This value provides numerical stability in the simulation process. The computational time for this analysis simulation is about 468 hours on an Intel core i7 6700k with 32 GB of RAM computer.

3.5.7 Convergence criteria

Residuals are used to monitor the convergence of simulations. The stability of the solution is assumed when the residual variables are less than 1×10^{-3} except for the pressure where the residual is less than 1×10^{-5}. The simulation was assumed to have reached a steady-state when the difference in discharges at the inlet and two outlets is less than 2.5%.

3.5.8 Results and discussion

For a proper analysis of the results, the channel bend has been divided into two parts, namely first sharp bend and second sharp bend. Vertical cross sections in the first sharp bend have

been established at 0º, 30º, 45º, 60º, and 90º; while in the second sharp bend have been established at 0º, 45º, and 90º (Figure 3.25)
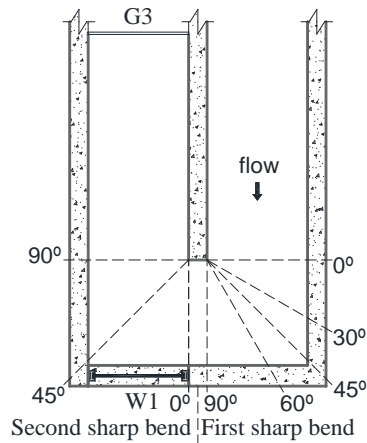
Figure 3.29. Cross section locations

Figure 3.30 shows the numerical results against the experimental case. Note that the free surface irregularities produce for the bend are captured for the numerical configuration (Figure 3.30-c).

a)   b)

c)

Figure 3.30. Open channel bend a) Numerical results b) PAC-UPC laboratory photo (taken by Gómez and Martínez-Gomariz [82]) and c) Free-surface numerical results

Streamlines

The secondary flow is an important feature of the flow pattern in open channel bends. In a channel bend, the water surface is slightly higher near the outer wall than near the inner wall causing a transverse pressure gradient, which provides the centripetal force for the fluid to change direction. This local imbalance between forces forms the secondary flow [66]. Figure 3.31 shows the secondary flows in two sections inside the first and second sharp bend. In order to clarify the numerical results presented by the CFD code, results in every cross section were digitalized.
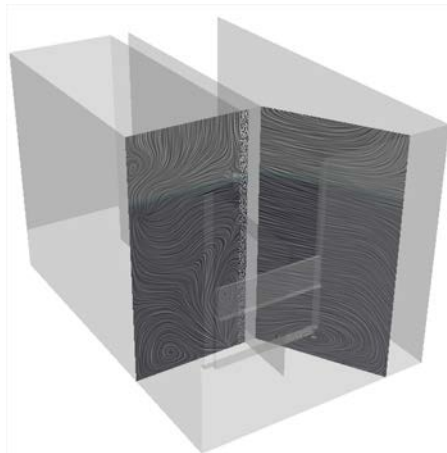
Figure 3.31. Sketch of secondary flows a) first sharp bend –section 60º, b) second sharp bend – section 90º

In Figure 3.32-a, the streamlines in the section located before the bend show a one-way radial flow towards the inner wall of the channel. From Figure 3.32-b to Figure 3.32-e, it is shown

the secondary flow moving along the bed. The rotation of the major secondary flow moves closer to the middle of the channel width and within 40 cm high. Figure 3.32-b shows how a minor secondary flow is formed near the outer wall and near the water surface. Therefore, the main secondary flow moves toward the inner wall while the minor secondary flow moves toward the outer wall. The rotation of this minor secondary flow is opposite to the major secondary flow. This feature has already been described by Gholami et al. [16]. Nevertheless, due to the influence of the first sharp bend this flow behavior vanishes, predominating thus flow towards the channel bottom in the outer wall (Figure 3.32-c). At the end of the first sharp bend (Figure 3.32-e) the flow points towards the outer wall of the channel.

a)
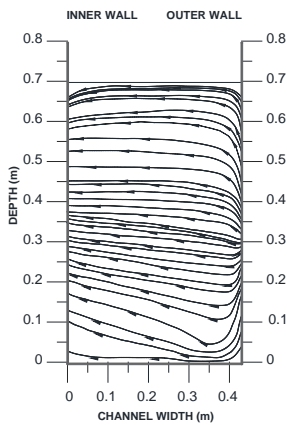
b)
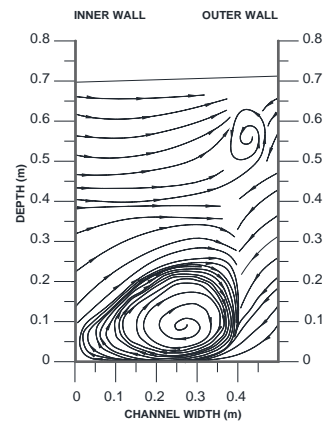
c)
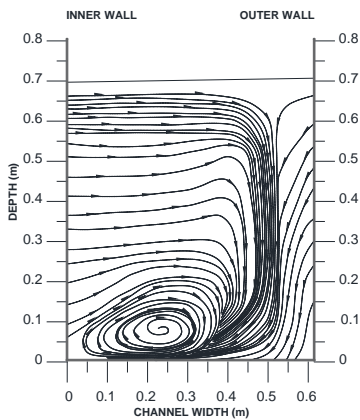
d)
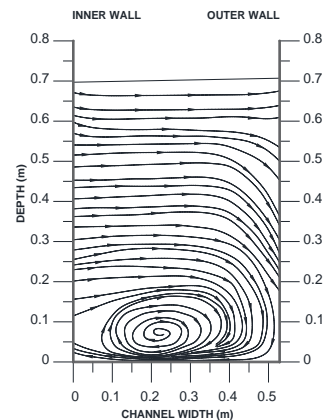
e)
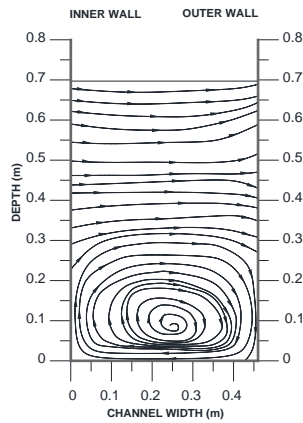
Figure 3.32. Streamlines at the established sections - first sharp bend a) 0º, b) 30º, c) 45º, d) 60º, and e) 90º

Figure 3.33 shows the streamlines at the different established sections along the second sharp bend, which is influenced by a weir and a gate. From Figure 3.33-a to Figure 3.33 -c, it is shown the formation of a minor secondary flow near the inner wall and within the 20-50 cm high of the channel. It is important to mention that, the rotation of the major secondary flow moves closer to the middle of the channel width and within 45 cm high (Figure 3.33-a to Figure 3.33-c). However, at the end of the second sharp bend, major secondary flow moves closer to the outer wall (Fig. 26-c).
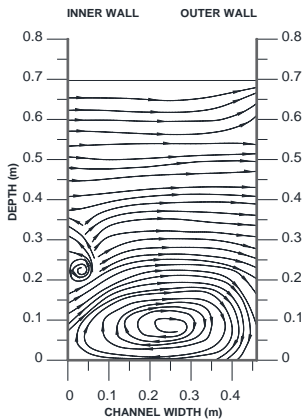
a)   b)
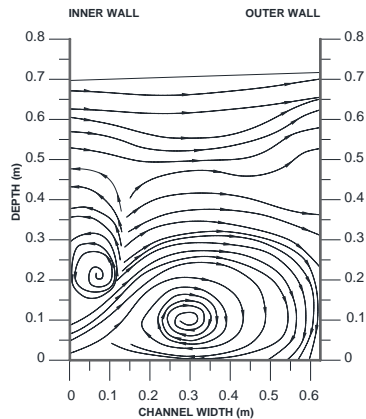
c)
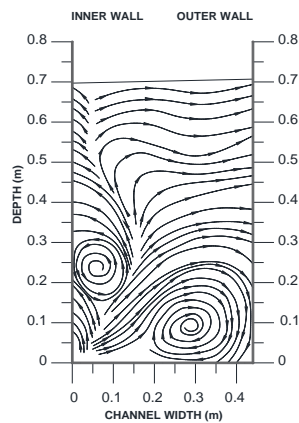
Figure 3.33. Streamlines at the established sections - second sharp bend a) 0º, b) 45º, and c) 90º

The comparison of streamlines along the bend at different horizontal plans is treated hereafter. Figure 3.34-a shows the pattern of the streamlines near the bed. Some of these streamlines deflect towards the inner wall following the pattern from upstream, but many of them coming from upper layers. At the mid-depth of flow, Figure 3.34-b, streamlines follow mostly the curvature of the bend; however, an area of a weaker counterrotating flow is identified (dead zone). The presence of the gate causes that streamlines collision with it and deflect towards the inner wall. Again, an area of flow moving slowly and distinct from the main flow structure is identified. In Figure 3.34-c, water surface can be observed, due to the presence of the weir (outlet 1) part of the streamlines following this direction while the rest of them deflect towards the outer wall of the channel until they hit the gate and deflect towards the inner wall. In the sharp corner, streamlines deflect towards the outer wall of the channel producing a dead zone larger than in mid-depth.
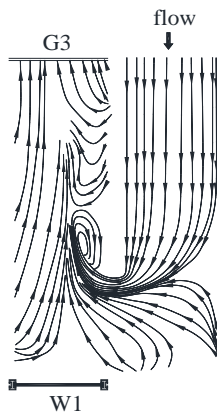
a)   b)
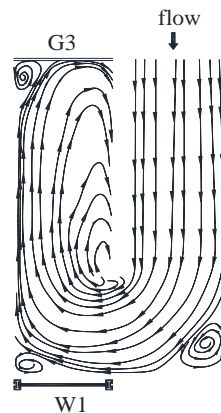
c)
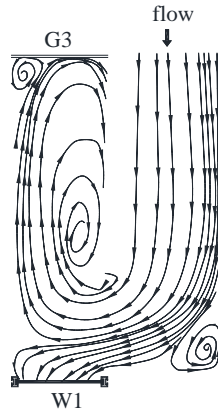
Figure 3.34. Streamlines at different distances from the bed, a) Near the bed, b) Mid-depth of flow and c) Water surface

After the gate, a submerged or drowned hydraulic jump is produced carrying a diffusive behavior of the streamlines. In Figure 3.35, show the streamlines in a section parallel to the wall in which the gate and the two outlets have influence (Figure 3.22-b, A-A section). Before the gate, the streamlines get close to each other and then after the gate the streamlines show a disturbed or oscillatory behavior of the flow. Figure 3.35-a shows the streamlines including both the water phase and the air phase, while Figure 3.35-b presents a digitalized streamlines of the water phase.

a)
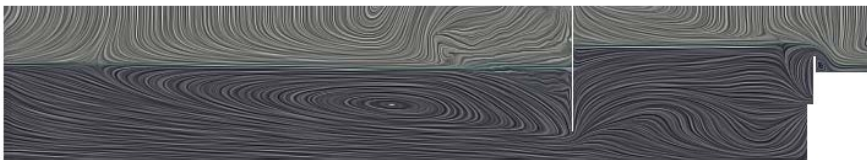
b)
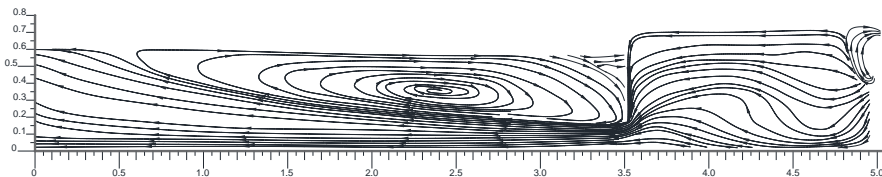
Figure 3.35. Streamlines in a section parallel to the wall - gate and the two outlets influence, a) water phase and the air phase b) water phase

Contours of longitudinal component of velocity

The distribution of the longitudinal component of velocity at established cross sections is presented in Figure 3.36. The high velocity zone tends to the inner wall through the first bend of the channel. From Figure 3.36-b to Figure 3.36-c, a zone with very low velocities ($\approx$ $0\ m/s$) is formed near the Outer Wall. An integration of the profiles show that about 15%

of the area through the investigated sections remains nearly static. At the end of the first sharp bend, the velocity distribution is almost symmetric Figure 3.36-e.

a)
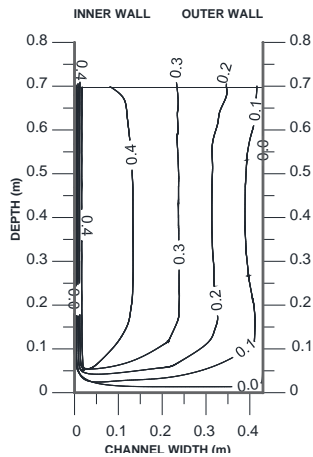
b)
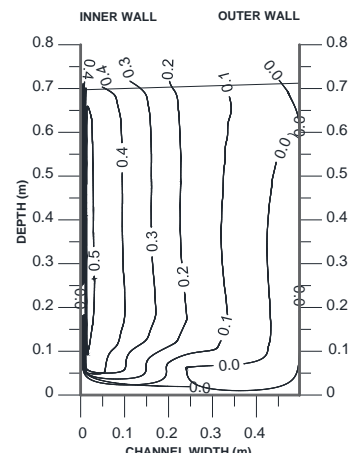
c)
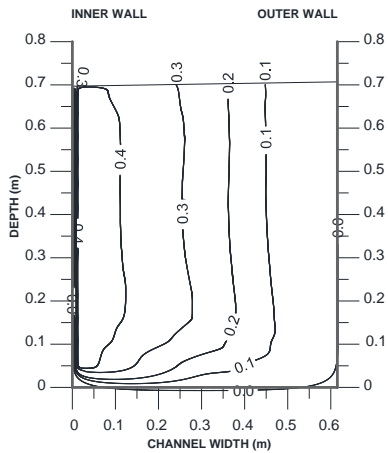
d)
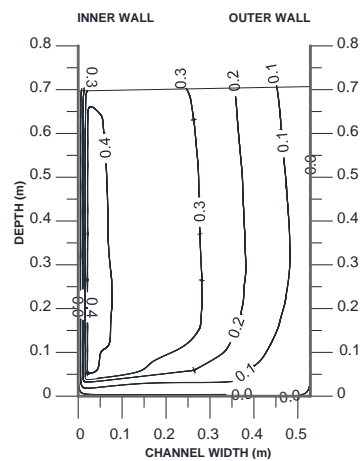
e)
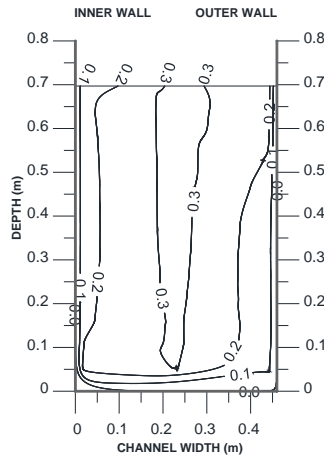
Figure 3.36. Contours of longitudinal component velocity (m/s) - first sharp bend, a) 0º, b) 30º, c) 45º, d) 60º, and e) 90º.

In the second sharp bend, weir and sluice gate influence leads to the formation of an unstructured component velocity distribution as can be seen in Figure 3.37. At the beginning, the weir (outlet 1) makes the velocity distribution asymmetric. At the end, the higher velocities are concentrated over the deeper Outer Wall of the section while velocities in the opposite direction appear on the top and bottom of the deeper Inner Wall. Unlike the first sharp bend, the high velocity zone tends to the outer wall.

a)
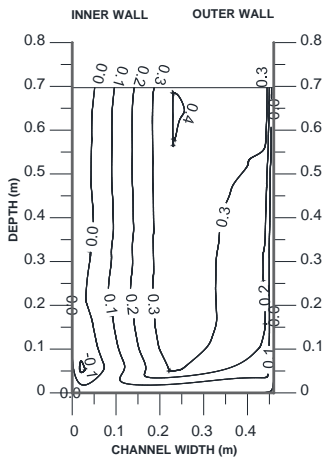
b)
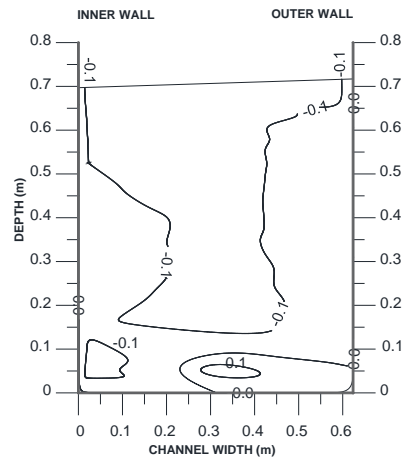
c)
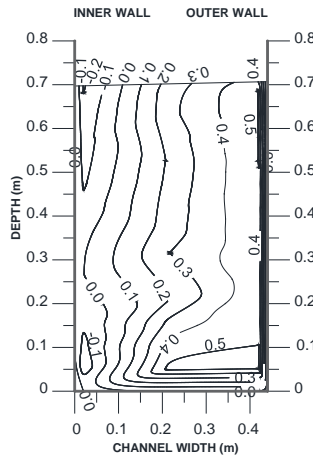
Figure 3.37. Contours of longitudinal component velocity (m/s) -second sharp bend a) 0º,
b) 45º, and c) 90º

3.5.9   Conclusions

In this test-case study, a numerical analysis of fluid field patterns in a sharp open channel bend is presented. A significant uniqueness of this study is influenced by a weir and a sluice gate. A mesh sensitivity analysis using RANS approach was conducted in order to determine an adequate mesh size which provides a balance between accuracy and computational time. In addition, the roughness parameter has been calibrated to set a reliable model. Once the turbulence model and the roughness parameter were established, the fluid field characteristics were analyzed. The main conclusions of this study are presented hereafter.

- Three-dimensional outcomes are in good agreement against experimental observations; i.e. water depths.

- $k - \varepsilon \, (RNG)$ turbulence model offers more accurate performances in front of the experimental measurements.

- In the first sharp bend, a main secondary flow forms along the bed moving toward the inner wall closer to the middle of the channel width and within 40 cm high. On the other hand, a minor secondary flow with opposite direction is formed near the outer wall and near the water surface.

- In the second sharp bend, which is influenced by a weir and a gate, a major secondary flow forms along the bed moving toward the outer wall closer to the middle of the channel width and within 45 cm high. In contrast, a minor secondary flow forms near the inner wall and within the 20-50 cm high of the channel along the bend.

- The pattern of the streamlines along the channel bend zone at different water levels differ from each other because the influence of the bend, the weir, and the gate. The

streamlines near the bed deflect towards the inner wall following the pattern from upstream, but many of them coming from upper layers. At the mid-depth of flow, the presence of the gate causes that streamlines collision with it and deflect towards the inner wall. On the water surface, due to the presence of the weir, part of the streamlines following this direction while the rest of them deflect towards the outer wall of the channel until they hit the gate and deflect towards the inner wall.

▪ In the first sharp bend, the high velocity zone tends to move towards the inner wall while in the second sharp bend the high velocity zone tends to move towards the outer wall.

The analysis shows a zone of low velocities in the Outer Wall of the first sharp bend causing a stagnation zone. It is suggested, to evaluate geometric modifications of the channel in the sharp bends parts.

3.6 References

[1]   B. Brørs, Numerical Modeling of Flow and Scour at Pipelines, J. Hydraul. Eng. 125 (1999) 511–523.

[2]   A. Roulund, B.M. Sumer, J. Fredsoe, J. Michelsen, Numerical and experimental investigation of flow and scour around a circular pile, J. Fluid Mech. 534 (2005) 351–401.

[3]   W. Wu, Computational river dynamics, Taylor & F, 2008.

[4]   A.M.A. Sattar, H. Jasak, V. Skuric, Three dimensional modeling of free surface flow and sediment transport with bed deformation using automatic mesh motion, Environ. Model. Softw. 97 (2017) 303–317.

[5]   J. Glimm, O. McBryan, R. Menikoff, D.H. Sharp, Front Tracking Applied to Rayleigh–Taylor Instability, SIAM J. Sci. Stat. Comput. 7 (1986) 230–251.

[6]   S.O. Unverdi, G. Tryggvason, A front-tracking method for viscous, incompressible, multi-fluid flows, J. Comput. Phys. 100 (1992) 25–37.

[7]   J. Farmer, L. Martinelli, A. Jameson, Fast multigrid method for solving incompressible hydrodynamic problems with free surfaces, AIAA J. 32 (1994) 1175–1182.

[8]   S. Osher, J.A. Sethian, Fronts propagating with curvature-dependent speed: Algorithms based on Hamilton-Jacobi formulations, J. Comput. Phys. 79 (1988) 12–49.

[9]   H. Rusche, Computational Fluid Dynamics of Dispersed Two-Phase Flows at High Phase Fractions, Direct. (2002).

[10]   A. Bayon-Barrachina, P.A. Lopez-Jimenez, Numerical analysis of hydraulic jumps using OpenFOAM, J. Hydroinformatics. 17 (2015) 662.

[11]   C.. W. Hirt, B.. D. Nichols, Volume of Fluid (VOF) Method for the Dynamics of Free Boundaries, J. Comput. Phys. 39(1) (1981) 201–225.

[12]   O. Ubbink, R.I. Issa, A Method for Capturing Sharp Fluid Interfaces on Arbitrary Meshes, J. Comput. Phys. 153 (1999) 26–50.

[13]   R. Stoll, F. Porte-Agel, Dynamic subgrid-scale models for momentum and scalar fluxes in large-eddy simulations of neutrally stratified atmospheric boundary layers over heterogeneous terrain, Water Resour. Res. 42 (2006) 1–18.

[14]   L.A. Larocque, J. Imran, M.H. Chaudhry, 3D numerical simulation of partial breach dam-break flow using the LES and $k-\epsilon$ turbulence models, J. Hydraul. Res. 51 (2013) 145–157.

[15]   A.S. Ramamurthy, S.S. Han, P.M. Biron, Three-Dimensional Simulation Parameters for 90° Open Channel Bend Flows, J. Comput. Civ. Eng. 27 (2013) 282–291.

[16]   A. Gholami, A. Akbar Akhtari, Y. Minatour, H. Bonakdari, A.A. Javadi, Experimental and Numerical Study on Velocity Fields and Water Surface Profile in a Strongly-Curved 90° Open Channel Bend, Eng. Appl. Comput. Fluid Mech. 8 (2014) 447–461.

[17]   A. Bayon, D. Valero, R. García-Bartual, F.J. Vallés-Morán, P.A. López-Jiménez, Performance assessment of OpenFOAM and FLOW-3D in the numerical modeling of a low Reynolds number hydraulic jump, Environ. Model. Softw. 80 (2016) 322–335.

[18]   Y. Kim, Z. Zhou, T.-J. Hsu, J.A. Puleo, Large eddy simulation of dam-break-driven swash on a rough-planar beach, J. Geophys. Res. Ocean. 122 (2017) 1274–1296.

[19]   R.J. McSherry, K. V. Chua, T. Stoesser, Large eddy simulation of free-surface flows, J. Hydrodyn. Ser. B. 29 (2017) 1–12.

[20]   Z. Xie, B. Lin, R.A. Falconer, Turbulence characteristics in free-surface flow over two-dimensional dunes, J. Hydro-Environment Res. 8 (2014) 200–209.

[21]   R.F. Dressler, Hydraulic Resistance Effect Upon the Dam-Break Functions*, J. Res. Natl. Bur. Stand. (1934). 49 (1952).

[22]   G.B. Whitham, The Effects of Hydraulic Resistance in the Dam-Break Problem, Proc. R. Soc. A Math. Phys. Eng. Sci. 227 (1955) 399–407.

[23]   R.F. Dressler, Unsteady Non-Linear Waves in Sloping Channels, Proc. R. Soc. A Math. Phys. Eng. Sci. 247 (1958) 186–198.

[24]   B. Hunt, Asymptotic Solution for Dam-Break Problem, J. Hydraul. Div. 108 (1982) 115–126.

[25]   B. Hunt, Perturbation Solution for Dam-Break Floods, J. Hydraul. Eng. 110 (1984) 1058–1071.

[26]   H. Chanson, Application of the method of characteristics to the dam break wave problem, J. Hydraul. Res. 47 (2009) 41–49.

[27]   N.D. Katopodes, T. Strelkoff, Computing Two-Dimensional Dam-Break Flood Waves, J. Hydraul. Div. 104 (1978) 1269–1288.

[28]   A.A. Akanbi, N.D. Katopodes, Model for Flood Propagation on Initially Dry Land, J. Hydraul. Eng. 114 (1988) 689–706.

[29]   F. Alcrudo, P. Garcia-Navarro, A high-resolution Godunov-type scheme in finite volumes for the 2D shallow-water equations, Int. J. Numer. Methods Fluids. 16 (1993) 489–505.

[30]   M.M. Alam, M.A. Bhuiyan, Collocation Finite-Element Simulation of Dam-Break Flows, J. Hydraul. Eng. 121 (1995) 118–128.

[31]   A.K. Jha, J. Akiyama, M. Ura, First- and Second-Order Flux Difference Splitting Schemes for Dam-Break Problem, J. Hydraul. Eng. 121 (1995) 877–884.

[32]   S.F. Bradford, B.F. Sanders, Performance of High-Resolution, Nonlevel Bed, Shallow-Water Models, J. Eng. Mech. 131 (2005) 1073–1081.

[33]   P. Garcia-Navarro, A. Fras, I. Villanueva, Dam-break flow simulation: some results for one-dimensional models of real cases, J. Hydrol. 216 (1999) 227–247.

[34]   L. Fraccarollo, E.F. Toro, Experimental and numerical assessment of the shallow water model for two-dimensional dam-break type problems, J. Hydraul. Res. 33 (1995) 843–864.

[35]   P. Brufau, P. Garcia-Navarro, Two-dimensional dam break flow simulation, Int. J. Numer. Meth. Fluids. 33 (2000) 35–57.

[36]   F. Aureli, P. Mignosa, M. Tomirotti, Numerical simulation and experimental verification of Dam-Break flows with shocks, J. Hydraul. Res. 38 (2000) 197–206.

[37]   A.K. Jha, J. Akiyama, M. Ura, Flux-Difference Splitting Schemes for 2D Flood Flows, J. Hydraul. Eng. 126 (2000) 33–42.

[38]   F. Aureli, A. Maranzoni, P. Mignosa, C. Ziveri, Dam-Break Flows: Acquisition of Experimental Data through an Imaging Technique and 2D Numerical Modeling, J. Hydraul. Eng. 134 (2008) 1089–1101.

[39]   M. Shige-eda, J. Akiyama, Numerical and Experimental Study on Two-Dimensional Flood Flows with and without Structures, J. Hydraul. Eng. 129 (2003) 817–821.

[40]   V.I. Bukreev, V. V. Zykov, Bore impact on a vertical plate, J. Appl. Mech. Tech. Phys. 49 (2008) 926–933.

[41]   S. Soares-Frazão, Y. Zech, Experimental study of dam-break flow against an isolated obstacle, J. Hydraul. Res. 45 (2007) 27–36.

[42]   C. Biscarini, S. Di Francesco, P. Manciola, CFD modelling approach for dam break flow studies, Hydrol. Earth Syst. Sci. 14 (2010) 705–718.

[43]   F. Aureli, S. Dazzi, A. Maranzoni, P. Mignosa, R. Vacondio, Experimental and numerical evaluation of the force due to the impact of a dam-break wave on a structure, Adv. Water Resour. 76 (2015) 29–42.

[44]   T. Shigematsu, P.L.-F. Liu, K. Oda, Numerical modeling of the initial stages of dam-break waves, J. Hydraul. Res. 42 (2004) 183–195.

[45]   K. Abdolmaleki, K.P. Thiagarajan, M.T. Morris-Thomas, Simulation of The Dam Break Problem and Impact Flows Using a Navier-Stokes Solver, (2004).

[46]   H. Ozmen-Cagatay, S. Kocaman, Dam-break flows during initial stage using SWE and RANS approaches, J. Hydraul. Res. 48 (2010) 603–611.

[47]   H. Ozmen-Cagatay, S. Kocaman, Dam-Break Flow in the Presence of Obstacle: Experiment and CFD Simulation, Eng. Appl. Comput. Fluid Mech. 5 (2011) 541–552.

[48]   K.M.T. Kleefsman, G. Fekken, A.E.P. Veldman, B. Iwanowski, B. Buchner, A Volume-of-Fluid based simulation method for wave impact problems, J. Comput. Phys. 206 (2005) 363–393.

[49]   E. Sánchez-Cordero, M. Gómez, E. Bladé, Three-dimensional numerical analysis of a dam-break using OpenFOAM, Proc. ISP RAS. 29 (2017) 311–320.

[50]   E. Sánchez-Cordero, J. Boix, M. Gómez, E. Bladé, 3D numerical analysis of a dam - break using VOF method and LES turbulence model, Ing. Del Agua. 22 (2018) 167–176.

[51]   S.S. Han, P.M. Biron, A.S. Ramamurthy, Three-dimensional modelling of flow in sharp open-channel bends with vanes, J. Hydraul. Res. 49 (2011) 64–72.

[52]   I. Rozovskiĭ, Flow of water in bends of open channels., Acad. Sci. Ukr. SSR, Kiev,

USSR (Translated by Isr. Progr. Sci. Transl. Jerusalem, 1961). (1957).

[53]   M. Naji Abhari, M. Ghodsian, M. Vaghefi, N. Panahpur, Experimental and numerical simulation of flow in a 90° bend, Flow Meas. Instrum. 21(3) (2010) 292–298.

[54]   J. Ye, J.A. McCorquodale, Simulation of Curved Open Channel Flows by 3D Hydrodynamic Model, J. Hydraul. Eng. 124 (1998) 687–698.

[55]   H. Morvan, G. Pender, N.G. Wright, D.A. Ervine, Three-Dimensional Hydrodynamics of Meandering Compound Channels, J. Hydraul. Eng. 128 (2002) 674–682.

[56]   W.Z. Lu, W.S. Zhang, C.Z. Cui, A.Y.T. Leung, A numerical analysis of free-surface flow in curved open channel with velocity-pressure-free-surface correction, Comput. Mech. 33 (2004) 215–224.

[57]   N. Rüther, N. Reidar, B. Olsen, M. Asce, Three-Dimensional Modeling of Sediment Transport in a Narrow 90° Channel Bend, J. Hydraul. Eng. 131 (2005) 917–920.

[58]   T. Bodnár, J. Příhoda, Numerical simulation of turbulent free-surface flow in curved channel, Flow, Turbul. Combust. 76 (2006) 429–442.

[59]   A. Khosronejad, C.D. Rennie, S.A.A. Salehi Neyshabouri, R.D. Townsend, 3D Numerical Modeling of Flow and Sediment Transport in Laboratory Channel Bends, J. Hydraul. Eng. 133 (2007) 1123–1134.

[60]   R. Booij, Measurements and large eddy simulations of the flows in some curved flumes, J. Turbul. 4 (2003).

[61]   W. Van Balen, W.S.J. Uijttewaal, K. Blanckaert, Large-eddy simulation of a mildly curved open-channel flow, J. Fluid Mech. 630 (2009) 413.

[62]   T. Stoesser, N. Ruether, N.R.B. Olsen, Calculation of primary and secondary flow and boundary shear stresses in a meandering channel, Adv. Water Resour. 33 (2010) 158–170.

[63]   W. Ottevanger, K. Blanckaert, W.S.J. Uijttewaal, A parameter study on bank shear stresses in curved open channel flow by means of large-eddy simulation, in: Proc. 7th IAHR Symp. River, Costal Estuar. Morphodynamics, Tsinghua Univesity, 2011: pp. 1917–1927.

[64]   S. Kang, F. Sotiropoulos, Flow phenomena and mechanisms in a field-scale experimental meandering channel with a pool-riffle sequence: Insights gained via numerical simulation, J. Geophys. Res. 116 (2011) F03011.

[65]   W. van Balen, K. Blanckaert, W.S.J. Uijttewaal, Analysis of the role of turbulence in curved open-channel flow at different water depths by means of experiments, LES and RANS, J. Turbul. 11 (2010) 1–34.

[66]   K. Blanckaert, H.J. De Vried, Secondary flow in sharp open-channel bends, J. Fluid Mech. 498 (2004) 353–380.

[67]   D. Choudhury, Introduction to the renormalization group method and turbulence modeling, Tech. Memo. No. 107, Fluent, Lebanon, NH. (1993).

[68]   S.B. Pope, Turbulent Flows, 2000.

[69]   X. Liu, M.H. García, Three-Dimensional Numerical Model with Free Water Surface and Mesh Deformation for Local Sediment Scour, J. Waterw. Port, Coastal, Ocean Eng. 134 (2008) 203–217.

[70]   S.. Han, Characteristics of flow around 90º open channel bends. PhD thesis., Concordia University, Montreal, Quebec., 2010.

[71]   V. Casulli, E. Cattani, Stability, accuracy and efficiency of a semi-implicit method for three-dimensional shallow water flow, Comput. Math. with Appl. 27 (1994) 99–112.

[72]   H.C. Lien, T.Y. Hsieh, J.C. Yang, K.C. Yeh, Bend-Flow Simulation Using 2D Depth-Averaged Model, J. Hydraul. Eng. 125 (1999) 1097–1108.

[73]   A.T. Ippen, P.A. Drinker, Boundary Shear Stresses in Curved Trapezoidal Channels, J. Hydraul. Div. 88 (1962) 143–180.

[74]   A. Shukry, Flow Around Bends in an Open Flume, Trans. Am. Soc. Civ. Eng. - ASCE. 115 (1949) 751–779.

[75]   H.J. de Vriend, A Mathematical Model Of Steady Flow In Curved Shallow Channels, J. Hydraul. Res. 15 (1977) 37–54.

[76]   J.P.T. Kalkwijk, H.J. de Vriend, Computational of the flow in shallow river bends, J. Hydraul. Res. 18 (1980) 327–342.

[77]   H.J. de Vriend, Velocity redistribution in curved rectangular channels, J. Fluid Mech. 107 (1981) 423–439.

[78]   Y. Shimizu, H. Yamaguchi, T. Itakura, Three- Dimensional Computation of Flow and Bed Deformation, J. Hydraul. Eng. 116 (1990) 1090–1108.

[79]   Y. Shimizu, T. Itakura, Calculation of Bed Variation in Alluvial Channels, J. Hydraul. Eng. 115 (1989) 367–384.

[80]   C.A.M.E. Wilson, J.B. Boxall, I. Guymer, N.R.B. Olsen, Validation of a Three-Dimensional Numerical Code in the Simulation of Pseudo-Natural Meandering Flows, J. Hydraul. Eng. 129 (2003) 758–768.

[81]   W. Wu, W. Rodi, T. Wenka, 3D Numerical Modeling of Flow and Sediment Transport in Open Channels, J. Hydraul. Eng. 126 (2000) 4–15.

[82]   M. Gómez, E. Martínez-Gomariz, 1D, 2D, and 3D Modeling of a PAC-UPC Laboratory Canal Bend, in: SimHydro 2014:Modelling of Rapid Transitory Flows, Sophia Antipolis, 2014: pp. 423–438.

[83]   K. Horváth, Model Predictive Control of Resonance Sensitive Irrigation Canals - PhD Thesis, Universitat Politècnica de Catalunya, 2013.

4   SEDIMENT TRANSPORT

4.1   Introduction

Sediment transport process is used to determine the morphological evolution, erosion or deposition, in open channels and rivers. The understanding of this process is essential in the context of river engineering practice to planning, analysis, protection, and remediation of river crossing structures (Figure 4.1). Accurate numerical model prediction is not a simple task because the flow field is often highly three-dimensional and turbulent. In addition, the sediment phenomena includes a wide range of grain sizes and different sediment material properties. Due to advances in computational power in recent years, the use of 3D numerical models has become a valuable tool for understanding and predicting morphodynamic developments.

This chapter begins with an overview of the sediment transport mechanisms in order to understand the erosion/deposition process. It continues with a review of the main studies conducted, which are based on the two main three-dimensional approaches, i.e. single-phase and two-phase. Then, the mathematical description of the governing differential equations for both model approaches are exposed. The chapter ends with an application of the two-phase modeling approach. The numerical results are compared with an experimental case used to simulate the scour caused by a submerged jet.

a)   b)

c)

Figure 4.1. Scour hole around bridge piers: a) cylindrical (www.usgs.gov) and b) rectangular cylinder (www.fondriest.com); c) Bridge failure due to pier scour (www.iahrmedialibrary.net)

4.2   Sediment Transport Mechanism

Sediments can be classified into two main categories according to the size of the particles that are composed, i.e. cohesive and non-cohesive. This study focuses on non-cohesive sediments, specifically sand. Mathematically it is useful to describe sand particles as a sphere with an equivalent grain diameter in order to specify the mechanical properties of the material.

In Sediment Transport, the concentration is an important parameter that controls the transport mechanism; thus, the sediment volume concentration can be defined as:

$$\phi = \frac{V_P}{V_P + V_f} \qquad (4.1)$$

where V_P and V_f are the volumes occupied by the particles and interstitial fluid, respectively. Similarly, the sediment mass concentration, c, can be obtained multiplying by the sediment density, ρ^s, so $c = \phi\rho^s$.

There is an important parameter in sediment concentration for uniform spheres that needs to be defined, i.e. random-packing. This parameter establishes the random arrangement of the spheres (volume is taken by a number of particles) poured in a given space of volume. Experiments show that there is a range of random-packing densities; i.e. the upper limit referred as random-close-packing and the lower limit denominated random- loose-packing [1].

In the classical sediment transport theory, single-phase, the transport modes are divided into bed-load and suspended-load. In the bed-load the particles roll, slide or saltate, with permanent or intermittent contact on the sediment bed; while, in the suspended-load, the flow turbulence transports the sediment particles into the water column [2].

On the other hand, a modern description of the non-cohesive sediment transport considers four transport layers according to the dominant transport mechanisms[‡], Figure 4.2. Therefore, Highly concentrated region of transport occurs immediately above the bed, *enduring contact regime*. The transport in this region is dominated by intergranular interactions due to enduring contact forces and it is a critical mechanism for sediment transport suspension since the flow turbulence is very small (viscous sublayer). In the region denominated *rapid sediment flow*, due to smaller concentration, the transport is dominated by particle-particle interactions (either due to enduring contact or energetic collision) and turbulence suspension (flow turbulence is important in this region). In the *dilute region*, particles are far from each other and the collisions are negligible. Then, the flow turbulence becomes the only dominant suspension mechanism.
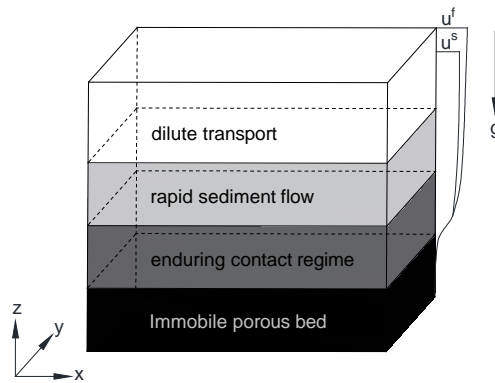
Figure 4.2. Schematic plot of different mechanisms in sediment transport
"Adapted from Cheng and Hsu [3]"

4.3   Models of sediment transport and bed elevation – An overview

The sediment transport models are divided into two main categories, single-phase and two-phase model approaches. In the single-phase model, the total sediment transport is separated into bed load and suspended load components. The bed load is parameterized with empirical or semi-empirical formulations, which are obtained from different laboratories, usually for a limited range of conditions in a steady flow experiment condition (i.e. Meyer-Peter and Muller [4]; Einstein [5]; Bagnold [6]; Yalin [7]; Wilson [8]; Ashida and Michiue [9]; Engelund and Fredsoe [10];Fernandez Luque and Van Beek [11]; Parker [12]; Smart [13]). On the other hand, the suspended load is resolved to treat the sediment as a passive scalar with a falling velocity difference with the flow phase. In practice, this approach can be applied to dilute sediment concentration so ignoring the effects of fluid-particle and particle-particle iterations. Changes in bed levels are calculated from sediment mass conservation equation, which provides a dynamic link between the two components using empirical or

---

[‡] Lecture notes - Professor Tian-Jian Hsu (University of Delaware - Center for Applied Coastal Research)

semi-empirical parameterization again to represent deposition and erosion fluxes (i.e. Smith and McLean [14]; van Rijn [15]; Garcia and Parker [16]; Zyserman and Fredsøe [17]).

Most single-phase models discretize and solve the Reynolds-Averaged Navier-Stokes equations (RANS), along with the sediment mass balance equation using a finite difference, finite element, or finite volume method suitable for structured or unstructured grids.

Numerical models to predict morphodynamic changes in the bed of open channels using $k - \varepsilon$ or $k - \omega$ turbulence closure have been reported [18–20]; while one others use the hydrostatic-pressure distribution over water depth assumption [21,22]. Also, several models to simulate local scour around structures have been developed [23–28]. Liu and García [29] proposed a numerical model in which the free surface flow is simulated with the volume of fluid scheme (VOF) and the bed change is captured with a moving mesh method based on a Lagrangian approach. More recently, Sattar et al.[30] presented a 3D numerical model using a novel volume of flow and a novel finite area methods in order to capture the water-air and water-sediment interface, respectively.

Despite the ability to predict long-term bed morphological evolution in rivers with this modeling approach; it is necessary to study a numerical alternative that can resolve the full profile of sediment transport. Depending on the flow condition, Chauchat et al. [31] state that the sediment concentration near bed-region can reach values ~60%, where the single-phase model relies on empirical or semi-empirical parameterization ignoring particle-particle and particle-fluid interactions [31,32].

The second alternative is the two-phase model approach, where the governing equations for both the particle motion and flow phase are formulated separately. The interaction between two phases is accounted by using the stress tensor due to phase interactions and the interfacial momentum transfer.

In the past decades, several models have been developed in the two-phase framework. Numerical models using Eulerian-Lagrangian scheme were proposed by [33,34]. Alternatively, some models are solved using Euralian-Euralian approach. Early models use the mixing length closure turbulence model [35–39], while more sophisticated models include two equations closure turbulence models, $k - \varepsilon$ or $k - \omega$ [40–46]. Recently, Lee et al.[47] and Cheng et al. [48] developed a multi-dimensional two-phase flow models using the kinetic theory and granular rheology theory for particle stress, respectively. Chauchat et al. [31] based on the Cheng et al.[48] model, added a dense granular flow rheology for the particle phase-stress.

4.4 Sediment transport models

4.4.1 Single-phase sediment transport model

The mathematical description presented in this section is based on the single-phase approach, classical model. As already mentioned, in this model, the total sediment transport is separated into suspended load and bed load components and a set of equations are defined to describe the bed evolution, i.e. erosion and deposition. A complete description of the model can be found in the publication presented by Liu and García [29].

Flow governing equations

The governing equations for the flow are the Reynolds-averaged Navier-Stokes (RANS) equations with $k - \varepsilon$ turbulence closure model and the free surface is tracked using the Volume of Fluid method (VOF).

Bed load transport

The displacement of the particles with permanent or intermittent contact on the sediment bed occurs when the threshold of sediment motion is exceeded [2]. The initiation of the sediment motion can be quantified by the non-dimensionalized bed shear stress called Shield number.

The bed load transport rates in different directions (fluxes), q_{bi}, are giving by [24]

$$q_{bi} = q_o \frac{\tau_{bi}}{|\tau_b|} - C|q_o| \frac{\partial \eta}{\partial x_i}, i = 1,2 \qquad (4.2)$$

in tensor form

$$q_{bi} = q_o \frac{\tau_{bi}}{|\tau_b|} - C|q_o| \cdot \nabla_s \eta \qquad (4.3)$$

where q_o is the bed load sediment transport rate per unit width for a flat bed, τ_b is the bed shear stress calculated from the flow model, C is a constant that reflects the slope of the sediment flux gradient $(1.5 - 2.3)$, and η is the bed elevation.

The bed load sediment transport rate formula, Equation (4.4), proposed by Fredsoe [49] is considered in this model

$$q_o = \begin{cases} 18.74\sqrt{Rgd}d(\theta - \theta_c)\left[\theta^{1/2} - 0.7\theta_c^{1/2}\right] & \text{if } \theta > \theta_c \\ 0 & \text{otherwise} \end{cases} \qquad (4.4)$$

where R is the relative submerged density given by

$$R = \frac{\rho_s}{\rho_w} - 1 \qquad (4.5)$$

here ρ_s is the density of sediment and ρ_w is the density of water

The dimensionless bed shear stress or Shield number, θ, is defined as:

$$\theta = \frac{\tau_b}{\rho_w g R d} \qquad\qquad (4.6)$$

d denotes a characteristic grand size of the bed material (i.e. d_{50}), and g is gravitational acceleration.

The critical Shield number for initiation of motion at the horizontal bed, θ_{co} , which is obtained from the Shields diagram, is adjusted to account the local slope effect according to the Equation (4.7), proposed by Roulund [26]. Thus, the critical Shields number is related to the bed slope angle, β; and the angle between the fluid velocity vector at the particle position and the steepest bed slope direction, φ, Figure 4.3; while μ_s is the static friction coefficient which value is 0.63 in this study.

$$\theta_c = \theta_{co}\left(\cos\beta\sqrt{1 - \frac{\sin^2\varphi\,\tan^2\beta}{\mu_s^2}} - \frac{\cos\varphi\,\sin\beta}{\mu_s}\right) \qquad (4.7)$$

In Equation (4.7), the critical Shields number increases or decreases when the wall shear stress tries to move sediment upslope or downslope, respectively [29].
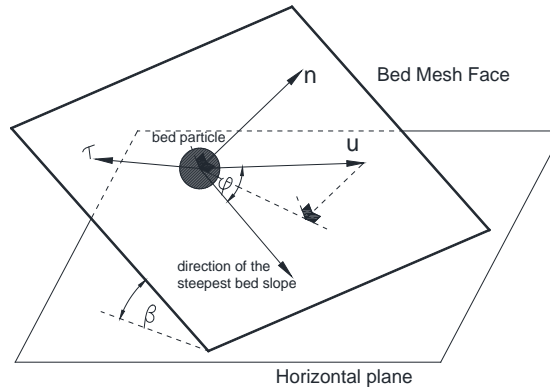
Figure 4.3. Slope effect on sediment transport - a single moving particle.
"Adapted from Roulund [26]"

Suspended Load

The suspended material process is modeled by solving a passive scalar convection-diffusion transport equation with an additional fall-velocity convection term. In this approach, the sediment concentration is diluted and the inertial effect of the particle is ignored (particle size is fine enough) [29].

$$\frac{\partial c}{\partial t} + \nabla \cdot \left(\mathbf{u} - w_s \delta_{j3}\right)c = \nabla \cdot \left(\frac{\nu_t}{\sigma_c}\nabla c\right) \qquad (4.8)$$

here c is the local volumetric suspended sediment concentration; $\mathbf{u}$ is the fluid velocity vector; w_s is the sediment fall velocity and δ is the Kronecker delta with $j = 3$ indicating the

vertical direction $(g/|g|)$; σ_c is the turbulent Schmidt number and ν_t is the diffusivity which is taken as the same value as turbulence eddy viscosity.

Bed Change

The bed elevation changes in vertical direction can be calculated by solving the Exner equation for sediment continuity.

$$\frac{\partial \eta}{\partial t} = \frac{1}{1-n}\left[-\frac{\partial q_i}{\partial x_i} + D - E\right], i = 1,2 \tag{4.9}$$

In tensor form

$$\frac{\partial \eta}{\partial t} = \frac{1}{1-n}[-\nabla \cdot q_{bi} + D - E] \tag{4.10}$$

the bed porosity n is on the first right-hand side factor of the equation. D is the rate at which sediment volume is deposited from suspended sediment at the bed, and E is the rate of entrainment or erosion of bed material into suspension.

The deposition rate, D, in the downward direction is the sediment concentration very near the bed, c_b, times the local sediment velocity, w_s. c_b is computed from the concentration at the nearest cell center above the bed.

$$D = c_b w_s \tag{4.11}$$

Oppositely, the entrainment rate, E, in the upward direction is considered as:

$$E = c_b{}^* w_s \tag{4.12}$$

here, it is necessary to introduce an empirical model to obtain $c_b{}^*$, which is the equilibrium concentration at a reference level very near the bed, z_b. In this model, $c_b{}^*$ is calculated using the formulation proposed by van Rijn [15].

$$c_b{}^* = 0.015\frac{d_{50}\psi^{1.5}}{z_b D_*^{0.3}} \tag{4.13}$$

where ψ is a dimensionless shear stress parameter; D_* is the dimensionless particle diameter; and H is the water depth from the bed.

$$\psi = \frac{\theta - \theta_c}{\theta_c} \quad (4.14) \quad D_* = d_{50}\left[\frac{R-1}{g\mu^2}\right]^{1/3} \quad (4.15) \quad z_b = 0.05H \quad (4.16)$$

The Exner equation is solved on the 2D bottom boundary grid and the bed level change is calculated. Therefore, the results are mapped back onto the 3D flow mesh, and the 3D finite volume mesh is deformed to follow the new bed profile.

4.4.2 Multiphase Eulerian two-phase modeling of sediment transport

The mathematical description in this section is based on the numerical model developed at the University of Delaware, College of Engineering, Civil and Environmental Engineering, Center for Applied Coastal Research; under the research group lead by the Professor Tian-Jian Hsu. As part of the doctoral training, the author's thesis worked a period of time as Visiting Scholar in this Research Department. A complete description of the model and its implementation can be found in the different publications [31,48,50,51].

Cheng et al. [48] developed a multi-dimensional model for sediment transport based on the Eulerian two-phase mathematical formulation proposed by Hsu et al. [50]. The mathematical equations are derived by ensemble averaging over carried fluid and dispersed particles following the formulation proposed by Drew [52]. To avoid resolving all scales of turbulence (larger than grain scale), additional turbulence averaging (or filtering) is necessary. The resulting 3D governing equations for Eulerian turbulence-averaged two-phase flow can be considered as the counterpart of Reynolds-Averaged Navier-Stokes (RANS) for single-phase flow. Therefore, in this two-phase flow approach, it is necessary to use appropriate closure models for turbulence modulation, fluid-particle interactions, and particle-particle interactions. According to Cheng [48], the resulting model can resolve the full dynamics for sediment transport (concentration profile) from immobile bed to dilute region of transport away from the bed, see Figure 4.2.

Kim et al. [51] modified the former model introduced by Cheng et al. [48] in order to consider the effect of the free water surface. The details considered most relevant to the mathematical formulation are detailed hereafter.

Flow governing equations

The numerical model is able to solve the problem when three phases are involved (air, water , and sediment). The governing equations are based on Reynolds-averaged approach. Mathematical expressions of the continuity and momentum equations for the flow variables involved, ϕ, are presented without the over bar on the mean values for simplicity.

It is assumed that there is no mass transfer between the three phases. The mass conservation equations for the phases can be written as:

$$\frac{\partial \phi^a}{\partial t} + \frac{\partial \phi^a u_i^a}{\partial x_i} = 0 \qquad (4.17)$$

$$\frac{\partial \phi^w}{\partial t} + \frac{\partial \phi^w u_i^w}{\partial x_i} = 0 \qquad (4.18)$$

$$\frac{\partial \phi^s}{\partial t} + \frac{\partial \phi^s u_i^s}{\partial x_i} = 0 \qquad (4.19)$$

where ϕ is the volumetric concentration and u is the velocity for air (a), water (w) and sediment (s), respectively; while $i = 1,2,3$ represents the spanwise, streamwise and vertical components.

Mass conservation establishes that:

$$\phi^a + \phi^w + \phi^s = 1 \tag{4.20}$$

The free surface is tracked using the Volume of Fluid method (VOF). In the VOF method, the air and water are considered as immiscible fluids and can be combined as a fluid phase, $\phi^f = \phi^a + \phi^w$. The sediment phase under the free water surface can be modeled as a miscible phase of fluids using the two-phases model approach [31,48]. The momentum equations for fluid and particle phases are presented according to Kim et al. [51]

$$\frac{\partial \rho^f \phi^f u_i^f}{\partial t} + \frac{\partial \rho^f \phi^f u_i^f u_j^f}{\partial x_j}$$
$$= -\phi^f \frac{\partial p^f}{\partial x_i} + \rho^f \phi^f \mathrm{g}\delta_{i3} - \sigma_t \gamma \frac{\partial \phi^a}{\partial x_i} + \frac{\partial \tau_{ij}^f}{\partial x_j} + M_i^{fs} \tag{4.21}$$

$$\frac{\partial \rho^s \phi^s u_i^s}{\partial t} + \frac{\partial \rho^s \phi^s u_i^s u_j^s}{\partial x_j} = -\phi^s \frac{\partial p^f}{\partial x_i} - \frac{\partial p^s}{\partial x_i} + \rho^s \phi^s \mathrm{g}\delta_{i3} + \frac{\partial \tau_{ij}^s}{\partial x_j} + M_i^{sf} \tag{4.22}$$

where f and s are superscripts for fluid and sediment phases, respectively. ρ is the density, u is the velocity , g is the gravitational acceleration, δ is the Kronecker delta with $i = 3$ indicating the vertical direction $(\mathrm{g}/|\mathrm{g}|)$, p is the pressure, σ_t is the surface tension, and γ is the surface curvature. The fluid stress, τ_{ij}^f, includes fluid grain-scale (viscous) stress and fluid Reynolds stress, which are calculated with a turbulence model based on two-equation turbulence approach. p^s, τ_{ij}^s, are particle pressure and particle shear stress. The latter terms are modeled on the basis of intergranular interactions; therefore, the kinetic theory of granular flow for particle collisions is applied at low to moderate sediment concentration, while a phenomenological closure of frictional contact stresses is used in concentrated regions. M_i^{fs} and M_i^{sf} represent the interphase momentum transfer between fluid and particle phases, and $M_i^{fs} = -M_i^{sf}$.

Closure models

Turbulence closures

The fluid stress term, τ_{ij}^f, is modeled based on $k - \varepsilon$ two-phases turbulence model proposed by Cheng et al. [48]. An adjustment to the former model is introduced by Kim et al. [51] in the turbulence kinetic energy, k^f, to consider the excessive diffusion in the water-air interface by means of the sharp density gradient.

The fluid stress term involves the effect of turbulent fluctuations larger than grain-scale into R_{ij}^{ft} (Reynolds stress), and a grain-scale components into r_{ij}^{ft}. Although r_{ij}^{ft} includes viscous stress and the effect due to fluid-particle interaction, this later effect is not considered in this model approach.

$$\tau_{ij}^f = R_{ij}^{ft} + r_{ij}^{ft} = \rho^f \phi^f \left[2(v^{ft} + v^f) S_{ij}^f - \frac{2}{3} k^f \delta_{ij} \right] \tag{4.23}$$

with v^{ft} being the turbulent eddy viscosity and v^f is the kinetic viscosity of the fluid. The deviatoric part of the fluid-phase strain rate tensor,S_{ij}^f, is defined as:

$$S_{ij}^f = \frac{1}{2} \left(\frac{\partial u_i^f}{\partial x_j} + \frac{\partial u_i^f}{\partial x_i} \right) - \frac{1}{3} \frac{\partial u_k^f}{\partial x_k} \delta_{ij} \tag{4.24}$$

The modified turbulence kinetic energy, k^f, is calculated by its balance equation appropriate for sands particles in water.

$$\frac{\partial \rho^f k^f}{\partial t} + \frac{\partial \rho^f u_i^f k^f}{\partial x_j}$$
$$= R_{ij}^{ft} \frac{\partial u_i^f}{\partial x_j} + \frac{\partial}{\partial x_j} \left[\rho^f \left(v^f + \frac{v^{ft}}{\sigma_k} \right) \frac{\partial k^f}{\partial x_j} \right] - \rho^f \varepsilon^f \tag{4.25}$$
$$- \frac{2\beta(1-\alpha)\phi^s k^f}{\phi^f} - \frac{\rho^f v^{ft}}{\phi^f \sigma_c} \frac{\partial \phi^s}{\partial x_j} (s-1) g \delta_{j3}$$

where σ_c and $s = \rho^f/\rho^s$ are the Schmith number and the specific density of the sediment, respectively. $\alpha = e^{-B \cdot S_t}$ characterizes the level of correlation between the fluid and sediment velocity fluctuations by using the Stokes number $S_t = t_p/t_l$ [51], where $t_p = \rho^s/\phi^f$ is the particle response time and $t_l = k/(6\varepsilon)$ is the characteristic timescale of energetic eddies, and B is an empirical coefficient.

The dissipation rate ε is exposed in the Equation (4.26)

$$\frac{\partial \rho^f \varepsilon^f}{\partial t} + \frac{\partial \rho^f u_i^f \varepsilon^f}{\partial x_j}$$
$$= C_{1\varepsilon} R_{ij}^{ft} \frac{\varepsilon^f}{k^f} \frac{\partial u_i^f}{\partial x_j} + \frac{\partial}{\partial x_j} \left[\rho^f \left(v^f + \frac{v^{ft}}{\sigma_\varepsilon} \right) \frac{\partial \varepsilon^f}{\partial x_j} \right]$$
$$- C_{2\varepsilon} \rho^f \frac{\varepsilon^f}{k^f} \varepsilon^f - C_{3\varepsilon} \frac{\varepsilon^f}{k^f} \frac{2\beta(1-\alpha)\phi^s k^f}{\phi^f} \tag{4.26}$$
$$- C_{4\varepsilon} \frac{\varepsilon^f}{k^f} \frac{\rho^f v^{ft}}{\phi^f \sigma_c} \frac{\partial \phi^s}{\partial x_j} (s-1) g \delta_{j3}$$

Finally, the turbulence eddy viscosity is calculated as

$$v^{ft} = C_\mu \frac{(k^f)^2}{\varepsilon^f} \tag{4.27}$$

The model constants $C_{1\varepsilon}$, $C_{2\varepsilon}$, $C_{3\varepsilon}$, $C_{4\varepsilon}$, C_μ, and B are summarized in the Table 4.1. It is important to mention that, B is a parameter that needs to be calibrated.

Table 4.1. Constant coefficient values

C_μ	$C_{1\varepsilon}$	$C_{2\varepsilon}$	$C_{3\varepsilon}$	$C_{4\varepsilon}$	σ_c	σ_k	σ_ε	B
0.09	1.44	1.92	1.2	1	1	1	1.3	0.25

Particle stresses closures

Particle stresses are caused by intergranular iterations due to particle collisions and/or enduring contact/frictional forces among particles [51]. In this numerical model, particle pressure and particle stress are composed of a collisional component (super-script sc) and a frictional component (super-script sf).

$$p^s = p^{sc} + p^{sf} \tag{4.28}$$

$$\tau_{ij}{}^s = \tau_{ij}{}^{sc} + \tau_{ij}{}^{sf} \tag{4.29}$$

The collisional components (p^{sc} and $\tau_{ij}{}^{sc}$) are modeled based on the kinetic theory of granular flow for low to moderate sediment concentration. In the kinetic theory, intergranular interactions are dominated by particle-velocity fluctuations due to binary collisions and the strength is quantified using the concept of granular temperature, θ. The balance equation for granular temperature proposed by Ding and Gidaspow [53] is used

$$\frac{3}{2}\left[\frac{\partial \, \phi^s \rho^s \theta}{\partial t} + \frac{\partial \, \phi^s \rho^s u_j^s \theta}{\partial x_j}\right] = \left(-p^{sc}\delta_{ij} + \tau_{ij}{}^{sc}\right)\frac{\partial u_i^s}{\partial x_j} - \frac{\partial q_j}{\partial x_j} - \gamma_s + J_{int} \tag{4.30}$$

where q_j is the flux of granular temperature, γ_s is the energy dissipation rate due to inelastic collision, and J_{int} is the production (or dissipation) due to the interaction with the carrier fluid phase. The closure of particle pressure is used according to Ding and Gidaspow [53]:

$$p^{sc} = \rho^s \phi^s [1 + 2(1 + e)\phi^s g_{s0}]\theta \tag{4.31}$$

where e is the coefficient of restitution during collision. g_{s0} is the radial distribution function which describe the probability of the binary collisions as a function of particle concentration, which can be calculated as [54]:

$$g_{s0} = \frac{2 - \phi^s}{2(1 - \phi^s)^3} \tag{4.32}$$

The particle collision stress is considered as [55]

$$\tau_{ij}{}^{sc} = 2\mu^{sc} S_{ij}{}^{s} + \lambda \frac{\partial u_k^s}{\partial x_k} \delta_{ij} \tag{4.33}$$

where $S_{ij}{}^{s}$ is the deviatoric part of sediment-phase strain rate tensor:

$$S_{ij}{}^{s} = \frac{1}{2}\left(\frac{\partial u_i^s}{\partial x_j} + \frac{\partial u_j^s}{\partial x_i}\right) - \frac{1}{3}\frac{\partial u_k^s}{\partial x_k}\delta_{ij} \tag{4.34}$$

The particle shear viscosity, μ^{sc}, and the bulk viscosity, λ, are calculated as a function of granular temperature and radial distribution function by means of the kinetic theory.

$$\mu^{sc} = \rho^s d\sqrt{\theta}\left[\frac{4}{5}\frac{\phi^{s2}g_{s0}(1+e)}{\sqrt{\pi}} + \frac{\sqrt{\pi}\,g_{s0}(1+e)(3e-1)\phi^{s2}}{15(3-e)}\right. \\ \left. + \frac{\sqrt{\pi}\,\phi^s}{6(3-e)}\right] \tag{4.35}$$

$$\lambda = \frac{4}{3}\phi^{s2}\rho^s d g_{s0}(1+e)\sqrt{\frac{\theta}{\pi}} \tag{4.36}$$

A mathematical model analogous to the Fourier's law of conduction is assumed to the closure of granular temperature flux

$$q_j = -\kappa^{sc}\frac{\partial\theta}{\partial x_j} \tag{4.37}$$

where k^{sc} is the conductivity of granular temperature

$$\kappa^{sc} = \rho^s d\sqrt{\theta}\left[\frac{2\phi^{s2}g_{s0}(1+e)}{\sqrt{\pi}} + \frac{9\sqrt{\pi}\,g_{s0}(1+e)^2(2e-1)\phi^{s2} + 5\pi\phi^s}{2(49-33e)}\right] \tag{4.38}$$

The dissipation rate is calculated as:

$$\gamma_s = 3(1+e^2)\phi^{s2}\rho^s g_{s0}\theta\left[\frac{4}{d}\left(\frac{\theta}{\pi}\right)^{1/2} - \frac{\partial u_j^s}{\partial x_j}\right] \tag{4.39}$$

The carrier-flow turbulence can also induce particle fluctuations. The fluid-particle interaction can be expressed according to Hsu et al. [50]

$$J_{int} = \phi^s\beta(2\alpha k^f - 3\theta) \tag{4.40}$$

When the sediment concentration increases and reaches a certain value, ϕ_f^s, intermittent collisions decrease and the particles come into contact with each other. In this condition; the term of the particle pressure, p^{sf}, due to enduring contact and the term of the shear stress, $\tau_{ij}{}^{sf}$, caused by the frictional contact, are modeled by Cheng et al. [48] with a

phenomenological closure. Both terms are important to model the full transport profile to ensure the quasi-static bed without the need to track the location of the immobile bed.

The particle pressure because of enduring contact in the concentrated regions are modeled using the expression proposed by Johnson and Jackson [56]

$$
p^{sf} = \begin{cases} 0 & \phi^s < \phi^s_f \\ F \dfrac{\left(\phi^s - \phi^s_f\right)^a}{\left(\phi^s_{max} - \phi^s_f\right)^b} & \phi^s \geq \phi^s_f \end{cases}
\tag{4.41}
$$

where $\phi^s_f = 0.57$ is the random-loose-packing concentration and $\phi^s_{max} = 0.635$ is the random-close-packing for spheres used within the immobile porous bed. $F = 0.05$, $a = 3$, $b = 5$ are empirical coefficients which were calibrated by Cheng et al. [48].

The particle shear stress due to frictional contact is calculated:

$$
\tau_{ij}{}^{sf} = -2\mu^{sf} S_{ij}{}^s
\tag{4.42}
$$

Srivastava and Sundaresan [57] calculated μ^{sf} by combining p^{sf} and frictional viscosity from the model proposed by Schaefer [58]

$$
\mu^{sf} = \frac{\sqrt{2}\, p^{sf}\, \sin \theta_f}{2\sqrt{S_{ij}{}^s S_{ij}{}^s}}
\tag{4.43}
$$

where θ_f is a constant friction angle (repose angle).

Inter-phase momentum exchange

Due to in this mathematical formulation approach, the fluid (i.e. mixture of air and water) and sediment phases are considered as a continuum, the momentum exchange of these two phases are coupled by using Newton's third law, $M_i^{fs} = -M_i^{sf}$. In this interaction, only the dominant terms as drag force and turbulence suspension are considered (lift force, added mass force and Basset force are neglected) [48]

$$
M_i^{fs} = -M_i^{sf} = \phi^s \beta \left(u_i^f - u_i^s\right) + \beta \frac{\upsilon^{ft}}{\sigma_c} \frac{\partial \phi^s}{\partial x_i}
\tag{4.44}
$$

4.5 Three-dimensional numerical modeling of local sediment scour – A multi-dimensional two-phase flow approach

4.5.1 Introduction

Local scour of sediments can cause instability and failures in hydraulic structures (e.g. bridges piers, abutments, etc.). An estimated prediction of the location and maximum depth of scour is necessary for a safe engineering design. However, the scour process around hydraulic structures is complex due to three-dimensionality of the flow and sediment transport issue [59]. The development in computer capabilities in recent years provides an increasing possibility for solving sediment transport phenomena through the use of 3D numerical models.

Three-dimensional numerical models for local scour usually use the simplified concept that separates the total sediment transport into suspended and bed load components and a set of equations is used to describe the bed evolution process. Thus, several models have been developed by different investigators [28,60,61] to simulate the scour process.

Olsen and Melaaen [23] and Olsen and Kjellesvig [62] carried out the first three-dimensional numerical study of local scour around piles using RANS equations and $k - \varepsilon$ turbulence model. Brørs [24] and Roulund et al. [26] proposed a numerical models by using RANS equations with $k - \varepsilon$ and $k - \omega$ closure approaches, respectively. Those models assume a rigid lid for the free surface, so this assumption is likely to be valid when the curvature of the interface is smooth. As a result, the models are applicable only for small Froude numbers. Liu and García [29] developed a numerical model based on RANS equations with $k - \varepsilon$ closure model. They used the VOF method to track the free surface and a moving mesh deformation method for local sediment scour based on Laplacian smoothing operator. The numerical results for flow field and scour profile showed good agreement with experimental observations.

In order to improve some weaknesses in the previous model, Zhou [63] incorporated in the computational mesh motion, a sliding mechanism concept to restrict the bed slope angle to be smaller than the angle of repose. On the other hand, numerical improvements were implemented by Sattar et al. [30]. Wherein, the free surface is tracked with a steady-resistance VOF formulation, which alleviates instabilities and allows more efficient calculations; whereas, a finite element dynamic mesh method is used to simulate the deformation mesh.

In contrast, recently some studies have applied the two-phase flow approach to capturing the scour process. In two-phase models, the governing equations for both phases (flow and sediment) are formulated separately. The interaction between two phases is considered by including terms that define the interaction between phases, such as interphase momentum transfer and intergranular stresses.

Cheng et al.[48] and Chauchat et al.[31] presented a three-dimensional two-phase flow model for sediment transport applications where the free surface interface is not considered. These authors, validated the model using several tests; among them, the scour development downstream of an apron following the numerical studies of Amoudry and Liu [64]. They concluded that the numerical model shows a good capability to deal that type of test case.

In this study, the predictive ability of local scour process is analyzed using the new multi-dimensional two-phase flow approach in which three-phases, i.e. water, air, and sediment, are considered. To do so, the results of the new model are evaluated against the experimental data set of turbulent wall jet scour measured by Chatterjee et al. [65]. Although Lee et al. [66] presented an analysis using a three-phase approach; to the author's knowledge, it is the first time that this experiment configuration set-up using a multi-dimensional two-phase model based on kinetic theory is reported. In addition, a comparative analysis is performed between the results obtained with models based on, the classical sediment transport concept and the new approach.

4.5.2   Experimental set-up model

The verification test compares the solution of the numerical models with experimental data of turbulent submerged jet scour measured by Chatterjee et al. [65]. The experimental layout is shown schematically in Figure 4.4.
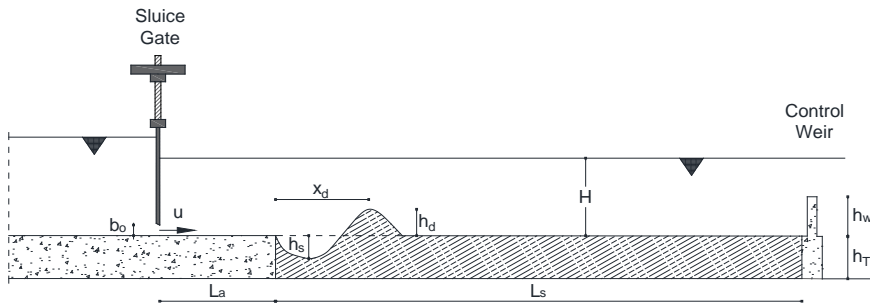
Figure 4.4. Schematic view of the turbulent wall jet scour experiment

The sluice gate opening allows the inflow discharge from the reservoir formed at the beginning of the experiment. This produces a horizontal water velocity, which forms a submerged jet due to the initial conditions downstream of the reservoir. The downstream initial condition has a constant water depth controlled by an outlet weir. Then, the water interacts with the apron until it reaches the erodible part of the experiment (sand), thus forming the local scour.

The relevant parameters of the test set-up are summarized in Table 4.2.

Table 4.2. Physical parameters for the numerical simulation

Ls	La	b_0	H	hw	h_T	**u**
m	m	cm	m	m	m	m/s
2.10	0.66	2.00	0.291	0.239	0.250	1.56

The bed material is quartz sand with $\rho_s = 2650$ kg/m^3 , $d_{50} = 0.76$ mm, angle of repose 29º and porosity 0.43.

4.5.3 Boundary and Initial conditions

In the computational domain, an equivalent boundary condition to simulate the reservoir is impose in the jet inlet BC in order to optimize the computational time. Additionally, a 2D consideration is used due to the flow streamwise direction is prevalent.

Figure 4.5 shows the sketch of the boundary conditions imposed in the experimental case set-up. In the wall-inlet, apron, sed-left, bottom and sed-right; a wall-function boundary condition for a rough wall is established. At the top of the test-case, an atmospheric boundary condition is imposed, $p_{\text{total}} = 0$. For the jet-inlet, a variation-time velocity function according to the given discharge-rate is applied; while in the outlet condition, a dynamic pressure, $p_{\text{dynamic}} = 1/2\,\rho\mathbf{u}^2$, with zero normal gradient, is used at the end of the channel where the hydrostatic pressure is subtracted from the total pressure. Details of this BC can be found in [29,30]. Note that the axis origin is at the end of the apron.
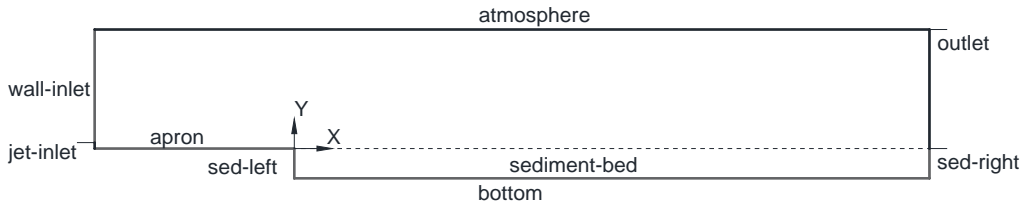
Figure 4.5. Description of the boundary conditions- An schematic view

In order to summarize the boundary conditions information, the following nomenclature is adopted. zG is zeroGradient for Neumann condition and fV is fixed value for Dirichlet condition. Furthermore; ϕ^f is the combined fluid phase (air and water), ϕ^s is the sediment phase, k and ε are the turbulence parameters, $\mathbf{u}^a$ and $\mathbf{u}^b$ are the fluid and sediment vector velocities, respectively; while θ is the granular temperature for the kinetic theory. So, mathematical boundary condition descriptions imposed in the domain are presented in the Table 4.3.

Table 4.3. Boundary conditions implemented in the test-case numerical simulation

Boundary	ϕ^f	ϕ^s	k	ε	$\mathbf{u}^a$	$\mathbf{u}^b$	p	θ
Wall-inlet	zG	zG	zG	zG	fV, $\mathbf{u}^a = 0$	fV, $u^b = 0$	zG	zG
Apron	zG	zG	zG	zG	fV, $\mathbf{u}^a = 0$	fV, $u^b = 0$	zG	zG
sed-left	zG	zG	zG	zG	fV, $\mathbf{u}^a = 0$	fV, $u^b = 0$	zG	zG
Bottom	zG	zG	zG	zG	fV, $\mathbf{u}^a = 0$	fV, $u^b = 0$	zG	zG
sed-right	zG	zG	zG	zG	fV, $\mathbf{u}^a = 0$	fV, $u^b = 0$	zG	zG
atmosphere	zG	zG	zG	zG	zG	zG	fV, $p_{\text{total}} = 0$	zG
jet-inlet	fV, $\phi^f = 1$	fV, $\phi^s = 0$	fV*, $k = 1 \times 10^{-12}$	zG	fV, $\mathbf{u}^a = f(Q)$	fV, $u^b = 0$	zG	fV, $\theta = 0$
outlet	fV, $\phi^f = 1$ if $y \le 0.291$ $\phi^f = 0$ if $y > 0.291$	zG	zG	zG	zG	zG	zG p_{dynamic} fV, $p_{\text{total}} = f(y)$	zG

* A value close to 0 is imposed, to provide numerical stability to the code.

The initial condition for the water depth is imposed to 0.291 m. Note that until now the height sediment-bed has not been defined. For this, the initial sediment concentration is specified using the mathematical formulation, Equation (4.45), proposed by Cheng et al. [67]

$$\phi(z) = 0.54 \frac{1 + \tanh[150(z_{b0} - z)]}{2} \qquad (4.45)$$

where z_{b0} is the height sediment-bed and z is the vertical direction in the domain. This formulation provides a smooth vertical sediment concentration profile which avoid numerical instability.

4.5.4   Grid domain configuration

Non-uniform structured elements are used in the grid configuration of the computational domain. The large gradients of flow expected; near walls, fluid-air, and fluid-sediment interface; impose mesh densification in their vicinity. Furthermore, in order to capture the jet effect and scour process with adequate detail, blocks with higher grid density are established. Due to the jet effect, horizontal velocity is larger than the vertical velocity, the grid size in the downstream water inlet direction is coarser than the vertical direction.

The domain is divided into nineteen grid blocks, see Figure 4.6; here maximum grid cells size are imposed in the bottom of the sediment bed, atmosphere and in the middle-height of the blocks VIII to XI. On the other hand, a minimum grid size are assigned in the top of the sediment bed, I to III blocks, and in the blocks XII to XV. These latter ones are configured to capture the free surface effect.
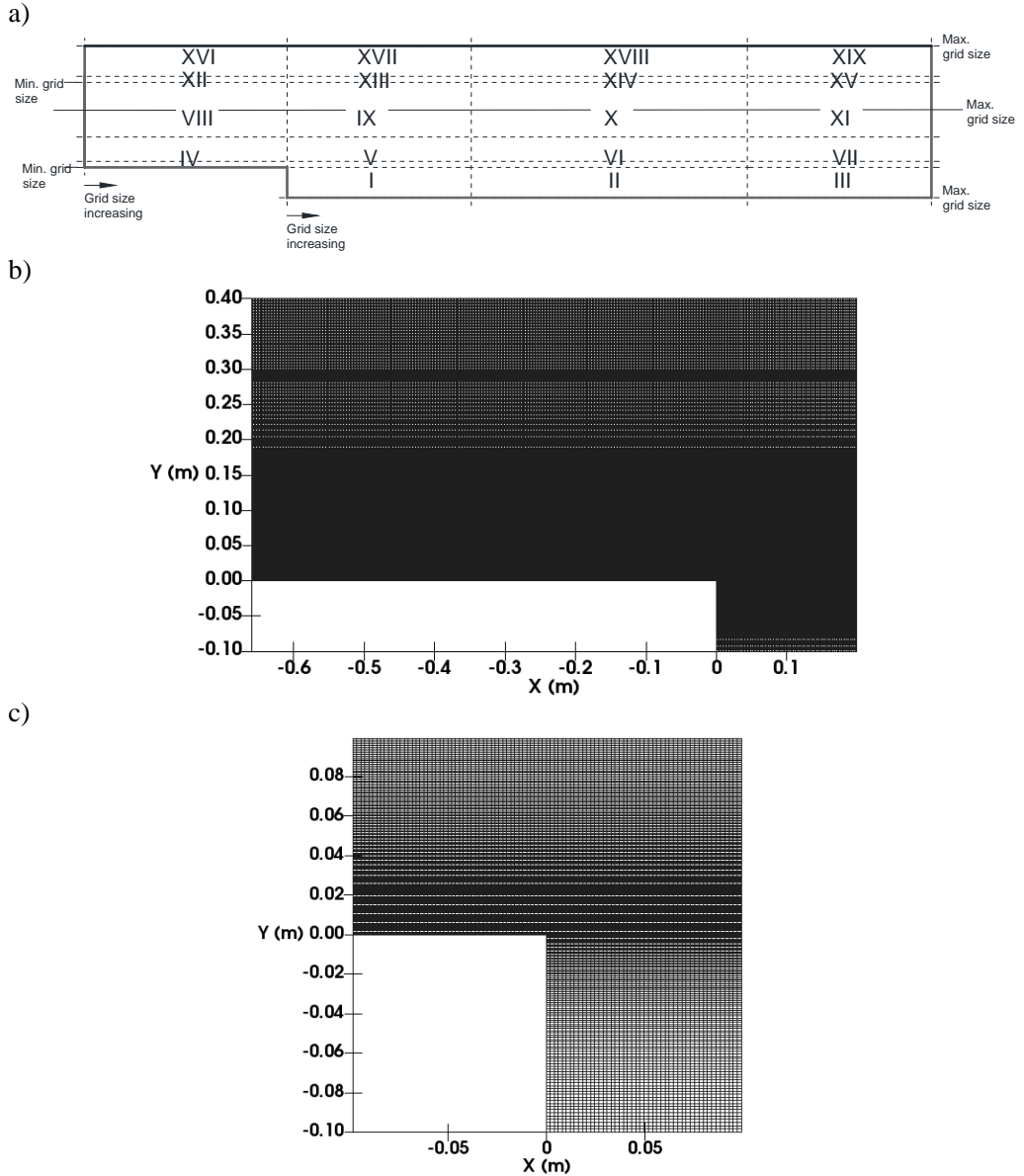
a)

b)

c)

Figure 4.6. a) A sketch of the numerical domain configuration, b) Grid configuration detail inlet-apron, c) Grid configuration detail apron-sediment

In order to obtain grid independent results, sensitive analysis was performed following the methodology proposed by Han [68]. Similar layouts with two maximum grid cell size values were tested. The values differ by 20% between them.

The final grid was chosen once the deviations, at t= 60 s, of velocities, pressure, depth scour and height sand dune were less than 5% compared with the penultimate grid.

In the streamwise direction, Δx, starting from the coarser grid at the jet-inlet and wall inlet boundary conditions, the cells size increase with a maximum aspect ratio of 1.5, $\Delta x \in [2 \times 10^{-3} - 3 \times 10^{-3}]$ m.

On the other hand, in the vertical direction, Δy, a maximum aspect ratio of 4 is imposed. A summary of the values are presented in Table 4.4.

Table 4.4. Summary of the grid size implemented – vertical direction

Blocks	Grid size Δy range values (min-max) m
I to III	$[5 \times 10^{-4} - 3 \times 10^{-3}]$
IV to VII	$[5 \times 10^{-4} - 5 \times 10^{-4}]$
VIII to XI	$[5 \times 10^{-4} - 2 \times 10^{-3}]$
XII to XV	$[4 \times 10^{-4} - 2 \times 10^{-3}]$
XVI to XIX	$[2 \times 10^{-3} - 2 \times 10^{-3}]$

4.5.5 Numerical Simulation Schemes

The pimple algorithm is used to solve the Navier-Stokes equations, velocity-pressure coupling procedure. The numerical discretization schemes for the differential operators are described in this section. As regards of temporal derivative, the implicit second-order backward scheme is applied. The convection terms in the momentum conservation equation, mass conservation equation and granular temperature equation are solved using the second-order central difference scheme bounded with a variation of the Sweby limiter [69], limitedLinear. On the other hand, for the volume fraction variable, α, a second-order Total Variation Diminish (TVD)-scheme with van Leer limiter is used. Due to the mesh-orthogonality, a second-order linear corrector scheme is used for the diffusion terms.

In addition, maximum Courant number was set to 0.2, which ensures convergence and numerical stability. Note that the Courant number is low, which causes an increase in the computational time required. The simulation with this numerical approach is extremely time-consuming. Therefore, the computational time is about 140 hours for 10 s of simulation on an Intel core i7 6700k with 32 GB of RAM computer.

4.5.6   Results and discussion

Scour profile

Scour profiles comparison between the numerical simulation data using two model approaches, i.e. single-phase and multi-dimensional two-phase flow, against experimental measurements are presented in Figure 4.7. The single-phase numerical data are obtained from the results presented by Liu and García [29]. Although the analysis of results are offered for 8 different instants of time, i.e. t= 1, 3, 5, 8, 12, 20, 30 and 60 min; the computational power and computational time required to perform the complete experiment, make that, only the first four instants are analyzed in this study.

The high velocity of the jet causes that, the shear stress on the erodible part of the experiment (sand), placed downstream of the rigid apron, exceed the critical shear stress value causing the development of the scour and a sediment deposition dune. According to the study conducted by Chatterjee, the scour development is highly dependent on time; which presents a rapid scour in the initial period of the experiment, gradually reduced until an equilibrium stage is reached.

The qualitative analysis shows an adequate agreement between both simulated values and experimental observations in the scour process for the four instants in mention. However, there are discrepancies in the shape and height value of the sediment deposition dune in the multiphase-model approach.
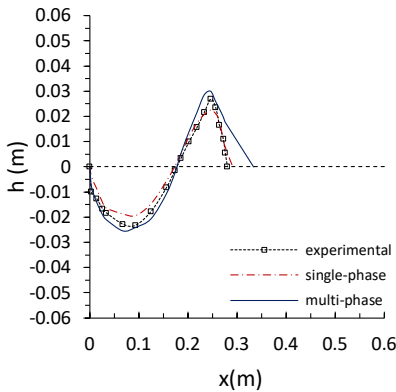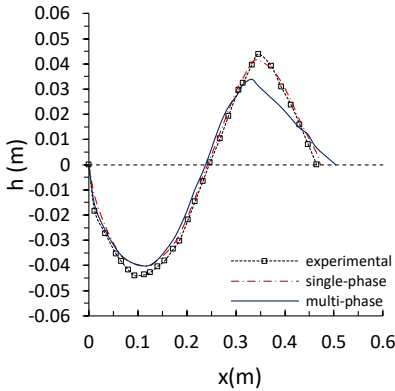
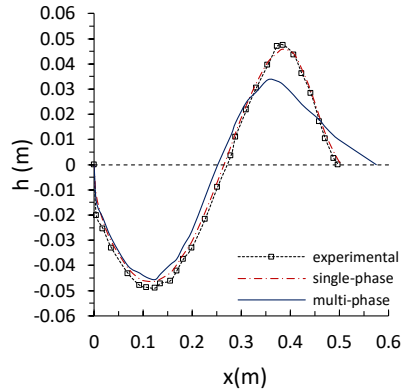a)   b)
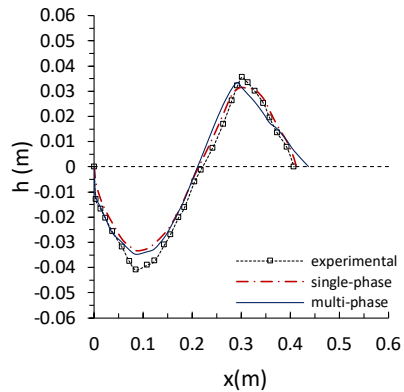
c)   d)

Figure 4.7. Scour profile development at time: a) 1 min, b) 3 min, c) 5 min and d) 8min.

The multiphase-model model over-predict the values during the first minute of the simulation while under-predict the values of the sediment deposition dune for the rest of the analysis when are compared with the experimental measurements. The under-prediction of values increase while the simulation progresses over time. In fact, the downstream measured slope is steeper than the computed slope, the above leads to the toe of the sediment sand dune varies from the experimental measurements.

It is worth mentioning that the experimental set-up reported by Chatterjee [65] does not detail the initial conditions. This can lead to discrepancies obtained during the first minute of analysis due to initial conditions imposed in the numerical configuration.

On the other hand, in the numerical configuration of this case, the B coefficient value recommended in Chauchat et al. [31] was imposed. Once in that study, the effect of the free surface is not considered and due to the modification in the $k - \varepsilon$ turbulence model, the B parameter should be calibrated again. In addition, it is important to emphasize that a 2D simplification has been considered, minimizing three dimensional effects produced in the laboratory experiment.

The results of the simulations for both approaches are listed in Table 4.5, where the coefficient of determination R^2 is used for their quantification. Both models agree well with experimental measurements. Note that the single-phase approach presents higher correlation values of R^2.

Table 4.5. Coefficient of determination R^2

t	R^2	
min	single-phase	multi-dimensional
1	0.987	0.949
3	0.994	0.985
5	0.998	0.984
8	0.997	0.967

Figure 4.8 shows the snapshots of sediment concentration profiles during the scour process at t=1, 3, 5 and 8 min.
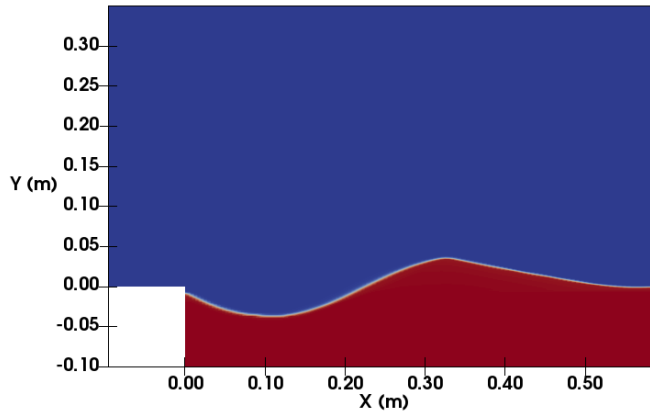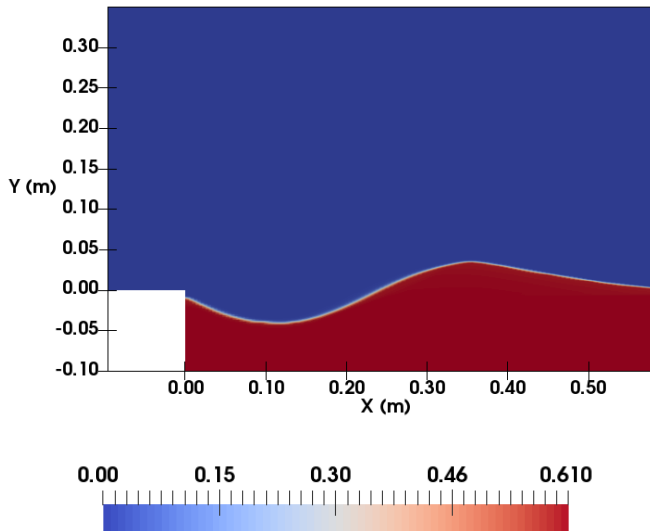
a)
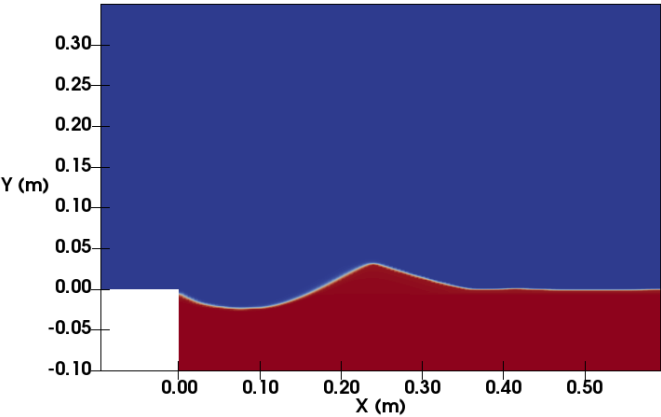
b)
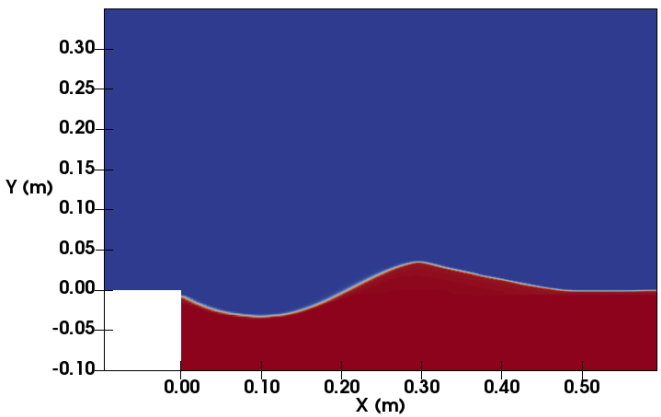
c)

d)

Figure 4.8. Sediment concentration profiles – scour process: a) 1 min, b) 3 min, c) 5 min and d) 8min (volume fraction indicator field).

In Figure 4.9, the simulated maximum depth of the scour hole, h_s, and the experimental data are presented (Refer to Figure 4.4). During the first minute of the experiment, the multi-phase model presents a higher scour depth, then the model matches with the simulated values of the single phase approach. It is important to mention that, except for the first minute, both models under-predict the experimental values for the period of analysis. The maximum discrepancy of the multi-phase model is in t=1 min, where the model under-predict the value, 5.3 mm. On the other hand, the single-phase over-predict the value, 5.2 mm t= 8min.
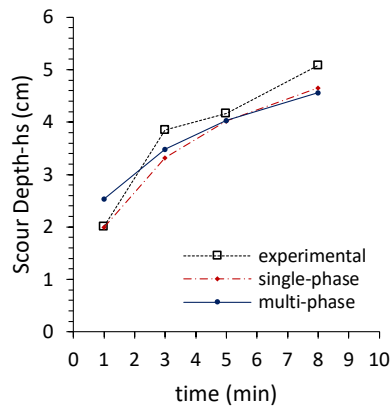
Figure 4.9. Maximum Scour depth - evolution with time

Figure 4.10-a and Figure 4.10-b show the results of the simulation in terms of height, h_d, and horizontal location, x_d, of the sediment deposition dune peak, respectively (Refer to Figure 4.4). The maximum discrepancy values are summarized in Table 4.6.

Table 4.6. Max. Discrepancy

Model	Max. discrepancy			
	time	h_d	time	x_d
	min	(mm)	min	(cm)
Multi-phase	8	12.79	8	2.84
Single-phase	5	5.7	3	0.21

a)
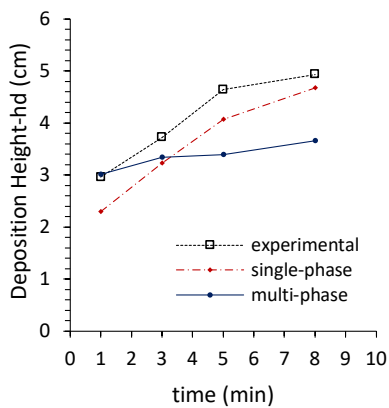
b)

Figure 4.10. Sediment deposition dune peak - evolution with time,
a) height and b) horizontal location

Fluid flow and sediment phase velocities

In Figure 4.12, the sediment-phase velocity fields are plotted. The interaction between the jet flow and the water-depth downstream initial condition produces a recirculation zone, over the apron, towards the water jet inlet, Figure 4.11-a, as well as an alteration in the water free surface is shown, Figure 4.11-b.
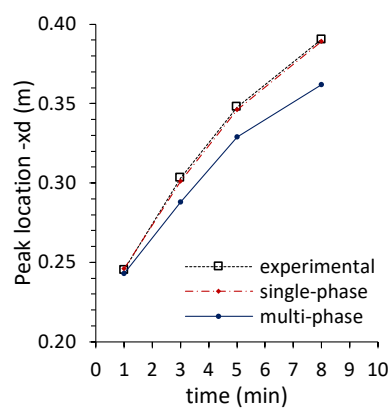
a)

b)
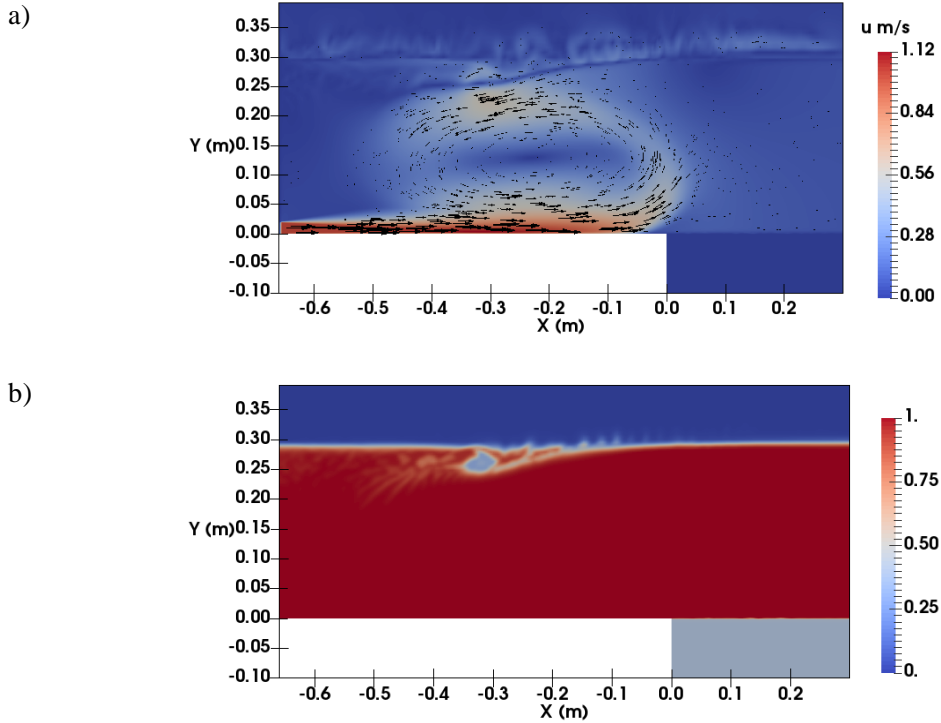
Figure 4.11. Apron zone before the jet reached the erodible part: a) velocity (m/s), b) water-surface profile (volume fraction indicator field)

In the scour hole, the sediment is transported along to the bed profile until it reaches the peak of the sediment deposition dune. It can be seen, the ability of the model to simulate both the bed-load and suspended-load transport. In the first instant of analysis, greater sediment dispersion occurs downstream. As the scour process takes place, the interaction is closest to sediment profile.

a)

b)

c)

d)
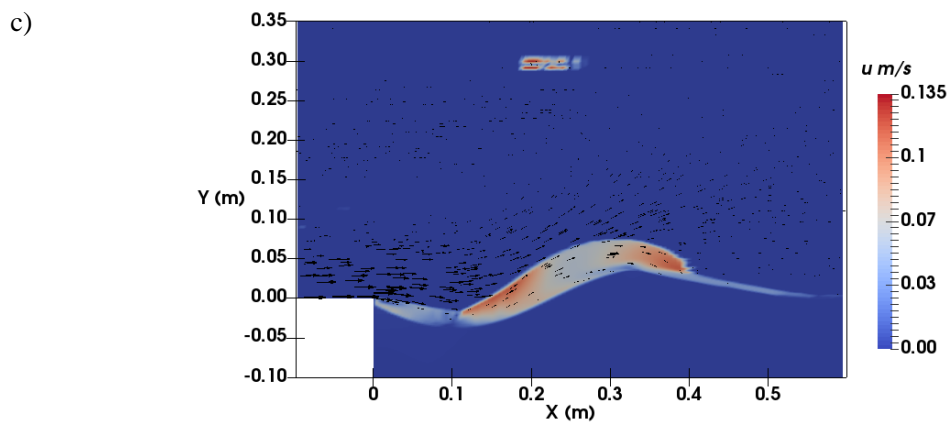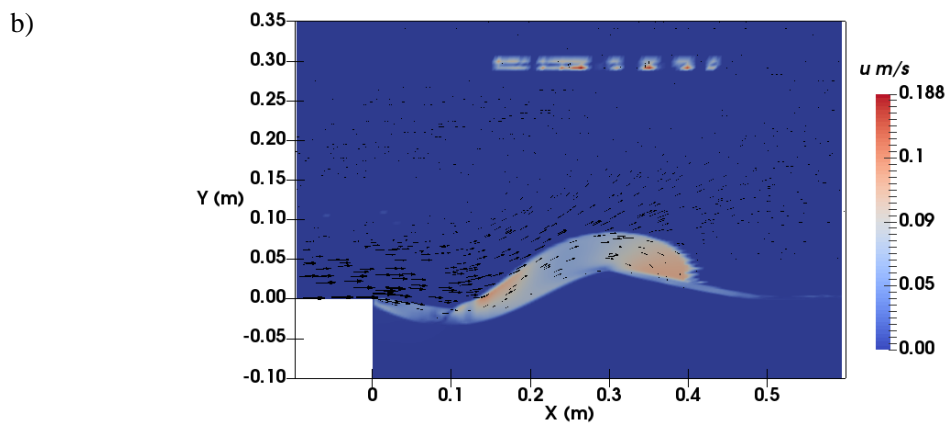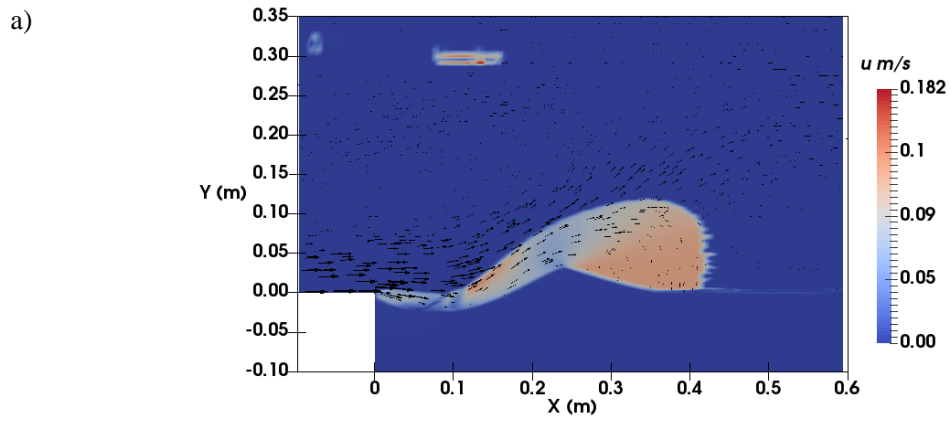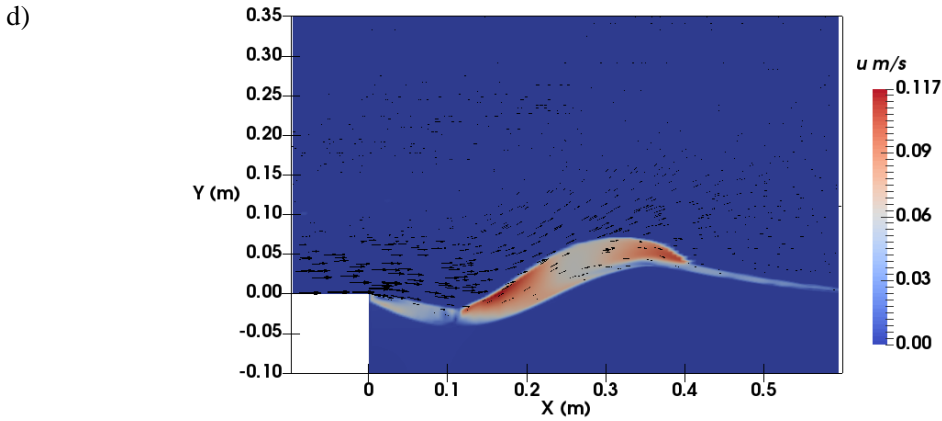
Figure 4.12. Sediment velocity profiles at time a) 1 min, b) 3 min, c) 5 min and d) 8min.

Note that the water velocity produces the drag of the sand particles at the peak of the sediment deposition dune. Then, the particles are deposited downstream due to the gravity force. This might explain the reduction in the peak value with respect to the measured value, as well as the downstream slope in the sediment deposition dune. It is important to mention that the B parameter allows characterizes the level of correlation between the particles and fluid fluctuating motions.

4.5.7 Conclusions

The predictive ability of the local scour process of sediments is analyzed by using the multi-dimensional two-phase flow modeling approach. The results obtained are compared with both, experimental laboratory values and single-phase modeled data. In order to obtain numerical results values which do not depend on the mesh size, a sensitivity analysis is performed. The main conclusions are described hereafter,

- The multi-dimensional two-phase numerical results match adequately against the experimental depth scour measurements.

- Differences between the multi-dimensional two-phase numerical results and experimental values are exposed when, both the peak-height and horizontal location of the sand deposition dune are considered.

- High correlation values are presented despite the above in the previous two items.

- A complete analysis of the sediment profile can be performed, due to the mathematical formulation involved in this mathematical approach.

Although the multi-phase sediment approach requires finer spatial resolution and smaller time steps than classical sediment transport models, the non-consideration of the mesh movement for the bed profile update provides numerical stability. It is important to mention that, due to the calibration parameter B was obtained without taking into account neither the

$k - \varepsilon$ turbulence model modification nor the free surface effect, a calibration process have to be performed in order to set a value that matches better with this test-case.

In addition, the completed test-case simulation have to be performed in order to analyze the scour-hole pattern when the equilibrium state is achieved.

4.6 References

[1] G.Y. Onoda, E.G. Liniger, Random loose packings of uniform spheres and the dilatancy onset, Phys. Rev. Lett. 64 (1990) 2727–2730.

[2] H.M. García, Sedimentation and erosion hydraulics, in: Hydraul. Des. Handb., McGraw-Hill, New York, 1999.

[3] Z. Cheng, T.-J. Hsu, A TURBULENCE-RESOLVING EULERIAN TWO-PHASE MODEL FOR SEDIMENT TRANSPORT, Coast. Eng. Proc. 1 (2014) 74.

[4] E. Meyer-Peter, R. Muller, Formulas for Bed Load Transport, Proc. 2nd Meet. Int. Assoc. Hydraul. Struct. Res. Delft, 7 June 1948. (1948) 39–64.

[5] H.A. Einstein, The Bedload Function for Bedload Transportation in Open Channel Flows, Tech. Bull. No. 1026, U.S.D.A., Soil Conserv. Serv. (1950).

[6] R.A. Bagnold, The Flow of Cohesionless Grains in Fluids, Philos. Trans. R. Soc. A Math. Phys. Eng. Sci. 249 (1956) 235–297.

[7] M.S. Yalin, An Expression for Bed-Load Transportation, J. Hydraul. Div. 89 (1963) 221–250.

[8] K.C. Wilson, Bed-Load Transport at High Shear Stress, J. Hydraul. Div. 92 (1966) 49–59.

[9] K. Ashida, M. Michiue, Study on Hydraulic Resistance and Bed-load Transport Rate in Alluvial Streams., Trans. Japan Soc. Civ. Eng. 206 (1972) 59–69.

[10] F. Engelund, J. Fredsoe, A Sediment Transport Model for Straight Alluvial Channels, Nord. Hydrol. 7 (1976) 293–306.

[11] R. Fernandez Luque, R. Van Beek, Erosion And Transport Of Bed-Load Sediment, J. Hydraul. Res. 14 (1976) 127–144.

[12] G. Parker, Self-formed straight rivers with equilibrium banks and mobile bed. Part 2. The gravel river, J. Fluid Mech. 89 (1978) 127.

[13] G.M. Smart, Sediment Transport Formula for Steep Channels, J. Hydraul. Eng. 110 (1984) 267–276.

[14] J.D. Smith, S.R. McLean, Spatially averaged flow over a wavy surface, J. Geophys. Res. 82 (1977) 1735–1746.

[15] L.C. van Rijn, Sediment Transport, Part II: Suspended Load Transport, J. Hydraul. Eng. 110 (1984) 1613–1641.

[16] M. Garcia, G. Parker, Entrainment of Bed Sediment into Suspension, J. Hydraul. Eng. 117 (1991) 414–435.

[17] J.A. Zyserman, J. Fredsøe, Data Analysis of Bed Concentration of Suspended Sediment, J. Hydraul. Eng. 120 (1994) 1021–1042.

[18] W. Wu, W. Rodi, T. Wenka, 3D Numerical Modeling of Flow and Sediment Transport in Open Channels, J. Hydraul. Eng. 126 (2000) 4–15.

[19] J. Zeng, S.G. Constantinescu, L. Weber, A fully 3D nonhydrostatic models for prediction of flow, sediment transport and bed morphology in open channels, XXXIst

Int. Assoc. Hydraul. Res. Congr. Seoul, Korea. a (2005) 554– 560.

[20]   N. Ruether, N.R.B. Olsen, 3D modeling of transient bed deformation in a sine-generated laboratory channel with two different width to depth ratios, Third Int. Conf. Fluv. Hydraul. River Flow 2006, Lisbon, Port. (2006).

[21]   S.Y. Wang, S.E. Adeff, Three-dimensional modeling of river sedimentation process., in: Proc., 3rd Int. Symp. River Sedimentation, Univ. Mississippi, Mississippi, 1986: pp. 1496–1505.

[22]   A. (Thanos) N. Papanicolaou, M. Elhakeem, G. Krallis, S. Prakash, J. Edinger, Sediment Transport Modeling Review—Current and Future Developments, J. Hydraul. Eng. 134 (2008) 1–14.

[23]   N.R.B. Olsen, M.C. Melaaen, Three-Dimensional Calculation of Scour Around Cylinders, J. Hydraul. Eng. 119 (1993) 1048–1054.

[24]   B. Brørs, Numerical Modeling of Flow and Scour at Pipelines, J. Hydraul. Eng. 125 (1999) 511–523. doi:10.1061/(ASCE)0733-9429(1999)125:5(511).

[25]   S.Y. Wang, Y. Jia, Computational Simulations of Local Scour at Bridge Crossings-Capabilities and Limitations., in: Int. Conf. Hydro-Science Eng. 2000, Korea Water Resour. Assoc., Seoul, Korea, 2000.

[26]   A. Roulund, B.M. Sumer, J. Fredsoe, J. Michelsen, Numerical and experimental investigation of flow and scour around a circular pile, J. Fluid Mech. 534 (2005) 351–401.

[27]   Y. Aghaee, H. Hakimzadeh, Three Dimensional Numerical Modeling of Flow around Bridge Piers Using LES and RANS, in: River Flow, Dittrich, Koll, Aberle and Geisenhainer (Eds) P(2010), 2010.

[28]   A. Khosronejad, S. Kang, F. Sotiropoulos, Experimental and computational investigation of local scour around bridge piers, Adv. Water Resour. 37 (2012) 73–85.

[29]   X. Liu, M.H. García, Three-Dimensional Numerical Model with Free Water Surface and Mesh Deformation for Local Sediment Scour, J. Waterw. Port, Coastal, Ocean Eng. 134 (2008) 203–217.

[30]   A.M.A. Sattar, H. Jasak, V. Skuric, Three dimensional modeling of free surface flow and sediment transport with bed deformation using automatic mesh motion, Environ. Model. Softw. 97 (2017) 303–317.

[31]   J. Chauchat, Z. Cheng, T. Nagel, C. Bonamy, T.-J. Hsu, SedFoam-2.0: a 3-D two-phase flow numerical model for sediment transport, 105194 (2017) 4367–4392.

[32]   X. Yu, T.-J. Hsu, J.T. Jenkins, P.L.-F. Liu, Predictions of vertical sediment flux in oscillatory flows using a two-phase, sheet-flow model, Adv. Water Resour. 48 (2012) 2–17.

[33]   T.G. Drake, J. Calantoni, Discrete particle model for sheet flow sediment transport in the nearshore, J. Geophys. Res. Ocean. 106 (2001) 19859–19868.

[34]   J. Heald, I. McEwan, S. Tait, Sediment transport over a flat bed in a unidirectional flow: simulations and validation, Philos. Trans. R. Soc. A Math. Phys. Eng. Sci. 362

(2004) 1973–1986.

[35]   T. Asano, Two-Phase Flow Model on Oscillatory Sheet-Flow, in: Coast. Eng. 1990, American Society of Civil Engineers, New York, NY, 1991: pp. 2372–2384.

[36]   L. Li, M. Sawamoto, Multi-Phase Model on Sediment Transport in Sheet-Flow Regime Under Oscillatory Flow, Coast. Eng. Japan. 38 (1995) 157–178.

[37]   J.T. Jenkins, D.M. Hanes, Collisional sheet flows of sediment driven by a turbulent fluid, J. Fluid Mech. 370 (1998) S0022112098001840.

[38]   T. Revil-Baudard, J. Chauchat, A two-phase model for sheet flow regime based on dense granular flow rheology, J. Geophys. Res. Ocean. 118 (2013) 619–634.

[39]   F. Chiodi, P. Claudin, B. Andreotti, A two-phase flow model of sediment transport: transition from bedload to suspended load, J. Fluid Mech. 755 (2014) 561–581.

[40]   T.-J. Hsu, Toward modeling turbulent suspension of sand in the nearshore, J. Geophys. Res. 109 (2004) C06018.

[41]   L. Amoudry, T.-J. Hsu, P.L.-F. Liu, Two-phase model for sand transport in sheet flow regime, J. Geophys. Res. 113 (2008) C03011.

[42]   J. Chauchat, S. Guillou, On turbulence closures for two-phase sediment-laden flow models, J. Geophys. Res. 113 (2008) C11017.

[43]   S.K. Jha, F.A. Bombardelli, Toward two-phase flow modeling of nondilute sediment transport in open channels, J. Geophys. Res. 115 (2010) F03015.

[44]   X. Yu, T.-J. Hsu, D.M. Hanes, Sediment transport under wave groups: Relative importance between nonlinear waveshape and nonlinear boundary layer streaming, J. Geophys. Res. 115 (2010) C02013.

[45]   A. Yeganeh-Bakhtiary, M.H. Kazeminezhad, A. Etemad-Shahidi, J.H. Baas, L. Cheng, Euler–Euler two-phase flow simulation of tunnel erosion beneath marine pipelines, Appl. Ocean Res. 33 (2011) 137–146.

[46]   L.O. Amoudry, Extension of k-w turbulence closure to two-phase sediment transport modelling: Application to oscillatory sheet flows, Adv. Water Resour. 72 (2014) 110–121. 6.

[47]   C.-H. Lee, Y.M. Low, Y.-M. Chiew, Multi-dimensional rheology-based two-phase model for sediment transport and applications to sheet flow and pipeline scour, Phys. Fluids. 28 (2016) 053305.

[48]   Z. Cheng, T.-J. Hsu, J. Calantoni, SedFoam: A multi-dimensional Eulerian two-phase model for sediment transport and its application to momentary bed failure, Coast. Eng. 119 (2017) 32–50.

[49]   J. Fredsoe, Article in Hydrology Research, (1976) 293–306.

[50]   T.-J. Hsu, J.T. Jenkins, P.L.-F. Liu, On two-phase sediment transport: sheet flow of massive particles, Proc. R. Soc. A Math. Phys. Eng. Sci. 460 (2004) 2223–2250.

[51]   Y. Kim, Z. Cheng, T.-J. Hsu, J. Chauchat, A numerical study of sheet flow under monochromatic non-breaking waves using a free surface resolving Eulerian two-phase flow model, J. Geophys. Res. Ocean. (2018).

[52] D.A. Drew, Mathematical Modeling of Two-Phase Flow, Annu. Rev. Fluid Mech. 15 (1983) 261–291.

[53] J. Ding, D. Gidaspow, A bubbling fluidization model using kinetic theory of granular flow, AIChE J. 36 (1990) 523–538.

[54] N.F. Carnahan, K.E. Starling, Equation of State for Nonattracting Rigid Spheres, J. Chem. Phys. 51 (1969) 635–636.

[55] D. Gidaspow, Multiphase flow and fluidization: Continuum and kinetic theory descriptions, Acad. Press. (1994).

[56] P.C. Johnson, R. Jackson, Frictional–collisional constitutive relations for granular materials, with application to plane shearing, J. Fluid Mech. 176 (1987) 67.

[57] A. Srivastava, S. Sundaresan, Analysis of a frictional–kinetic model for gas–particle flow, Powder Technol. 129 (2003) 72–85.

[58] D.G. Schaefer, instability in the Evolution Equations Describing Incompressible Granular Flow, 1987.

[59] A. Kumar, U.C. Kothyari, K.G. Ranga Raju, Flow structure and scour around circular compound bridge piers – A review, J. Hydro-Environment Res. 6 (2012) 251–265.

[60] F. Li, L. Cheng, Prediction of Lee-Wake Scouring of Pipelines in Currents, J. Waterw. Port, Coastal, Ocean Eng. 127 (2001) 106–112.

[61] N. Nagata, T. Hosoda, T. Nakato, Y. Muramoto, Three-Dimensional Numerical Model for Flow and Bed Deformation around River Hydraulic Structures, J. Hydraul. Eng. 131 (2005) 1074–1087.

[62] N.R.B. Olsen, H.M. Kjellesvig, Three-dimensional numerical flow modeling for estimation of maximum local scour depth, J. Hydraul. Res. 36 (1998) 579–590.

[63] L. Zhou, Numerical modelling of scour in steady flows, Université de Lyon, 2017.

[64] L.O. Amoudry, P.L.-F. Liu, Two-dimensional, two-phase granular sediment transport model with applications to scouring downstream of an apron, Coast. Eng. 56 (2009) 693–702.

[65] S.S. Chatterjee, S.N. Ghosh, M. Chatterjee, Local Scour due to Submerged Horizontal Jet, J. Hydraul. Eng. 120 (1994) 973–992.

[66] C.-H. Lee, C. Xu, Z. Huang, A three-phase flow simulation of local scour caused by a submerged wall jet with a water-air interface, Adv. Water Resour. (2017).

[67] Z. Cheng, T.-J. Hsu, J. Chauchat, An Eulerian two-phase model for steady sheet flow using large-eddy simulation methodology, Adv. Water Resour. 111 (2018) 205–223.

[68] S.. Han, Characteristics of flow around 90º open channel bends. PhD thesis., Concordia University, Montreal, Quebec., 2010.

[69] P.K. Sweby, High Resolution Schemes Using Flux Limiters for Hyperbolic Conservation Laws, SIAM J. Numer. Anal. 21 (1984) 995–1011.

5   CONCLUSIONS

The main focus of this research project lies in the analysis and prediction of the flow pattern and sediment transport process in open channels by using three-dimensional numerical models. In order to achieve this goal, a review of the mathematical formulation involved is presented to understand, the need to use a turbulence model, the method applied to track or capture the free-surface variations and physical-based mathematical formulation used to study the sediment transport process.

Turbulence models are required to represent the scales which are not resolved. The study of the two main approaches are used in this research; i.e. LES and RANS. The Volume of Fluid (VOF) method is used to capture the free-surface interface, due to several studies have demonstrated its applicability in river engineering problems where complex water surface deformations are presented. Note that in river engineering applications, a detailed prediction of the turbulence features in the free-surface boundary is not the main interest.

The numerical simulation is performed using representative experimental cases which were selected due to the fact that they provide interpretations that can bring knowledge on the complex process involved in river engineering problems which usually include: free-surface flows around hydraulic structures, secondary flows in bend channels and besides the sediment transport effects.

In addition, a mesh sensitive analysis was conducted in all the numerical configurations in order to determine an adequate grid size which provides a balance between accuracy and computational time.

Regarding the analysis and prediction of the flow structure in open-channels, the following conclusions and recommendations are presented.

Unsteady-state (transient) hydraulic flow conditions, Three-dimensional numerical analysis of dam-break flow waves with the presence of an obstacle.

- Three-dimensional numerical configurations; i.e. LES, RANS and LAMINAR show good performance when the results are compared against laboratory experimental data in two hydraulic variables; i.e. water depth and pressure.
- The use of a specific 3D numerical approach affects both qualitative and quantitative comparisons.

- The non-use of a turbulence model (LAMINAR) presents lower R^2 performance. Therefore, the results demonstrate that turbulence approach is important in the analysis.

- There is no clear trend to support that turbulence model approach (LES or RANS) produces better adjustments.

Steady-state hydraulic flow conditions, Three-dimensional comparative numerical analysis in an open-channel bend.

- Three-dimensional numerical model results; i.e. Static Smarinsky, Dynamic Smarinsky and k-ε (RNG), present an acceptable level of agreement in the variables analyzed; i.e. water level and longitudinal velocity component.
- The major discrepancies of the simulated values occur in the middle sections of the channel bend, where the influence of the secondary flow is significant.

Field-scale, Three-dimensional numerical analysis of free-surface flows in a sharp open-channel bend influenced by a weir and a sluice gate

- Three-dimensional outcomes are in good agreement against experimental observations; i.e. water depths.
- In the first sharp bend, a main secondary flow forms along the bed moving toward the inner wall closer to the middle of the channel width and a minor secondary flow with opposite direction is formed near the outer wall and near the water surface.
- In the second sharp bend, which is influenced by a weir and a gate, a major secondary flow forms along the bed moving toward the outer wall closer to the middle of the channel width and a minor secondary flow forms near the inner wall of the channel along the bend.
- The three-dimensional numerical analysis suggests to evaluate geometric modifications of the channel in the sharp bends parts due to a zone of low velocities is produced causing a stagnation zone.

The accuracy of the results of the new multi-dimensional two-phase flow approach for sediment transport is analyzed using the experimental data of turbulent wall jet scour. The examination of the results provides the following conclusions:

- The numerical results adequately match against the experimental depth scour measurements.
- A complete analysis of the sediment profile can be performed.
- The non-consideration of the mesh movement in this numerical approach for the bed profile update provides numerical stability.

- Despite the satisfactory results obtained with this numerical model, a calibration process of the parameter B has to be performed in order to set a value that better matches with this test-case.

In conclusion, three-dimensional numerical configurations provide satisfactory results in the different engineering problems analyzed. The results clearly demonstrate that the use of the turbulence approach is important in the three-dimensional numerical analysis.

The use of 3D numerical models increases the density of spatial information in comparison with experimental cases. Therefore, the results allow to analyze components of velocity, pressure values, streamlines and secondary flows. In regard to sediment transport, the new 3D model approach can resolve the full concentration profile from immobile bed to dilute region of transport away from the bed.

It is worth mentioning that, although the numerical results are satisfactory, the application of three-dimensional numerical models in field-scale requires high computational resources.